DEANSHIP OF GRADUATE STUDIES

AL- QUDS UNIVERSITY

Macroscopic magnetic characterization of Mn_4FeSi_3 single crystal

Shatha Nazzal Naji Nazzal

M.Sc. Thesis

Jerusalem-Palestine

1444 / 2023

Macroscopic magnetic characterization of Mn_4FeSi_3 single crystal

Prepared by:

Shatha Nazzal Naji Nazzal

B.Sc.: Arab American university, Palestine

Supervisors:

Dr. Husain Alsamamra

Physics Department, Al-Quds University, Palestine

apl. Prof. Dr. Karen Friese

Jülich Centre for Neutron Science-2, Forschungszentrum Jülich, Germany

Dr. Jörg Voigt

Jülich Centre for Neutron Science-2, Forschungszentrum Jülich, Germany

Co-supervisor

Dr. Nour Maraytta, Physics Department, Birzeit University, Palestine.

A thesis submitted in partial fulfillment of requirement for the degree of Master of Physics, Faculty of Graduate Studies, Al- Quds University

Jerusalem-Palestine

1444 / 2023

Al-Quds University

Deanship of Graduate Studies

Physics Department

Thesis Approval

Macroscopic magnetic characterization of Mn_4FeSi_3 single crystal

Prepared by: Shatha Nazzal Naji Nazzal

Registration No.: 22012156

Supervisors

Dr. Husain Alsamamra, Physics Department, Al-Quds University, Palestine.
apl.Prof. Dr. Karen Friese, Jülich Centre for Neutron Science-2, FZ Jülich, Germany.
Dr. Jörg Voigt, Jülich Centre for Neutron Science-2, FZ Jülich, Germany.

Co-supervisor

Dr. Nour Maraytta, Physics Department, Birzeit University, Palestine.

Master thesis submitted and accepted, Date: 29/04/2023.

The names and signatures of the examining committee members are as follows:

1- Head of Committee: Dr. Husain Alsamamra Signature

2- Internal Examiner: Prof. Dr. Musa Abu Teir Signature

3- External Examiner: Dr. Muayad Abu Saa Signature

Jerusalem-Palestine

1444 / 2023

Dedication

I dedicate this work to my lovely family, my parents Ashjan and Nazzal, my sister Wafa, my brothers Firas and Fares who have been a constant source of support and encouragement.

My grandmother who has never stop pursuit of knowledge and motivating me to get higher education.

To all my respected teachers, friends and colleagues.

Declaration

I certify that this thesis submitted for the degree of the master is the result of my research, except where otherwise acknowledged, and that this thesis, neither in whole nor in part, has been previously submitted for any degree to any other university or institution.

The work was done under the supervision of Dr. Husain Alsamamra, from the Physics Department, Al-Quds University, Palestine, and apl.Prof. Dr. Karen Friese, Jülich Centre for Neutron Science-2, FZ Jülich, Germany, and Dr. Jörg Voigt, Jülich Centre for Neutron Science-2, FZ Jülich, Germany[1], and Dr. Nour Maraytta, from the Physics Department, Birzeit University, Palestine.

Signed: 

Name: Shatha Nazzal Naji Nazzal

Date: 29/ 04 / 2023

[1] This project is part of a collaborative effort under the framework collaboration between FZ-Jülich Research Center, Germany, and Al-Quds University, Palestine, and coordinated by Karen Friese, Jülich Centre for Neutron Science CNS-2 and Husain Alsamamra from the Department of Physics.

Acknowledgements

I would like to express my sincere gratitude to all who support me during the running of this project.

Palestinian-German Science Bridge PGSB, the scholarship program, for giving me this significant opportunity. **Prof. Dr. Thomas Brückel**, the director of JCNS-2 and PGI-4, and **apl. Prof. Dr. Karen** for giving me the opportunity to work at JCNS-2.

Further, I would like to express my deepest appreciation to my supervisor **Dr. Husain Alsamamra**, who nominated me to conduct my thesis within this project. I could not have undertaken this journey without his consistent support and wise guidance throughout this project.

My deepest gratitude goes to my supervisor **apl. Prof. Dr. Karen Friese** who gave me the opportunity to work with her team, for the thoughtful guidance, constructive discussions, and amending my writing during the running of this project.

My sincere appreciation to my supervisor **Dr. Jörg Voigt** for his consistent support in the magnetization measurements, data analysis, and writing progress. I am grateful for his insightful suggestions, discussions and provoking me always to learn.

Dr. Nour Maraytta for her help in the experimental work, guidance and assisting in reviewing my thesis. Special thanks for **DP. Jörg Persson** for his patience, faithful support in preparing the samples and discussing the techniques.

All our group scientists **Prof. Dr. Manuel Angst** and **Dr. Andrzej Grzechnik** for the fruitful discussions and suggestions.

The instruments scientists **Dr. Oleg Petracic** and **Dr. Shibabrata Nandi** for their help in scheduling the measurements. **Berthold Schmitz** due to his kind technical assistance during the magnetization measurements.

Special thanks for my college, **Dr. Pulkit Prakash** who shared me the office and provided me his kind support and useful discussions. My colleagues **Hend Shahed**, **Dr. Neetika** and **Viliam** for their support and hospitality. **Sameh Othman** for his support in learning python basics.

The IT-team **Micha Hölzle** and **Markus Consoir** for the technical support. **Barbara Daegener** for her kind support in the administrative matters, **Caitlin Morgan,** and all in the administrative and security teams who facilitate my journey in **FZJ**.

I would like to extend my heartful thanks to all colleges in **JCNS-2** for their hospitality.

Place of experimental work

The experimental work is implemented at the Jülich Centre for Neutron Science (JCNS-2) institute, in Forschungszentrum Jülich GmbH, Germany.

Juelich Centre for Neutron Science (JCNS) is an international center providing facilities and collaborations for internal and external users by means of a procedure whereby proposals are reviewed by an independent group of experts. JCNS provides many specialized neutron spectrometers at the world's top neutron sources. Additionally, JCNS focuses on research programs in the field of Key Technologies.

JCNS-2 is one of its branches which works to develop and use scattering methods for determination of structural and magnetic order and excitations in novel quantum, nano and functional materials in order to achieve an understanding of macroscopic properties and functionalities.

Jülich Centre for Neutron Science (JCNS).

Abstract

In this work, the macroscopic magnetization study on a single crystal of Mn_4FeSi_3 reveals a variety of the magnetic properties. Magnetization measurements were implemented on a pre-oriented single crystal using Vibrating sample magnetometry (VSM) option. Two different protocols (isofield and isothermal) were followed and showed comparable magnetic response, implying that the system is always in thermodynamic equilibrium. The field dependent magnetization was measured by applying a magnetic field (up to 8 T) along the three symmetry directions of the hexagonal system ([001], [100], [120]). The experimentally calculated paramagnetic moment is determined as ~ 4.3(1) μ_B. The sample exhibits an obvious anisotropic magnetic behavior in the low temperature ranges. In agreement with earlier studies, the compound undergoes a paramagnetic to antiferromagnetic transition around 95 K. This transition is detected along all measured field strengths and field directions. A transition between two distinct antiferromagnetic phases, which was reported in the literature based on measurements on polycrystalline samples, is visible around 65 K only if the field is applied in [001] direction. The present results hint to a temperature independent field-induced transition in the low temperature region < 80 K for a field between 5 and 6 T. This transition manifests itself differently when the field is applied in different directions. The results hint towards the predominance of antiferromagnetic interactions and indicate a preference of moments to align perpendicular to the [001] direction. In addition, ferromagnetic correlations of the *c*-component of the magnetic moments are observed which can be suppressed with increasing the applied field. The latter results, in addition to the drop in the magnetization which occurs in vicinity of 80 K requires a microscopic method to probe the magnetic structure in Mn_4FeSi_3.

Table of contents

List of Figures

List of tables

List of Abreviations

Abbreviation	Representation
MCE	Magnetocaloric effect
PM	Paramagnetic
FM	Ferromagnetic
AF	Antiferromagnetic
T_C	Curie Temperature
T_N	Néel temperature
T	Absolute temperature
H	Magnetic field strength
B	Magnetic flux density
M	Magnetization
μ_0	Magnetic permeability of free space
μ_B	Bohr magneton
Oe	Oersted
T	Tesla
Mn	Manganese
Fe	Iron
Si	Silicon
λ	Wavelength
CCIM	Cold crucible induction melting
PPMS	Physical properties measurement system
VSM	Vibrating sample magnetometer
χ_{mol}	Molar magnetic susceptibility
C	Curie-Weiss constant
μ_{eff}	Effective moment
θ_{cw}	Curie- Weiss temperature

Chapter 1 Introduction

1.1 Motivation

The magnetocaloric effect (Kittel & McEuen, 2018) is an intrinsic property of magnetic substances, which can be defined as a reversible change of temperature is related to the entropy change in a material when exposed to an external magnetic field (De Oliveira & von RANKE, 2010). This entropy change ΔS is related to the coupling between the external field H and the magnetic moments of the solid (Franco et al., 2018).

MCE materials can be used in the magnetic refrigeration cycle, which is shown in **Figure 1.1.** When a paramagnetic material is magnetized adiabatically, the system is heated up (Gschneidner Jr & Pecharsky, 1999). Then the system is demagnetized, and the zero-field magnetic entropy of the system is restored resulting in cooling effect (Reif, 2009). On the other hand, if a substance is exposed to a magnetic field and changes from a magnetically ordered state to a phase with a lower degree of order, the magnetic entropy is increased (Franco et al., 2018; Gencer, Kolat, Izgi, Bayri, & Atalay, 2020). As a consequence, the material will cool down when exposed to an external field, this is known as an inverse or (negative) MCE (O Tegus, Brück, Zhang, Buschow, & De Boer, 2002).

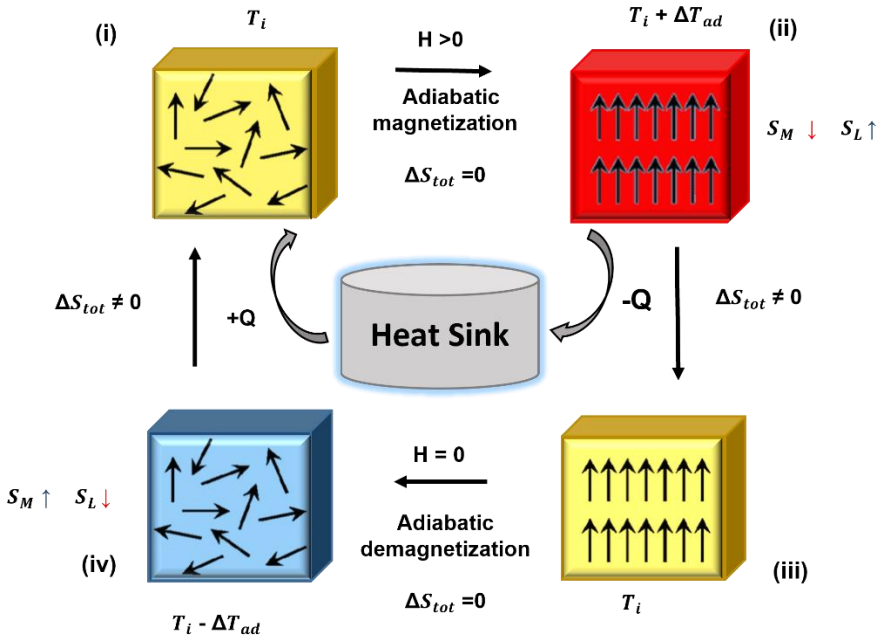

Figure 1.1: The magnetic refrigeration cycle. T_i: initial temperature of the system, ΔT_{ad}: temperature change under adiabatic condition, H: applied field, Q: heat, S_l: lattice entropy, S_M: magnetic entropy, ΔS_{tot}: total entropy change.

Most of the studies on the MCE materials focus on the discovery of new materials with optimized performance, as the caloric cooling cycle is seen as an alternative to the conventional gas compression (CGC) refrigerators. Orendáč and his partners (Orendáč et al., 2018) summarized the advantages of magnetic refrigerators are of being compact, highly efficient, and ecologically friendly.

Thousands of compounds are studied in the context of the magnetocaloric effect MCE, but less than ten systems were labelled as promising materials (Zarkevich & Zverev, 2020). Although the MCE of compounds in the system $Mn_{5-x}Fe_xSi_3$ is moderate (N. Maraytta et al., 2019) when compared to other systems (e.g., rare earth elements), still the system is under intensive exploration owing to its unusual diverse phase diagram, in addition to the availability of constituting elements and environmental acceptability. Approaches to optimize their caloric properties by modification, substituting, or doping are also followed.

Mn-based silicides are remarkable due to their unique crystal and magnetic structures (B. Das et al., 2016). The coupling between spin and lattice degrees of freedom leads to interesting thermodynamic phenomena and physical properties throughout the system (V. Singh, Bag, Rawat, & Nath, 2020; O. Tegus, Brück, Buschow, & de Boer, 2002). This variety of properties is based on the geometry, atomic distances, and the two-symmetry independent atomic sites for the paramagnetic atoms which are preferentially occupied by Mn and Fe (N. Maraytta et al., 2019; Songlin et al., 2002). Consequently, the systematic study of the system provides information on the complex physics behind the MCE, and the magnetic interactions in these intermetallic compounds (Bińczycka, Dimitrijević, Gajić, & Szytula, 1973; Herlitschke et al., 2016).

Doping on the Mn-site influences the Mn-Mn separation as well as the magnetic interactions (S. C. Das, Mondal, Khamaru, Pramanick, & Chatterjee, 2020). Substitution of Mn with the smaller Fe is accompanied leads to a reduction of the unit cell volume, in addition to an increase of the critical temperature at which the transition between the magnetically ordered phase transforms to a paramagnetic phase (Lundgren, Tarmohamed, Beckman, Carlsson, & Rundqvist, 2007; V. Singh et al., 2020). Thus, while for low concentrations of Fe the ordering temperatures are much lower than 300 K, for high concentrations (x=4) the system undergoes the transition to a ferromagnetically ordered phase close to room temperature (Gourdon et al., 2014). This opens the way to several practical applications, in particular room temperature cooling and heating

(Gottschilch et al., 2012). Moreover, in difference to many other magnetocaloric materials it is possible to synthesize large single crystals which preserve their stability while crossing the magnetic transition temperatures (Biniskos et al., 2017; Herlitschke et al., 2016; N Maraytta et al., 2020). Due to this, a wide range of different measurements techniques are available for the characterization of the structures, dynamics and properties of the compounds.

$Mn_4 Fe Si_3$ has the reverse iron-manganese ratio with respect to $Mn_4 FeSi_3$ (x=4), which is reported as the most promising compound in this system with a magnetic transition near to the room temperature (Hering et al., 2015; Songlin et al., 2002). Moreover, it is expected to share the properties with the neighboring compounds with the low Fe concentration (x= 0 and 2).

This study aims to explore the macroscopic magnetic characteristics of $Mn_4 Fe Si_3$ (x=1) and forms part of an investigation aimed at understanding the MCE throughout the system. The main purposes of this work are:

- To explore the direction dependent macroscopic magnetic properties of the studied compound using magnetization measurements.
- To detect the nature of magnetic ordering and the phase transition temperatures of the sample.
- To compare the main features obtained from direction-dependent study on a single crystal with the previous works on polycrystalline material of the same substance.
- To compare the magnetic properties of $Mn_4 Fe Si_3$ (x=1) to the properties of the neighboring compounds of the system with x= 0 and 2.

1.2 Thesis Structure

This thesis consists of six chapters, structured in the following way:

- **Chapter 1** includes the motivation of this work, the main objectives, and explains the structure of the thesis.

- **Chapter 2** introduces the literature on $Mn_{5-x}Fe_xSi_3$ system, the crystal structure, and the magnetic structure. The basics of magnetism and essential models related to the content of this work are explained.

- **Chapter 3** outlines the techniques used in the experimental part of this research. It includes a description of the used instruments and the measurements protocol.

- **Chapter 4** presents the data analysis divided into two sections. The first one is related to the Laue diffraction results, the second one displays the outcomes of the magnetization measurements.

- **Chapter 5** provides a discussion of the main results and concludes the highlights of this research, including a comparison between the properties and features of the neighboring compounds (x= 0, 1 and 2) in $Mn_{5-x}Fe_xSi_3$ system.

- **Chapter 6** an outlook and recommendations for future investigations are included.

Chapter 2 Investigated material system and theoretical background

2.1 $Mn_{5-x}Fe_xSi_3$ system

2.1.1 Crystal structure

The parent structure of $Mn_{5-x}Fe_xSi_3$ crystallizes in a hexagonal crystal structure (space group $P6_3/mcm$) and can be considered as a distorted variant of the NiAs structure type (Johnson, Weiher, Frederick, & Rogers, 1972). According to (Hering et al., 2015) the symmetry of the crystal structure of $MnFe_4Si_3$ is reduced to $P\bar{6}$. Within the structure two symmetrically independent Wyckoff positions are occupied by the transition metals (4*d* and 6*g*), named as *M1* and *M2*, respectively (Al-Kanani & Booth, 1997). This results in conflicting intra- and inter-sublattice interactions which are affected by Mn-Mn distances (Songlin et al., 2002).

As shown in **Figure 2.1**, The *M1* site is surrounded by six Si atoms at distances ≈ 2.4 Å, leading to the formation of distorted [$M1\ Si_6$]-octahedra. These octahedra share triangular faces, resulting in an infinite chain of composition [$M1\ Si_3$] along the *c*-axis. The six *M2* atoms form a distorted empty octahedron [$M2_6$]. These octahedral also share triangular faces and build an infinite chain of [$M2_3$] along the *c*-axis (Eich et al., 2019; Hering et al., 2015; Johnson et al., 1972).

The occupation of the atomic sites depends on the Fe content (Luccas et al., 2019). Whereas Fe prefers to occupy the *M1* site, Mn tends to prefer the *M2* site, as illustrated in **Figure 2.2**. According to (Johnson et al., 1972) this preference is related to the fact that the smaller and more electronegative Fe atoms have more stable metal-metal bonds in the 4*d* site than the Mn atoms. However, it has been shown that the ordering of Mn and Fe into the different Wyckoff positions is never perfectly complete (Ait Haddouch et al., 2022; Hering et al., 2015). Neutron diffraction studies revealed that the metal sites split into multiple atomic sites with different arrangement of the moments below the ordering temperature (Hering et al., 2015; Herlitschke et al., 2016).

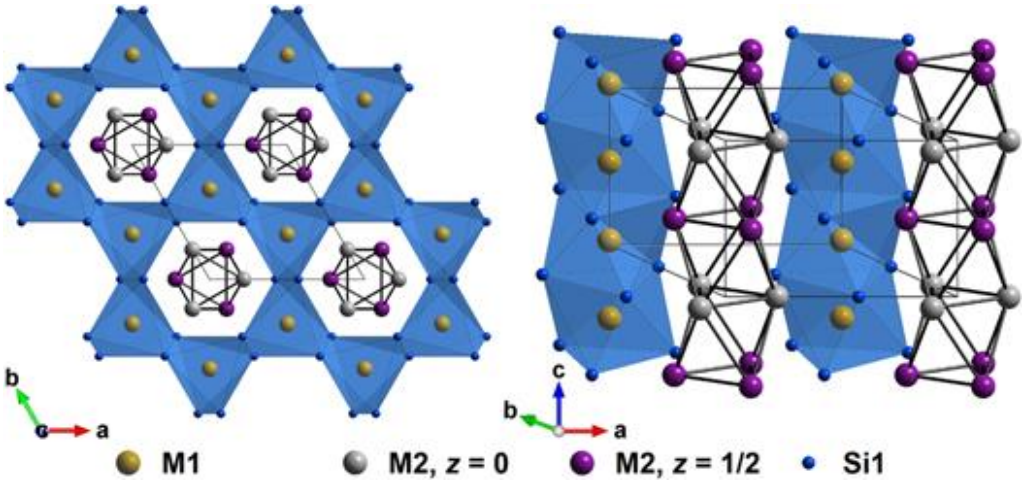

Figure 2.1: Crystal structure of $Mn_{5-x}Fe_xSi_3$ (Eich et al., 2019) (Left) A projection along the [001] direction and (right) a projection approximately along the [120] direction.

In the parent compound Mn_5Si_3, Mn atoms occupy both *M1* and *M2* positions. In Mn_4FeSi_3, Because the Fe is preferentially incorporated into the *M1* position, Mn and Fe share this site approximately equally, while the *M2* position is mostly occupied with Mn atoms (M1: 42.3% Fe, 57.7% Mn; M2: 5.1% Fe, 94.9% Mn) (Bińczycka et al., 1973). With increasing Fe content (*x*=2), the *M1* sites become nearly fully occupied by Fe and most of *M2* sites are occupied by Mn (M1: 76.5(1) %Fe, 23.4 %Mn; M2: 15.6 %Fe, 84.4 %Mn) (Ait Haddouch et al., 2022).

Mn_5Si_3 affords a structural transition at 100 K in which the symmetry is reduced from hexagonal (*P*6$_3$*/mmc)* to orthorhombic (*Ccmm)* (Candini et al., 2004; Lander, Brown, & Forsyth, 1967). In contrast to (Candini et al., 2004) who reported the distortion for *x*=1 close to 70 K coinciding with the low temperature magnetic transition, a recent study (Karen Friese, 2023) revealed that the orthorhombic structure is already observed at higher temperatures up to (95 – 100) K.

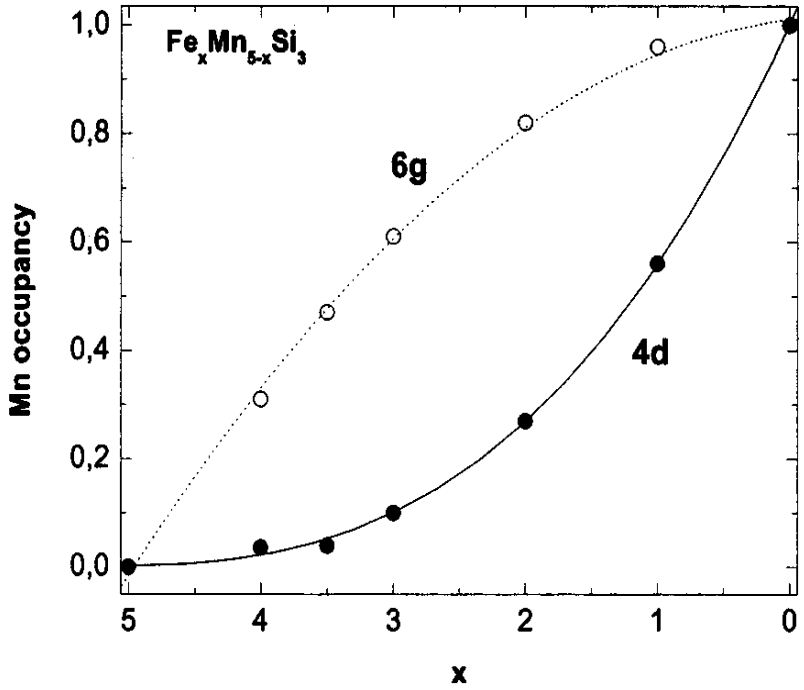

Figure 2.2: The manganese occupancy of Wyckoff positions (*4d* and *6g*) versus iron concentration in the $Mn_{5-x}Fe_xSi_3$ system (Candini et al., 2004).

The relationship between the hexagonal and the orthorhombic structure is illustrated in **Figure 2.3**. Assuming the orthorhombic standard setting *Cmcm*, the transformation which relates the lattice parameters of both phases is given as (Hahn, Shmueli, & Arthur, 1983): $a_{\text{ortho}} \approx 2a_h + b_h = \sqrt{3}\, a_h$, $b_{\text{ortho}} \approx b_h$, $c_{\text{ortho}} \approx c_h$. However, in the literature the orthorhombic structure is often described in the setting *Ccmm*.

At ambient conditions, $Mn_4\,Fe\,Si_3$ crystallizes in the hexagonal structure (space group $P6_3/mcm$) with lattice parameters $a = b = 6.885$ A°, $c = 4.786$ A° ($\alpha = \beta = 90°$, $\gamma = 120°$) and unit cell volume V≈ 196.4 Å (Bińczycka et al., 1973).

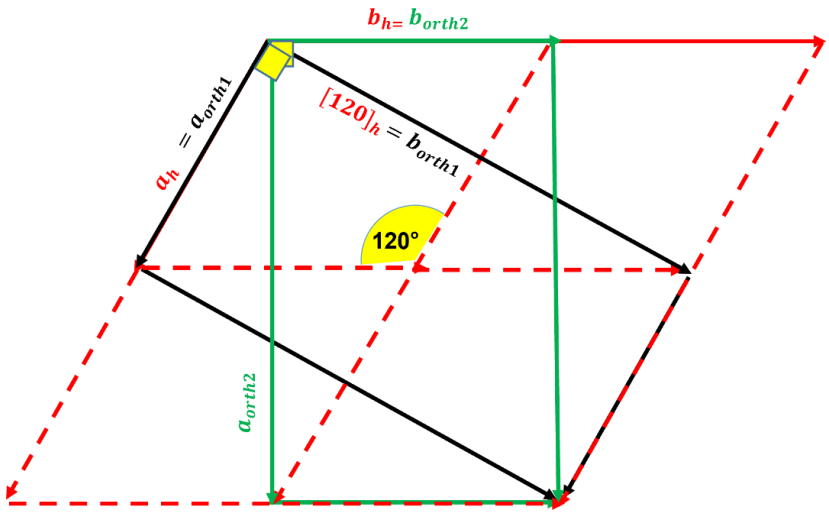

Figure 2.3: Illustration of the relation of the lattices of the hexagonal high temperature phase and orthorhombic low temperature phase. The hexagonal lattice (red), the orthorhombic lattice: *Ccmm* (black) and *Cmcm* (green).

2.1.2 Magnetic structure

The magnetic properties and interactions depend on the composition **(Figure 2.4).** For the Mn rich compositions ($x \leq 3$) antiferromagnetic AF interactions are observed at low temperatures while for higher Fe contents ($x > 3$) ferromagnetic FM interactions dominate (Narasimhan, Reiff, Steinfink, & Collins, 1970; V. Singh et al., 2020; Songlin et al., 2002; Vinokurova, Ivanov, & Kulatov, 1995). A direct MCE was recorded for compounds with $x \geq 3$, while an inverse MCE was reported for the two compounds with $x= 0$ and $x= 2$ (Ait Haddouch et al., 2022; Gottschilch et al., 2012; Luccas et al., 2019).

Within the system, Mn Fe_4Si_3 ($x= 4$) has the largest MCE with ΔS_M (T) ≈ 2 J/kg. K for a field change of 2 T (Hering et al., 2015). This compound exhibits a transition from paramagnetic PM to FM state at room temperature and shows a significant anisotropy, both in the magnetization and the MCE (N. Maraytta et al., 2019).

According to the literature, each of these three compounds ($x= 0,1,2$) has two magnetic phase transitions. On lowering the temperature, the transition from the paramagnetic to an antiferromagnetically ordered phase (AF2) is observed. This is followed by a second transition at lower temperatures to a second antiferromagnetically ordered phase (AF1) (V. Singh et al., 2020; Songlin et al., 2002).

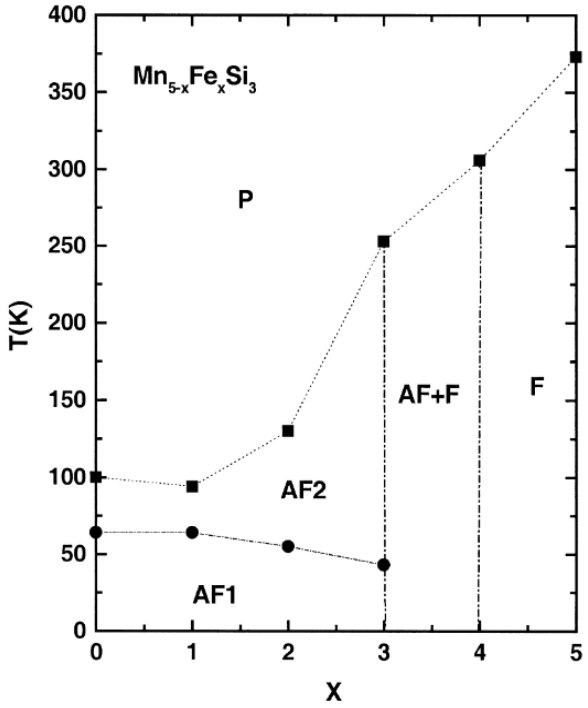

Figure 2.4: Sketch of the magnetic phase diagram for $Mn_{5-x}Fe_xSi_3$ system (Songlin et al., 2002).

A brief synopsis of the magnetic structure for the compounds with (x= 0-2) is given in **Table** 2.1**.** The high temperature phases AF2 of x= 0 and 2 are co-linear, while the AF1 phases are not. Noting that there are discrepancies in the literature concerning the AF1 phase of Mn_5Si_3. The high temperature magnetic structure of x=1 was supposed to exhibit incommensurate antiferromagnetic ordering (Candini et al., 2004). Currently ongoing investigations on the magnetic structure of this compound, confirm the incommensurate propagation vector. Preliminary refinements of the magnetic structure in superspace indicate that in both the low temperature phase and the high temperature phase, the *M1* and *M2* sites show a co-planar ordering of the magnetic moments in *a,b*-plane (Karen Friese, 2023).

x	0	1	2
High temperature phase	collinear	Incommensurate, Co-planar	collinear
Direction of ordered moment			
M1	-	In (*a*, *b*- plane)	along *b*
M2	$2/3$ (along *b*)	In (*a*, *b*- plane)	$2/3$ (along *b*)
Low temperature phase	non-collinear	Incommensurate Co-planar	Co-planar
Direction of ordered moment			
M1	along *c*	In (*a*, *b*- plane) and ⊥ (*a*, *b*- plane)	along *b*
M2	$2/3$ in (*a*, *b*-plane) with a small amount along *c*	In (*a*, *b*- plane) and ⊥ (*a*, *b*- plane)	$2/3$ in (*b*, *c*-plane)

Table 2.1: Summary of the information on the magnetic structures for $Mn_{5-x}Fe_xSi_3$ (*x*= 0, 1 and 2). Data is taken from (Ait Haddouch et al., 2022; Candini et al., 2004; Gottschilch et al., 2012; Karen Friese, 2023). Note that: (1) the high temperature and low temperature phases are named as AF2 and AF1 in the literature. (2) There are discrepancies in the literature concerning the AF1-phase of *x*= 0.

2.2 Magnetism basics

2.2.1 Exchange interaction and Curie- Weiss law

This section closely follows the explanation from (Buschow & Boer, 2003). Long range magnetic order results from the exchange interactions between the spins of the atoms in a crystal lattice. In the general form, the Heisenberg exchange Hamiltonian describes the symmetric exchange interaction as a sum over all spin pairs in the lattice:

$$\boldsymbol{H_{exch}} = -\sum_{i<j} 2J_{ij}\boldsymbol{S_i}.\boldsymbol{S_j} \tag{2.1}$$

where J_{ij} is the exchange constant which depends on the distance between the atoms i, j. The direct exchange interaction is strong in *3d* metals. If $J_{ij} > 0$, the spins tend to align parallel to each other resulting in ferromagnetic order (FM), while for $J_{ij} < 0$, the spins prefer to arrange antiparallel with respect to each other leading to antiferromagnetic order (AF). In the mean (molecular) field approximation the sum over all spin pairs is approximated by an effective field acting on a single spin. Thus, S_j is replaced by the average $< S_j >_{Av}$ which is proportional to the average magnetization $\boldsymbol{M}$, and $\boldsymbol{H_{exch}}$ is proportional to the molecular field $\boldsymbol{H_m}$ .With applying an external magnetic field $\boldsymbol{H}$, the total field experienced by the i^{th} moment can be written for ferromagnetic interactions:

$$\boldsymbol{H_{tot}} = \boldsymbol{H} + \boldsymbol{H_m} = \boldsymbol{H} + N_w \boldsymbol{M} \tag{2.2}$$

here N_w is called the molecular- (or Weiss) field constant. A ferrimagnet and a simple antiferromagnet in a crystalline material can be regarded as two sublattices (A and B) where the moments are aligned ferromagnetically in each sublattice and in opposite directions with respect to each other (Kittel & McEuen, 2018). In the former case, where the magnitude of moments $M_A \neq M_B$ and/or the number of A and B sites per unit cell are different, there is a net spontaneous magnetization. Two different magnetic species (e.g., different elements, different valence states, e.g., Fe^{2+} and Fe^{3+}) are required for ferrimagnetic interactions (Hurd, 1982). While for the latter case, the moments are equal $M_A = M_B$.

However, the molecular (mean) field caused by moments in the same sublattice is different from that caused by the antiparallel sublattice. Then, the total field on each sublattice in an antiferromagnet can be written as:

$$\boldsymbol{H_A} = \boldsymbol{H} + N_1\boldsymbol{M_A} + N_2\boldsymbol{M_B}\,;\ \boldsymbol{H_B} = \boldsymbol{H} + N_1\boldsymbol{M_B} + N_2\boldsymbol{M_A} \tag{2.3}$$

where N_1 is the intrasublattice-molecular field- constant, the contribution of the molecular field caused by the same sublattice and N_2 ($N_2 = N_{AB} = N_{BA}$) is the intersublattice-molecular field-constant or the exchange parameter, the contribution of the molecular field caused by the other sublattice. At a relatively high temperature (paramagnet PM state) where the thermal fluctuations are stronger than the interactions between the spins, a random distribution of the moments is produced by the thermal energy (K_BT). These randomly oriented moments can be aligned by applying an external magnetic field $\boldsymbol{H}$ (Blundell, 2001). The critical temperature at which the ordering occurs (T_{ord}) is called Neel Temperature T_N for AF phase (Hurd, 1982).

According to (Buschow & Boer, 2003) from the high- temperature treatment the sublattice moments could be derived as $\boldsymbol{M_A} = \frac{C'}{H}(\boldsymbol{H} + N_1\boldsymbol{M_A} + N_2\boldsymbol{M_B})$ and $\boldsymbol{M_B} = \frac{C'}{H}(\boldsymbol{H} + N_1\boldsymbol{M_B} + N_2\boldsymbol{M_A})$. And $C' = C_A = C_B = \frac{1}{2}C$, where C is the Curie-Weiss constant and can be calculated as:

$$C = \frac{\mu_0 N_A J(J+1){\mu_B}^2}{3k_B} \tag{2.4}$$

here k_B is Boltzmann's constant, N_A is Avogadro's number, μ_B is Bohr magneton, μ_0 is permeability of free space and J is the total the angular momentum quantum number.

Hence Neel temperature is obtained as $T_N = \frac{1}{2}C\,(N_1 - N_2)$, but $N_1 > 0$, $N_2 < 0$. For temperatures above T_N, Curie- Weiss law can be followed to calculate the magnetic susceptibility as:

$$\mathcal{X} = \lim_{H \to O} \frac{M}{H} = \frac{M_A + M_B}{H} = \frac{C}{T - \frac{1}{2}C(N_1 + N_2)} = \frac{C}{T - \theta_{cw}} \tag{2.5}$$

thus, $\theta_{cw} = \frac{1}{2}C(N_1 + N_2)$ is the Curie- Weiss temperature.

In mean field approximation, the Curie-Weiss constant *C* is directly proportional to the number of unpaired electrons of the atoms. It can be used to experimentally calculate the effective magnetic moment μ_{eff}^{exp} per unit formula (in units of μ_B) in the PM state as (Day, 1987):

$$\mu_{eff}^{exp} = g\sqrt{J(J+1)} = \sqrt{\frac{3k_B C}{\mu_0 N_A {\mu_B}^2}} \qquad (2.6)$$
$$= 2.828\sqrt{c}\ \text{(CGS)} \approx 798\sqrt{C}\quad \text{(SI)}$$

For *d*-transition metals, if one only accounts for the spin angular momentum *S* as the orbital angular momentum *L* is often quenched (*L= 0, J =S*), the paramagnetic moment can be calculated as ${\mu_{eff}}^2 = g^2\, S(S+1)\, {\mu_B}^2$, where g is their gyromagnetic factor (Mugiraneza & Hallas, 2022). As mentioned above $Mn_{5-x}Fe_xSi_3$ contains $Mn^{2+/3+}$ and $Fe^{2+/3+}$ ions, it can be treated as separate magnetic systems. Thus, assuming that for *x*= 1 (Wyckoff position *4d* of space group *P63/mcm* is half occupied by Mn^{3+} and half by Fe^{3+} while the *6g* site is totally occupied by Mn^{2+} (Johnson, 1972) the theoretical effective moment μ_{eff}^{theo} can be determined using the following formula:

$$\mu_{eff}^{theo} = \sqrt{0.2\ (\mu\, Fe^{3+})^2 + 0.2\ (\mu\, Mn^{3+})^2 + 0.6\ (\mu\, Mn^{2+})^2} \qquad (2.7)$$

The Curie Weiss temperature θ_{cw} and the Curie constant *C* can be obtained by plotting the reciprocal susceptibility χ^{-1} versus the temperature (Figure 2.5). For materials displaying normal paramagnetic behavior, the relation is a straight line above T_{ord}. By fitting the linear part of the $\chi^{-1}(T)$, *C* is determined as the slope of the linear fit and θ_{cw} is the intercept of x-axis. While μ_{eff} per magnetic ion, for this system, can be calculated using equation (2.6).

θ_{cw} is a parameter that indicates the strength of the molecular field. If the molecular field is related to ferromagnetic interactions, then $\theta_{cw} > 0 \approx T_c$, however it is larger than T_c due to the molecular field approximation. If antiferromagnetic or ferrimagnetic interactions prevail, then $\theta_{cw} < 0$ and deviates from T_N (Mugiraneza & Hallas, 2022).

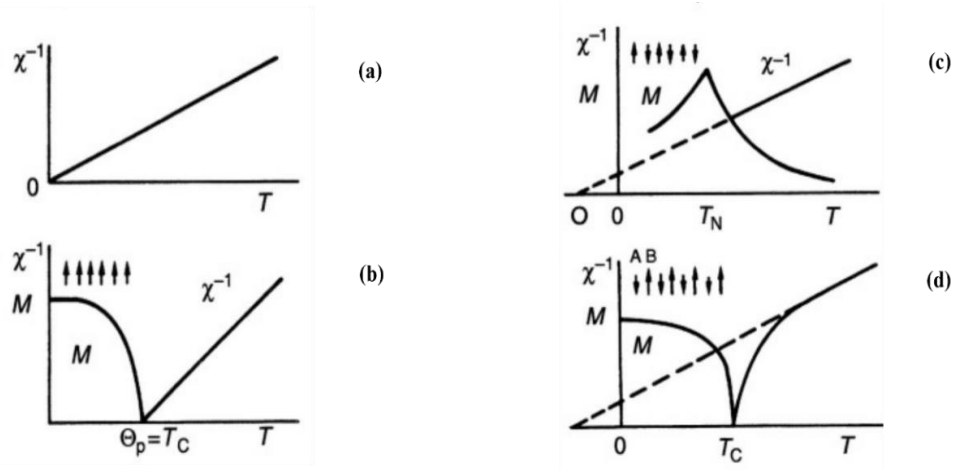

Figure 2.5: The temperature-dependence of the reciprocal susceptibility for (a) a paramagnet (b) a ferromagnet (c) an antiferromagnet (d) a ferrimagnet (Buschow & Boer, 2003).

2.2.2 Anisotropic behavior for a simple antiferromagnet

This section closely follows the explanation from (Buschow & Boer, 2003) and (Coey, 2010). If the magnetic properties of a crystalline material are different depending on the direction, then the material displays magnetic anisotropy. For a simple AF, the external field can be parallel and antiparallel or perpendicular to the two sublattices. In the former case the energy of the parallel sublattice is lowered, while it is increased for the antiparallel sublattice. As the exchange interaction is much stronger than the external field, individual spins cannot be flipped, and the magnetization remains zero. As the temperature gives rise to fluctuations, the fluctuating moments can be aligned with the field leading to a finite magnetization and hence the susceptibility increases. For the field perpendicular, the moments from both sublattices can tilt towards the external field, but still prevail the AF coupling for the largest component of the magnetic moment. So that the magnetization can follow the field independently of the temperature fluctuations and hence the susceptibility remains constant with temperature. The $\chi_\perp = 1/|N_2|$, **Figure 2.6**.

Below T_N ($\chi_\perp > \chi_\parallel$) which means that the application of a field on an antiferromagnetic single crystal always leads to a status where the two sublattices tend to align perpendicular to the direction of the external field. As the field strength is increasing, they bend more toward the field

until they align parallel to ***H***, where the saturation is achieved, i.e., more increasing of the field does not increase the net moment.

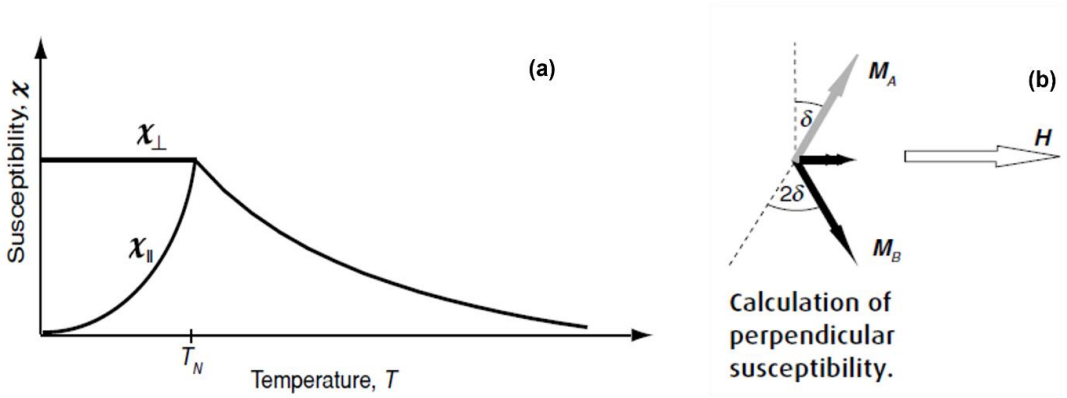

Figure 2.6: (a) The temperature dependence of the magnetic susceptibility in an AF single crystal (with H || and ⊥ to sublattices moments). (b) The alignment of magnetic moments on the two sublattices with H⊥ to sublattices moments (Coey, 2010).

Chapter 3 Experimental procedures (instruments and techniques)

3.1 Sample Synthesis

For single crystal growth with high quality as pure as possible, the sample was prepared in two steps using two techniques. In each step, the preparation environment was aimed to be inert and contaminant-free (S. J. Singh & Sturza, 2022). In the first step, a polycrystalline sample of the intermetallic complex $Mn_2Fe_3Si_3$ (x=3) was produced by the Cold Crucible Induction Melting (CCIM). In the second step, a single crystal was grown from the previously prepared polycrystalline material using the Czochralski method. Both steps were done in suitable experimental setups designed at Forschungszentrum Jülich. The following describes the procedure used for preparing $Mn_2Fe_3Si_3$ (x=3). The sample Mn_4FeSi_3(x=1), which was investigated in this thesis was prepared previously using the same methods.

3.1.1 Polycrystalline synthesis (Cold crucible induction melting device)

This technique of inductive melting in the cold wall crucible is used to produce high purity melts. Unlike traditional melting techniques, Cold crucible induction melting (CCIM) can approach extremely high operational temperatures while keeping the crucible cold. The advantage of this technique is that there is no interaction between the material and the cooper crucible which prevents any contamination (Mühlbauer, 2006).

In this set up, the sample is heated under vacuum conditions to remove the impurities on its surface. Instead of ceramic, a segmented copper crucible, cooled by a water cycle is used to avoid any rection between the material and the crucible. The required energy for heating and melting is generated by an electromagnetic field induced by a solenoidal copper coil surrounding the crucible **(Figure 3.1).** In a principle based on Ampere's law, the flow of high frequency alternating current in the coils creates a high-power alternating magnetic field. This field penetrates through the slits of the crucible and induces 'eddy' currents inside the sample. Once the material is melted, the induced electromagnetic Lorentz forces push the material away from the wall, creating a so- called melt cap. This process results in convenient stirring of the molten material which further enhances the homogeneity of the melt (Mühlbauer, 2006; Pericleous, Bojarevics, Djambazov, Harding, & Wickins, 2006).

The contact between the metal melt and the crucible allows heat to be released from the melt and produce a thin layer of solidified material. This solid layer, called 'skull', separates the metal and the crucible, and prevents direct physical contact between them, avoiding the diffusion of impurities (H. Windsheimer, R. Waitz, & P. Wubben, 2015).

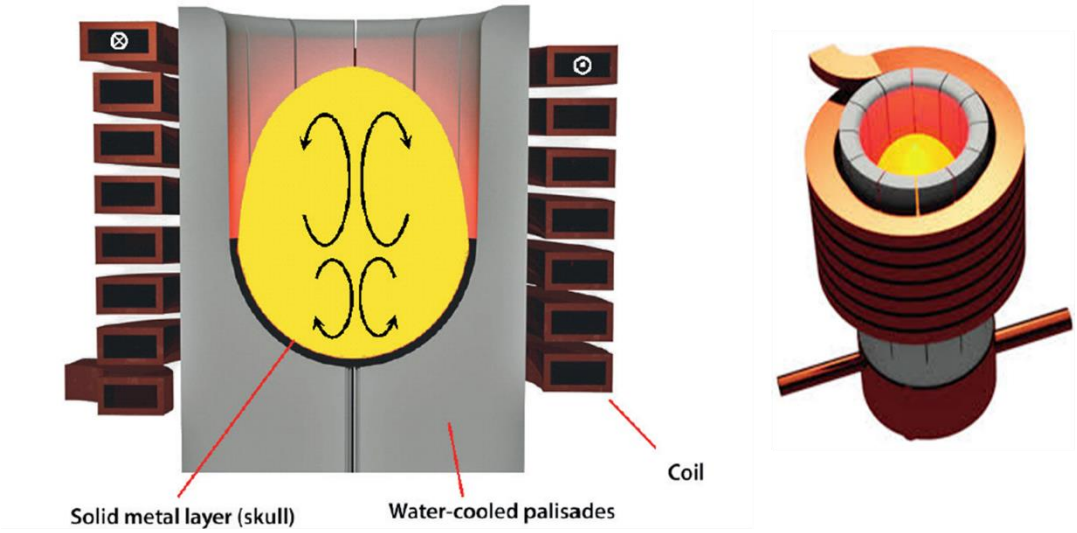

Figure 3.1: (Right) Cold Crucible Induction Melting (CCIM) setup. (Left) a sectional view, taken from (H. Windsheimer, R. Waitz, & P. J. I. t. Wubben, Reports, 2015).

$Mn_2Fe_3Si_3$ polycrystalline ingot synthesis

A pellet of 70 g of $Mn_2Fe_3Si_3$ polycrystalline was produced using the CCIM process. For this, first the calculations based on the weight percent for each element were done. The highly pure elements (4N≈ 99.99 purity) of manganese, iron and silicon were then weighed to be used for the ingot growth. The real mass of each element was recorded as 21.572 g Mn, 32.821 g Fe and 16.501 g Si.

The resulting mixture of these three elements was divided into two halves (35 g for each half) to ensure good heating and homogeneous melting. Then, the two portions of the mixture were molten individually in a copper crucible under argon atmosphere **(Figure 3.2, left).** The produced ingots were cleaned with ethanol and saved in a sterilized environment to avoid any surface contamination. Finally, they were molten together twice to produce a chemical homogeneous large polycrystalline sample of 70 g (**Figure 3.2, right**).

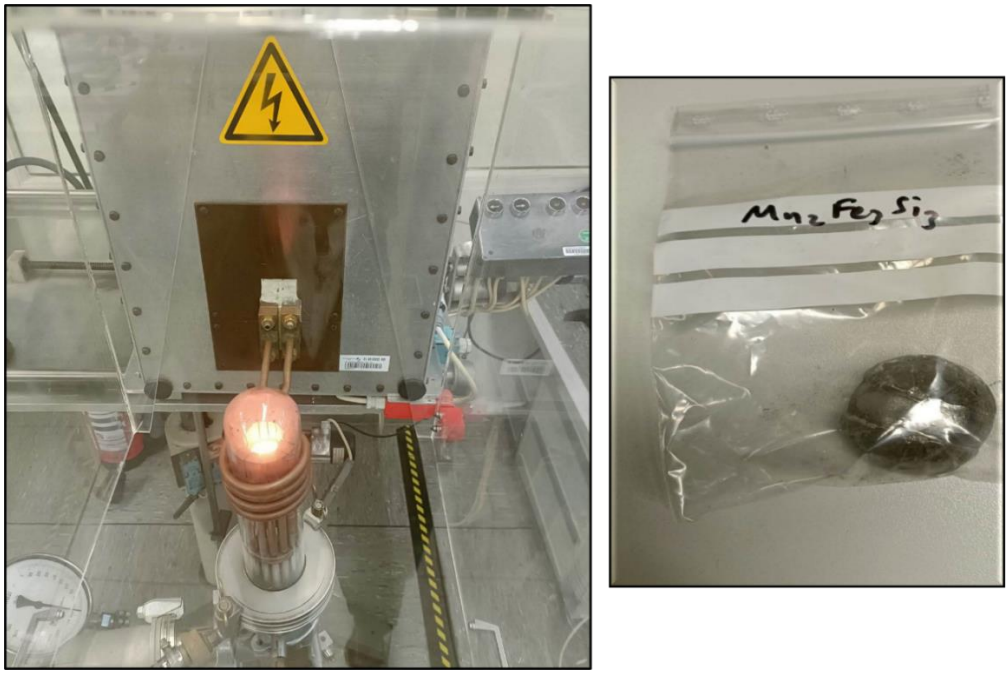

Figure 3.2: The melting process in the cold crucible induction melting apparatus at JCNS, Forschungszentrum Jülich (left) and the produced polycrystalline ingot (right).

3.1.2 Single crystal growth

Large diameter single crystals can be grown by the Czochralski method. This method of pulling single crystals from a melt allows a high quality and low-cost synthesis for research and for industrial applications (Galazka, 2020).

Figure 3.3 shows the setup used to create a single crystal from a previously prepared polycrystalline material using Czochralski technique. The ingot is first melted in a crucible under a controlled atmosphere by induction. It is worthy to mention that the used crucible must have a melting temperature above the melting point of the material. The melt is kept at a temperature above the melting point for a while, the temperature is then lowered to slightly above the freezing point. An oriented seed crystal (a single crystal of the same material or tungsten rod) is used to pull the melt from its surface. The crystal seed is lowered down near to the melt surface, then it is slowly contacted with the melt, while the melt temperature is increased. Then it is pulled upward with a well-defined pulling and rotation speed (Derby, Atherton, & Gresho, 1989; Galazka, 2020).

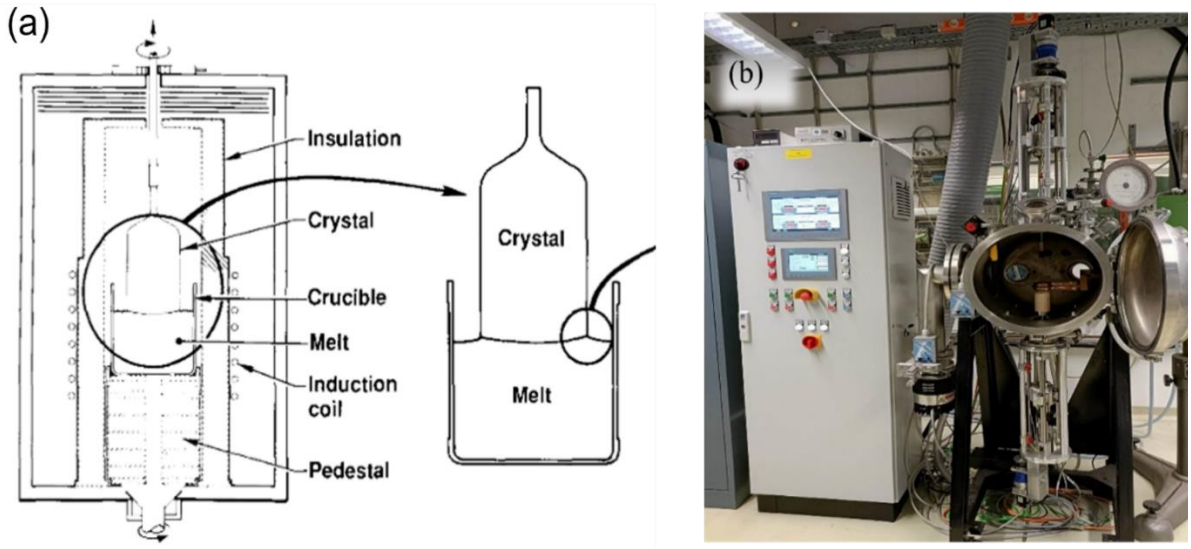

Figure 3.3: (a) a schematic plot illustrating the Czochralski technique (Derby et al., 1989), (b) the apparatus designed and used in JCNS institutes, to produce single crystals based on the Czochralski method.

$Mn_2Fe_3Si_3$ bulk single crystal growth

The previously described polycrystalline of $Mn_2Fe_3Si_3$ specimen, the seed rod, and the crucible cavity were cleaned by ethanol to remove any surface contaminant. The sample was placed in a ceramic (Al_2O_3) crucible and inserted in a tungsten susceptor **Figure 3.4**. The susceptor is surrounded by a single turn of copper coil for inductive heating. An oriented tungsten seed rod, of 3 mm diameter, was attached to the machine at the top of the susceptor. The seed was centred manually. A camera was installed to observe and control the process. After that, the chamber door was closed tightly using a vacuum grease around its boundary, to ensure a good vacuum atmosphere (800 mbar Ar) inside the chamber.

The diameter of the growing single crystal was controlled by manipulating the heating power and the pulling rate along the whole process (Govindhan Dhanaraj, 2010), where the increasing of the power results in reduction of sample diameter. The seed rod was lowered slowly in the melt and the synthesis was started. At the beginning of the growth a low-quality crystal was assumed, so a neck with 2 mm diameter and 20 mm length was created with a relatively high crucible rotating speed of 20 rev/min and seed drawing speed of 15 mm/ h. Then the diameter of the crystal was increased slowly. After the growth of 5 cm two different

grains were observed at the upper part with the noting of a vertical boundary in the crystal. Finally, a cylindrical single crystal was obtained with 10 mm diameter by lowering both the crucible rotation rate (10 rev/min) and the drawing speed to 10 mm/h.

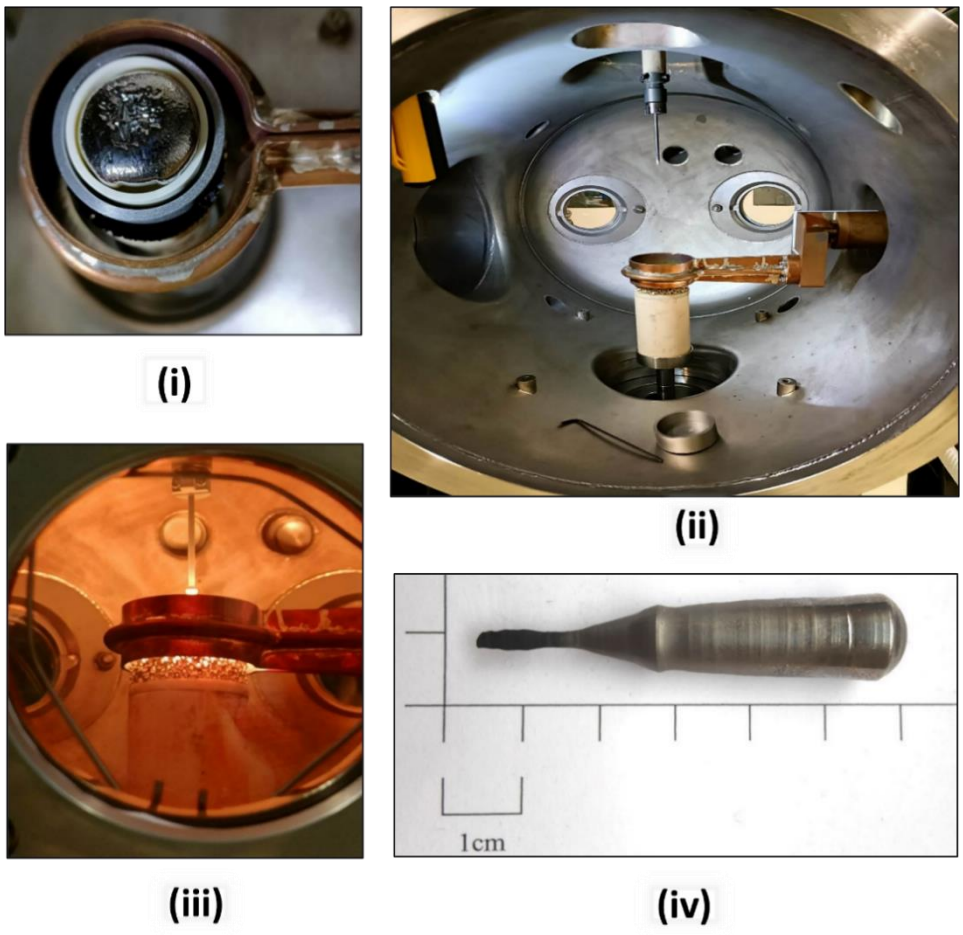

Figure 3.4: The single crystal growth (i) the polycrystalline ingot used as starting material. (Biniskos et al.) Centring of the seed rod inside the chamber. (iii) Pulling of the single crystal from the melt surface. (iv) The produced cylindrical single crystal.

The target was to produce a good-quality single crystal of the $Mn_2Fe_3Si_3$ (x=3) and prepare three different oriented samples for oriented magnetization measurements. Two distinct grains were observed as duplicated points in the Laue patterns. Additionally, the bottom cross section was evaluated as a bad crystal with some different grains. Spark erosion technique was used to cut the lower part, separate the two grains, and then cut small single crystals in specific directions for magnetization measurements.

3.2 Scattering technique

3.2.1 Laue diffraction

The Laue X-ray backscattering method is mostly used for a quick determination of a crystal orientation and symmetry, or as a primary testing to estimate the perfection of a crystal, due to its sensitivity to the impurities (Moffat, 1997).

In this method, a beam of polychromatic (white) X-ray radiation with a continuous wavelength distribution, passes perpendicularly through a photographic film, strikes the surface of a fixed crystal, then is diffracted back to the film by the crystal planes. Each plane results in a diffraction maximum, when an appropriate wavelength from the incident beam is such that constructive interference occurs, i.e., when the path difference between successive waves is an integral multiple of radiation wavelength, according to Bragg's law:

$$n\lambda = 2d_{hkl}\, sin\, \theta \qquad (3.1)$$

where d_{hkl} is the distance between two parallel adjacent lattice planes with Miller indices (hkl), θ is the glancing angle between the incident beam and the reflected planes, n is an integer, and λ is the wavelength of the incident beam (Kittel & McEuen, 2018).

Error! Reference source not found. illustrates the constructive interference of diffracted aves from parallel neighboring lattice planes of a crystal and the recorded 2-dimensional diffraction image on the detector.

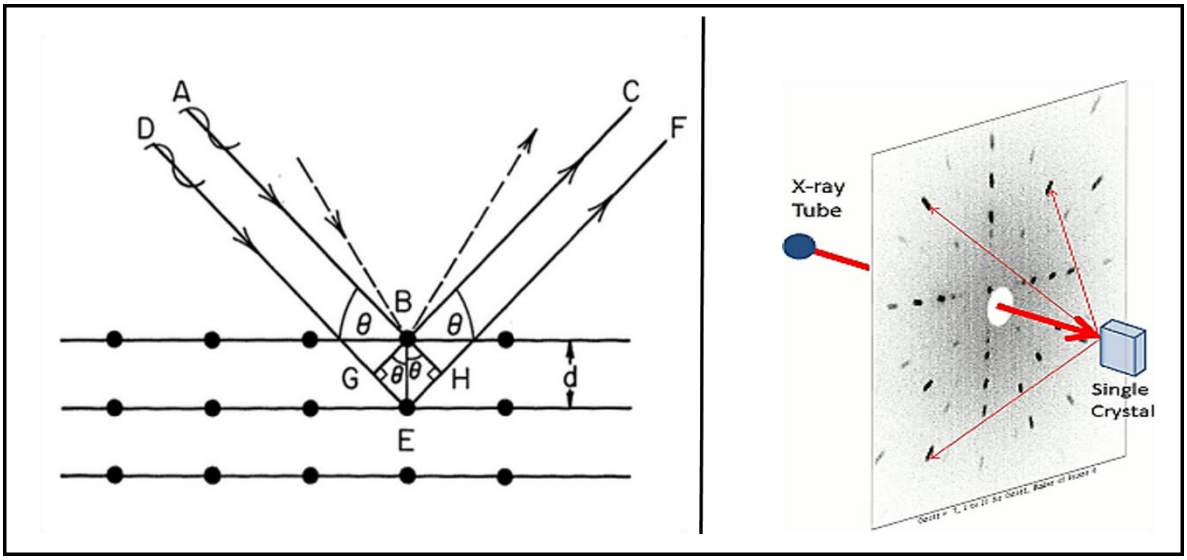

Figure 3.5: (Left) the Bragg condition, with representative lattice planes space d, glancing angle θ (Schwartz & Cohen, 2013) (right) the resulting diffraction pattern by a single crystal using the Laue method (Multiwire Laboratories, 2013).

A Multiwire MWL 120 X-ray Laue detector system, shown in **Figure 3.6,** was used in this study to identify the crystallographic directions. The radiation source is a tungsten X-ray tube. The sample was mounted on a three-axis goniometer, located on a translational stage, at a defined distance from the detector. The system provides a remote controller and is housed inside a radiation protection enclosure. The Laue camera is setup to focus the incoming X-rays onto a crystal and generate a pattern of spots. Different sizes of collimators are used to obtain a suitable spot size for the different samples (Bilderback, 1979). To rapidly characterize the orientation of the sample lattice planes, the device is linked to a computer software to analyze the back-reflected images in real time, using an orientation matrix which connects the information on the orientation of the crystal unit cell with the recorded diffraction pattern.

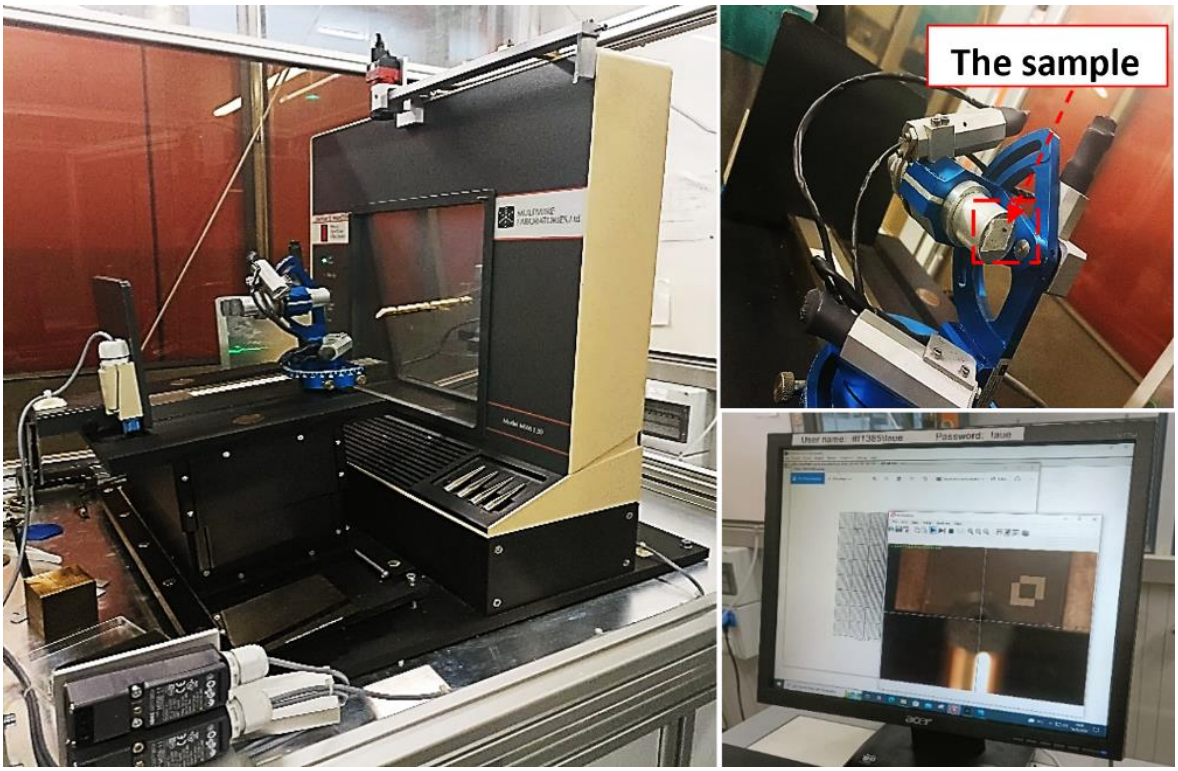

Figure 3.6: Multiwire MWL 120 X-ray Laue detector system (left), sample centering on the goniometer (upper right) and real time image (lower right).

In this work, the samples to be checked and oriented were bulk single crystals of Mn_4FeSi_3 and $Mn_2Fe_3Si_3$. To prepare the sample for the magnetization measurement, the crystal orientations were determined using the Laue method. For this, a suitable collimator with 2 mm diameter, was used. The sample was mounted on a barrel holder and was aligned by the collaboration of the remote controller, Laue camera and the reflecting mirrors.

The orientations corresponding to the three symmetry directions of the hexagonal system ([001], [100], and [120]) were determined this way. The analysis of the produced patterns, using a simulation software, is discussed in the **chapter 4.1**.

Cutting of samples using spark erosion

Spark erosion is a technique used in many industrial applications and research fields to cut samples to small pieces with the highest possible standards. This machinery is based on a process where material is removed from a sample with current discharges between two

electrodes that are separated by a dielectric fluid which works as heat conductor and a cooling agent (Muthuramalingam, Mohan, & processes, 2013). In this process, the electrical energy is converted into heat to melt the targeted area without any physical contact between the sample and the electrode, which means no mechanical abrasion.

Initially, the large crystal was mounted on a holder (goniometer) and oriented along the hexagonal *c*-direction with the help of Laure camera. Then it was glued in proper orientation on the holder at its edges. The electrical contact between the sample and the holder was checked by a voltmeter. Next, the holder was fixed on the stage inside the chamber of the cutting machine. The electrode used here is a thin wire to cut quite small pieces precisely **(Figure 3.7)**. Once the chamber was closed an oily fluid was deposited on the sample until it completely covered the sample. Finally, the power source was turned on. The generated heat in the wire melted the crystal along the wire. The rest of the cuts was done in an equivalent way.

Three samples were oriented and cut with different orientations corresponding to the symmetry directions of the hexagonal unit cell ([001], [100], and [120]) and were thus ready for oriented magnetization measurement.

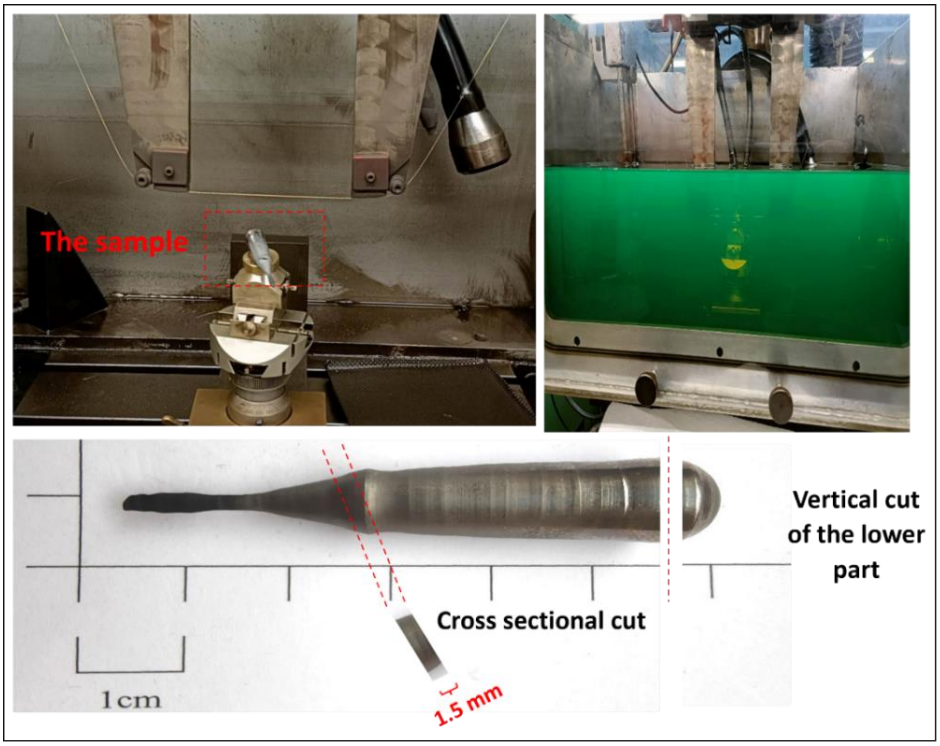

Figure 3.7: Spark erosion process (upper left) centring of the sample along the wire (upper right) the oily fluid covers the sample (lower) a schematic of the first three cuts of the $Mn_2Fe_3Si_3$ sample.

3.3 Magnetization measurement

The Physical Property Measurement System (PPMS) and PPMS DynaCool, with the vibrating sample magnetometer (VSM) option, were used in this study for the DC magnetization measurement of Mn_4FeSi_3 single crystal sample.

The PPMS is a multilateral instrument with versatile capacities to measure macroscopic properties of the material as a function of temperature and magnetic field. Due to its simplicity, accuracy, and variety the PPMS is widely used to measure both magnetic and thermodynamic properties of the specimen under investigation (Burgei, Pechan, & Jaeger, 2003).

Many options of measurement are available, such as heat capacity, electrical resistivity, Hall Effect, and thermal transport. Moreover, DC/AC magnetization and AC susceptibility can be measured with a sensitivity of $\sim 10^{-6}\, emu$. This instrument is capable to change

the temperature continuously from 1.9 K to 400 K and provides a magnetic field range of ±9 T. Furthermore, it can supply temperatures up to 1000 K if a specific oven is used.

The PPMS basically consists of a cryostat with a superconducting magnet coil. In addition to the different software modes, it is provided with various inserts and sample holders to suit the diverse options of measurement and samples. Furthermore, an external Helium supply is connected to cool both the sample chamber and the superconducting magnet.

The Physical Property Measurements in a cryogen-free system (PPMS DynaCool), has all capabilities of the previously described PPMS. Yet instead of the external liquid cryogens, DynaCool has a cryocooler compressor unit (cooled by water), which drives the high-pressure helium cycle for the pulse-tube cooler in the cryostat which cools down both the superconducting coils and the temperature control system and reduces the vibrations on the sample. Due to this setup, it provides better and smoother control for both temperature and magnetic field than the PPMS.

3.3.1 Vibrating Sample Magnetometer (VSM)

VSM is a commonly used option to precisely measure the magnetic moments of magnetic samples. With a relatively large oscillation amplitude (1–3 mm peak) and a frequency of 40 Hz, the system can resolve magnetization changes of less than 10^{-6}emu. It mainly consists of an electromagnet or superconducting solenoid to generate a vertical field in combination with a mechanism to vibrate the sample (linear transport motor). The system is also equipped with an amplifier to enhance the vibrations, pick up coils in close contact to the vibrating sample; to detect the induced voltage, and electronic devices drive the motor and measure the voltage (Buschow & Boer, 2003; Foner, 1959). In addition, there is a special software for controlling the instrument automatically.

As the sample is vibrating along the field axis in the center of the pick-up coils, the magnetic flux changes in its surrounding. According to Faraday's law of induction, the change of flux creates a difference in voltage in the pick-up coils (Schmid, 2008), as shown in **Figure 3.8.**

The time-dependent induced voltage is proportional to the time derivative of the magnetic flux through the coils, the frequency of oscillation, and the magnetic moment of the sample, as seen in the following equation (Design, 2011):

$$Vcoil = \frac{\mathrm{d}\phi}{\mathrm{d}t} = \left(\frac{\mathrm{d}\phi}{\mathrm{d}z}\right)\left(\frac{\mathrm{d}z}{\mathrm{d}t}\right) = 2\pi f C m A \sin(2\pi f t) \quad (3.2)$$

Here Φ is the magnetic flux enclosed by the pickup coil, z is the vertical position of the sample with respect to the coil, and t is time. C is a coupling constant, m is the sample magnetic moment, A and f are the amplitude and oscillation frequency, respectively {Design, 2011 #88}.

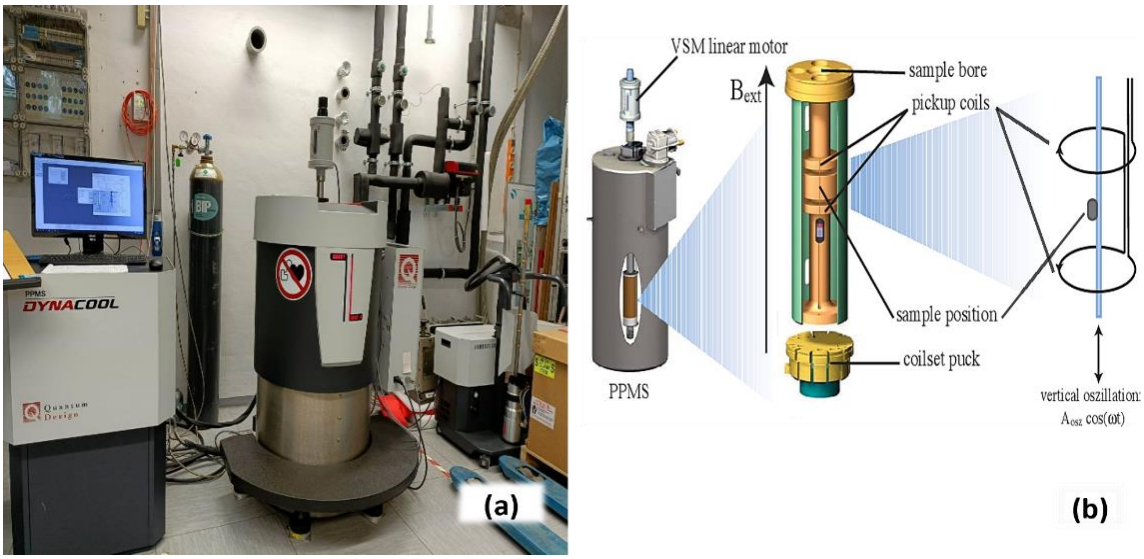

Figure 3.8: (Left) PPMS DynaCool at JCNS-2 and (right) Schematic drawing of the VSM option (Schmid, 2008).

3.3.1.1 Sample Preparation for magnetization

At the beginning of each magnetization measurement, the sample was prepared following some general steps. First, the sample and an appropriate vespel holder, has only a small background signal, were cleaned by isopropanol to remove surface impurities.

The sample mass was measured precisely with an electronic balance, in order to be used in the calculation of the magnetization. The recorded mass of the sample of Mn_4FeSi_3 was 15.6± 0.1 mg. Moreover, the dimensions of the sample were approximately determined as 1.5 mm× 1.5 mm× 1 mm.

The sample was mounted on the holder using a special station with a scale. The sample was centered 35 ±3 mm from the holder's bottom; to ensure the correct position inside the pickup coil, **(Figure 3.9, a).** At the beginning of the magnetization measurement the sample offset is checked by applying a small field, e.g.,100 Oe at room temperature, see **Figure 3.10.** It is worth emphasizing that the requested direction is always oriented parallel to the applied magnetic field of the instrument. Ge7031 varnish was used to adhere the sample rigidly to its holder and was put under light for ~30 minutes; to make sure that the varnish dried well, (**Figure 3.9, b).** This way it was secured that the sample would not move at high acceleration during the measurement.

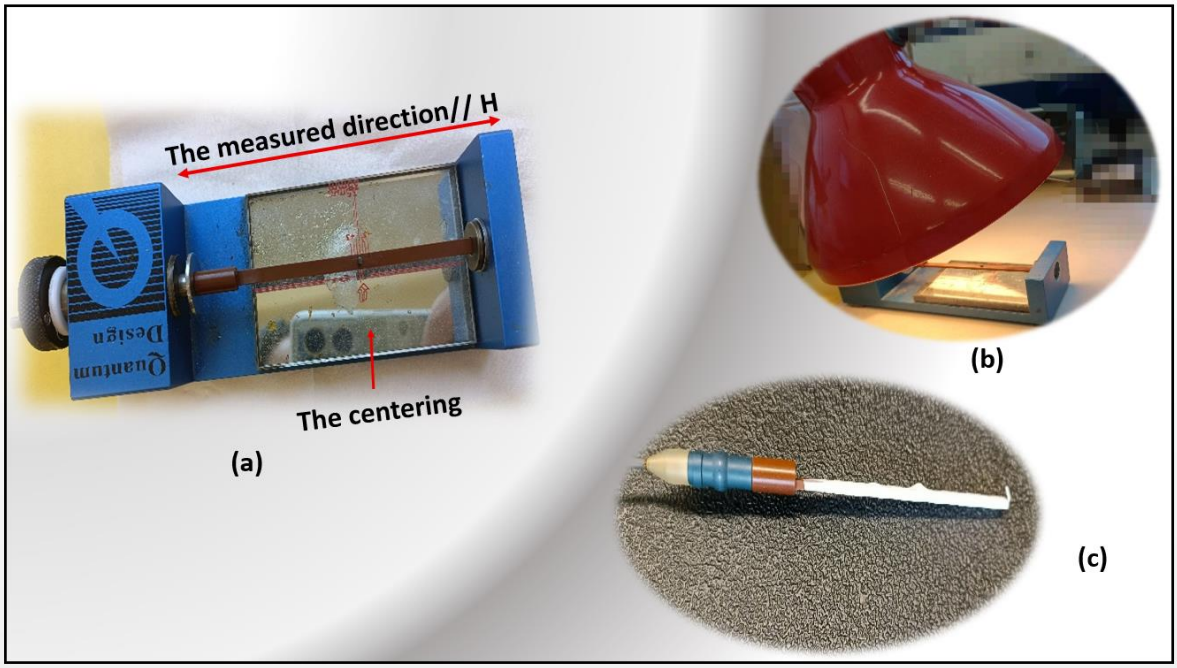

Figure 3.9: The sample preparation procedure. (a) Centering the sample on its holder using the mounting station (b) the sample under light to be dried (c) rapping the sample by Teflon.

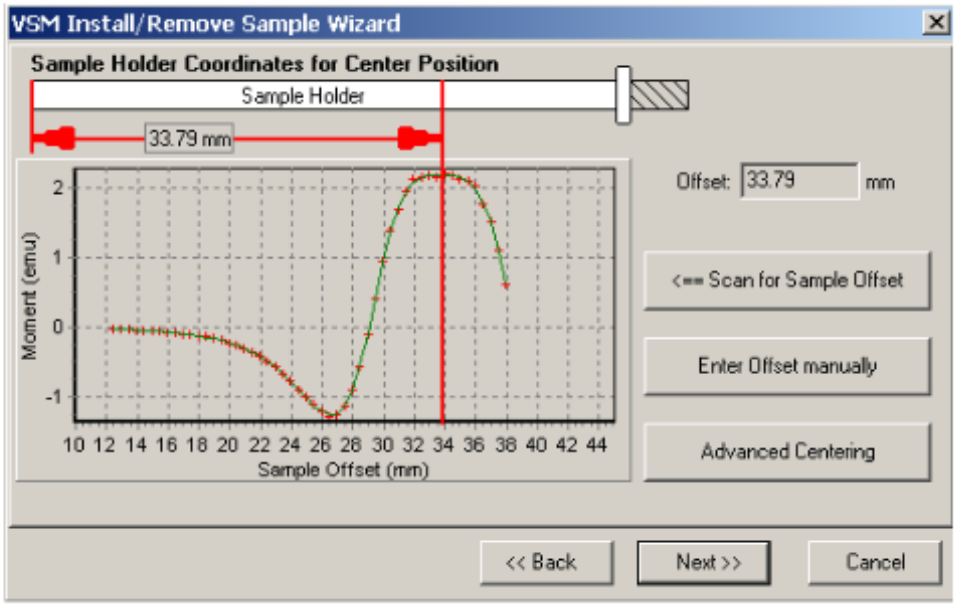

Figure 3.10: The sample installation wizard, an example of a sample offset scan (Design, 2011).

At the end, the sample was covered with Teflon tape, **(Figure 3.9, c).** Then, the holder was attached to the sample rod of PPMS and becomes ready to be measured by PPMS/ DynaCool.

3.3.2 Measurement procedure

The magnetization measurement was performed following two different protocols, the isofield and the isothermal measurement. Several isothermal measurements were carried out, with a slightly changed protocol to obtain optimized data. Subsequently, the isofield measurement were performed for two reasons; to check some observations, and to compare the results of isofield and isothermal measurements and to examine the dependency of the results on the procedure. Both PPMS and PPMS DynaCool were used alternatively according to the beamtime schedule. The details of these experiments will be provided in the following sections.

3.3.2.1 Isothermal Measurements

The magnetic moment was measured as a function of magnetic field. The isothermal measurements were implemented by applying a magnetic field 8 T to -8 T. The sample was

kept at constant temperature while the hysteresis loop was running. The measurements were performed by applying the field parallel to a specified crystallographic axis. Three crystallographic directions were selected, considering that they are the symmetry directions in the hexagonal system. The details of the protocol are provided in **Table 3.1** which gives the temperature step size for each temperature range and orientation. **Table 3.2** shows how the field was changed at each temperature (mode/ rate), and the field increment.

Orientation	Temperature range	Temperature step
[001]	350-110	10
[001]	110 – 90	3
[001]	90 – 80	1
[001]	80 – 8	3
[001]	8 – 2	1
[100]	350- 110	10
[100]	110- 95	3
[100]	90 - 81.5	1.5
[100]	77 – 8	3
[100]	8 – 2	1
[120]	110 – 90	3
[120]	90- 80	1
[120]	80 – 8	1

Table 3.1: Isothermal magnetization measurement protocol with temperature increment in each temperature range.

To illustrate the procedures the first isothermal experiment which was done using the PPMS will be described in more detail here. In this measurement, the temperature was decreased from 110 K to 8 K at rate of 5 K/ min, in 35 steps. This means that the temperature was reduced 3 K each step and the hysteresis loop was applied at each fixed temperature. The magnetic field was varied in three intervals.

First, the field changed from 8 T to 0.5 T with a rate of 150 Oe/sec on a driven mode of 1000 Oe, so that the field changes between the two recorded points uniformly as 1000 Oe. ‘Driven’ means that the field is stabilized at the set point before the magnetic moment is measured.

Second, the field was changed continuously from 0.5 T to – 0.5 T in a sweep mode with a rate of 50 Oe/sec. At this lower rate, the magnetic moment is measured, while the field is varied, as the field change during the measurement is small as the respective change of the moment. Third, the field decreased from – 0.5 T to – 8 T with a sweep rate of 150 Oe/sec (driven mode of 1000 Oe). The process was reversed from –8 T back to 8 T following the same steps.

Orientation	**Temperature range (K)**	**Field range (T)**	**Mode (Sweep/ Driven)**	**Rate (Oe/s)**	**ΔH**
[001]	110 - 2	(8 - 0.5) (-0.5 --8)	Driven	150	1000
		(0.5 --0.5)	Sweep	100	-
	350 - 110	(8 - 0.5) (-0.5 --8)	Sweep	150	1000
		(0.5 --0.5)	Sweep	50	-
[100]	110 - 2	(8 - 0.5) (-0.5 --8)	Driven	150	1000
		(0.5 --0.5)	Sweep	50	-
	350 - 110	(8 - 0.5) (-0.5 --8)	Sweep	150	1000
		(0.5 --0.5)	Sweep	50	-
[120]	110- 8	(8 - 0.5) (-0.5 --8)	Driven	150	1000
		(0.5 --0.5)	Sweep	50	-

Table 3.2: Isothermal magnetization measurement protocol for the descending branch of the hysteresis loop.

Due to an abnormal change of magnetization curves slope, which was observed at high fields (>3 T) between 80 and 90 K, this region was afterwards re-measured taking smaller steps (change of temperature between two points is 1 K) to get better data resolution.

In this sequence, a command "VSM locate by touchdown" was added for re-centering the sample at each temperature and loop. This ensures that the sample stays centered as the temperature varies.

3.3.2.2 Isofield Measurements

In the isofield measurements, the magnetic moment was measured as a function of temperature. The measurement was realized by cooling the sample at a fixed magnetic field. Six isofield measurements were performed with some slight changes in the protocol, as necessary. The details are provided in **Table 3.3**.

Orientation || H	Field (T)	Temperature range (K)	Sweep rate (K/min)	Instrument
[001]	0.5	300 – 10	2	PPMS
[001]	1	300 – 2	1	DynaCool
[001]	7.9	300 – 2	1	DynaCool
[100]	0.5	350 – 2	1	PPMS
[100]	1	350 – 2	1	PPMS
[100]	7.9	350 – 2	1	PPMS

Table 3.3: Protocol of the isofield magnetization measurements

As an example, the first isofield measurement will be briefly described here. The sample was cooled from room temperature to 10 K at a field of 0.5 T was applied parallel to the *c*-direction [001]. The temperature was swept continuously with a rate of 2 K/min.

Chapter 4 Data Analysis

4.1 Laue analysis of Mn_4FeSi_3

The symmetry directions of the single-crystalline Mn_4FeSi_3 sample were determined using the real-time back reflection images produced by Laue camera. First, prominent sample surfaces were identified and numbered as seen in **Figure 4.1.** The crystal was mounted on the holder where the first face (1) was oriented in the direction of the incoming beam and the first pattern was recorded, as described in **chapter 3.2.1**, then it was rotated to record the patterns for other faces. Three different spot patterns along the main symmetry directions were recorded by the Laue camera and compared with simulated patterns. For the simulations, the space group and lattice parameters of the compound were defined in the WinLaue software (JCrystal, 2018). The simulated patterns were then calculated for the three viewing directions of the hexagonal unit cell ([001], [100] and [120]).

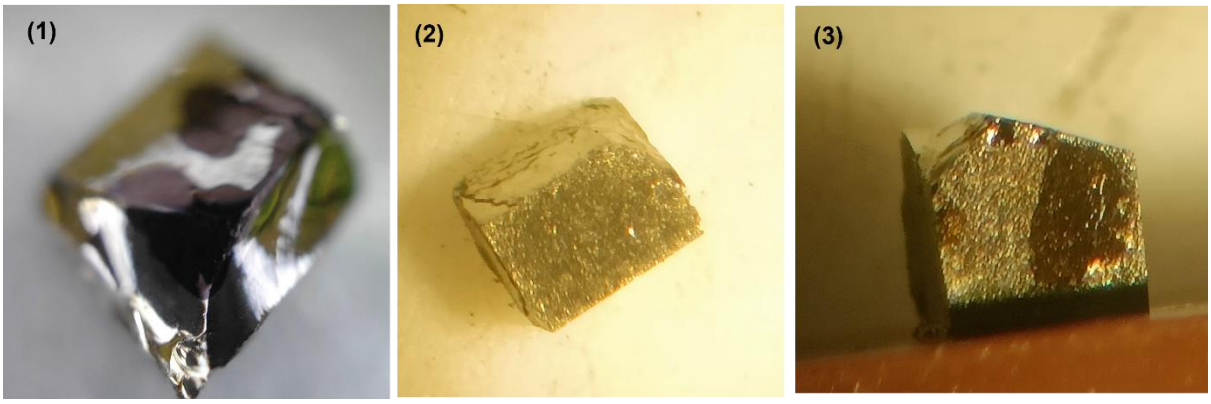

Figure 4.1: Top view of Mn_4 Fe Si_3 sample faces. The numbering is to distinguish them to determine the crystallographic orientations.

The obtained stereographic projection from the simulations and the experimental Laue patterns were then compared by measuring and identifying the angles between the diffraction spot and the reference axis (shown in blue), **Figure 4.2.**

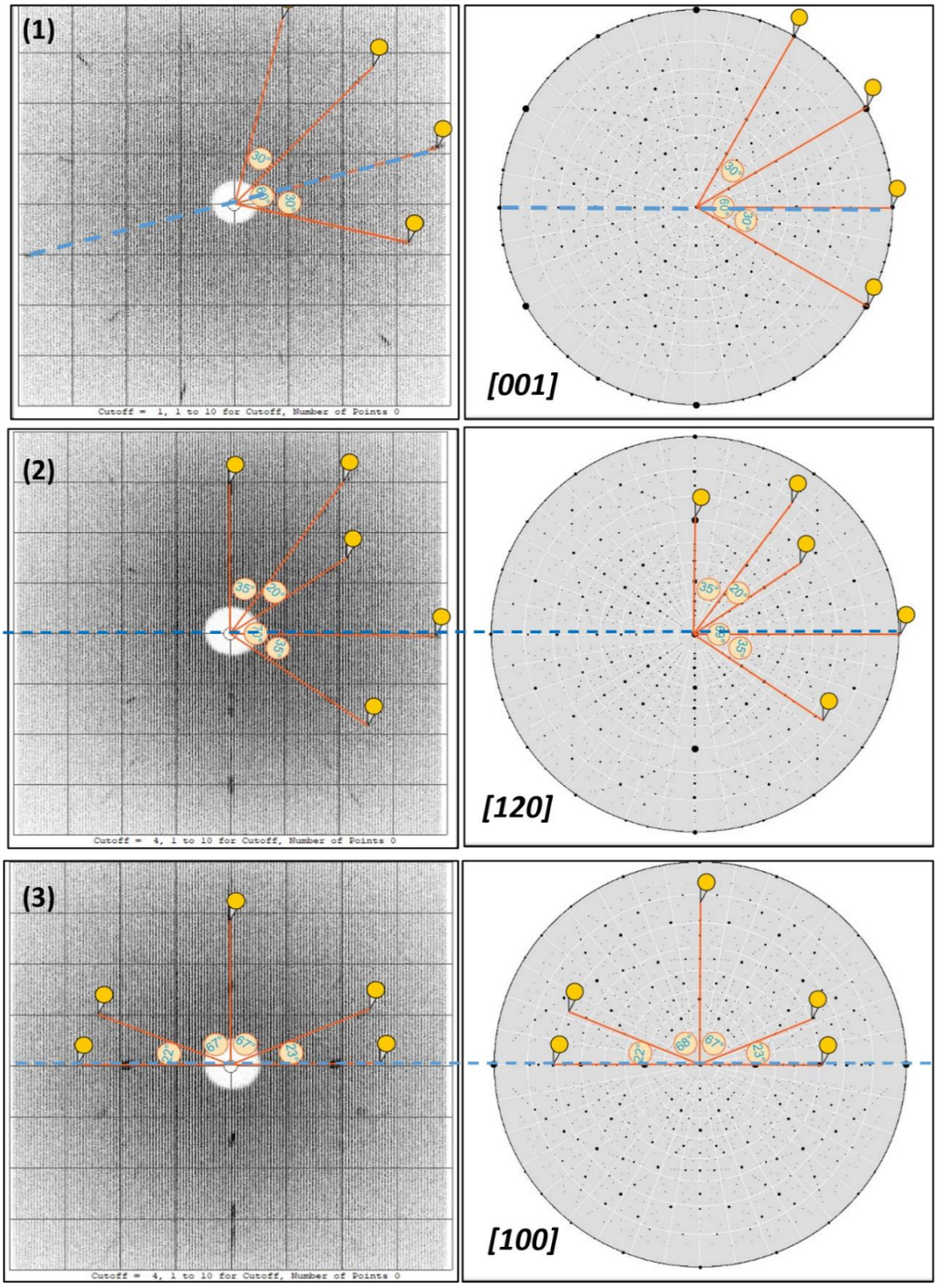

Figure 4.2: Identification of the symmetry directions of the Mn_4FeSi_3 single crystal based on the Laue patterns (left) and the simulated stereographic projections (right) with orientations parallel to [001] [120] and [100]. The yellow dots point to the reflection points. The dashed blue line is the reference axis.

4.2 Magnetization measurements

4.2.1 Paramagnetic region and Curie-Weiss analysis

The Curie-Weiss law describes the paramagnetic behavior of *4d* rare earth and *3d* transition metal compounds. Materials with the best adherence in, which exist in a magnetically disordered gas-like state at relatively high temperatures.

The molar magnetic susceptibility χ of Mn_4FeSi_3 at each temperature was calculated using the mass magnetization obtained from the isofield measurements. In **Figures (4.3, 4.4)** the inverse magnetic susceptibility χ^{-1} is represented as a function of temperature.

The curves were fitted to the linear regimes of the high temperature regions for two different isofield measurements measured with fields of 1 T and 7.9 T. In these measurements on the pre-oriented single crystal, the field H was applied || [100] (**Figure 4.3**) and || [001] (**Figure 4.4**). From the fit of the Curie-Weiss law, taking $\mathcal{X}^{-1}$ in equation (**2.5**), the Curie constant ***C*** is calculated from the inverse of the slope and the Curie-Weiss temperature θ_{cw} is determined as the intercept of the interpolation of the fitted curve on the *x*-axis. The effective magnetic moment per unit ion μ_{eff} (in units of Bohr magnetons, μ_B) is calculated using the formula (**2.6)** as ($\mu_{eff} = 798\sqrt{C/5}$). The values are calculated taking different temperature ranges above Neel temperature T_N, at different magnetic fields. The minimum is changed while the maximum is fixed at 350 K (H || [100]) and at 300 K (H || [001]) as shown in **Table 4.1.**

If one inspects the inverse susceptibility as a function of temperature for H || [100], the behavior seems to be linear from 280 to 350 K, i.e., the Curie- Weiss is followed for both the low and high fields in this temperature range (**Figure 4.3**).

On the other hand, when the H || [001], the deviation from the Curie-Weiss behavior strongly depends on the applied field. With applying a low field 1T, the curve is only linear in the temperature range (280-300) K. In contrast, if a much higher field 7.9 T is applied along this direction, the inverse magnetic susceptibility shows a linear behavior down to a temperature of ~100 K (**Figure 4.4).**

As seen from **Table 4.1**, θ_{cw} does not change strongly with changing the fitting temperature range at a fixed field, but it changes by field. If H || [100], θ_{cw} changes in a small range between -77 K and -80 K. If the field is || [001], θ_{cw} alternates between -99 K and -113 K by increasing the field. One can conclude that the Curie-Weiss temperature is field dependent. This indicates the differ of

the strength of the molecular field and the magnetic correlations, whereas the absolute θ_{cw} with H || [001] is higher than that with H || [100].

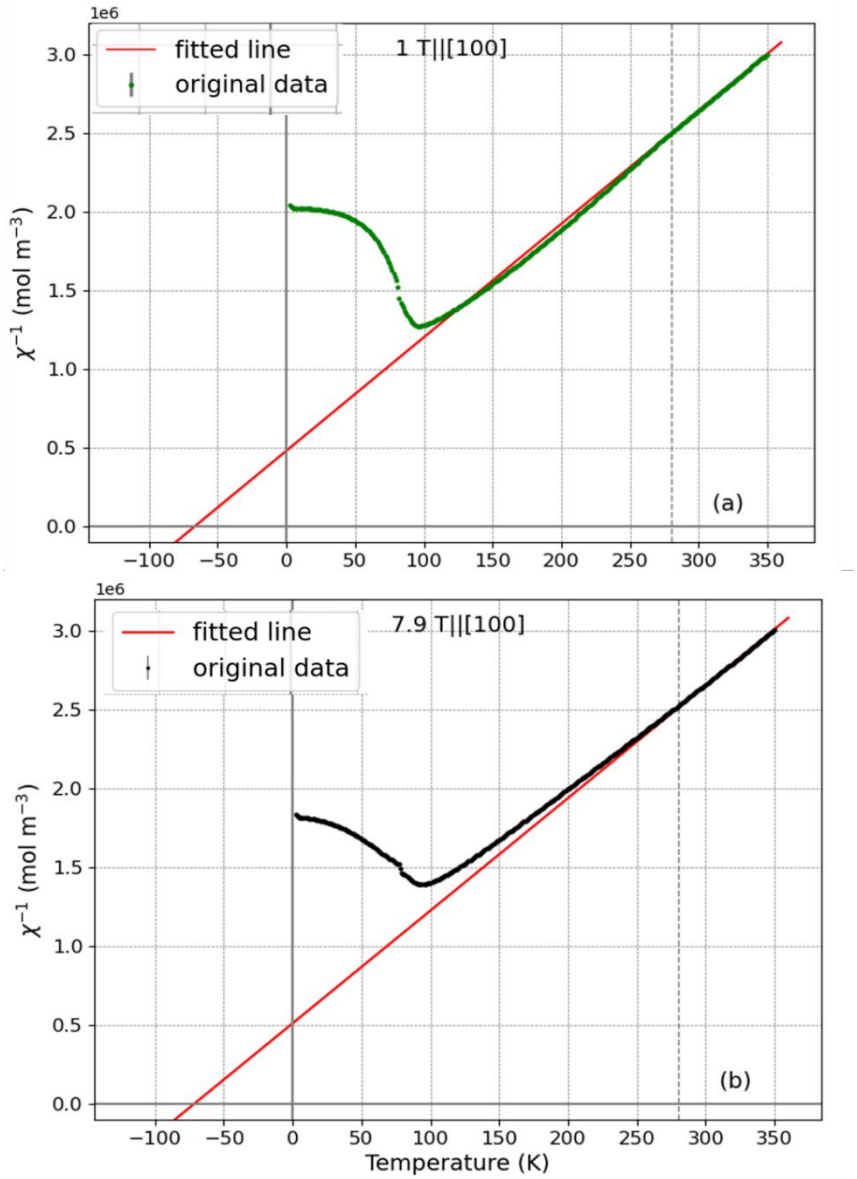

Figure 4.3: Inverse susceptibility of Mn_4FeSi_3 as a function of temperature (green) with a field of 1 T || [100] (black) with a field of 7.9 T || [100]. The red line is the Curie-Weiss fit to the data in the temperature range (320< T< 350) K.

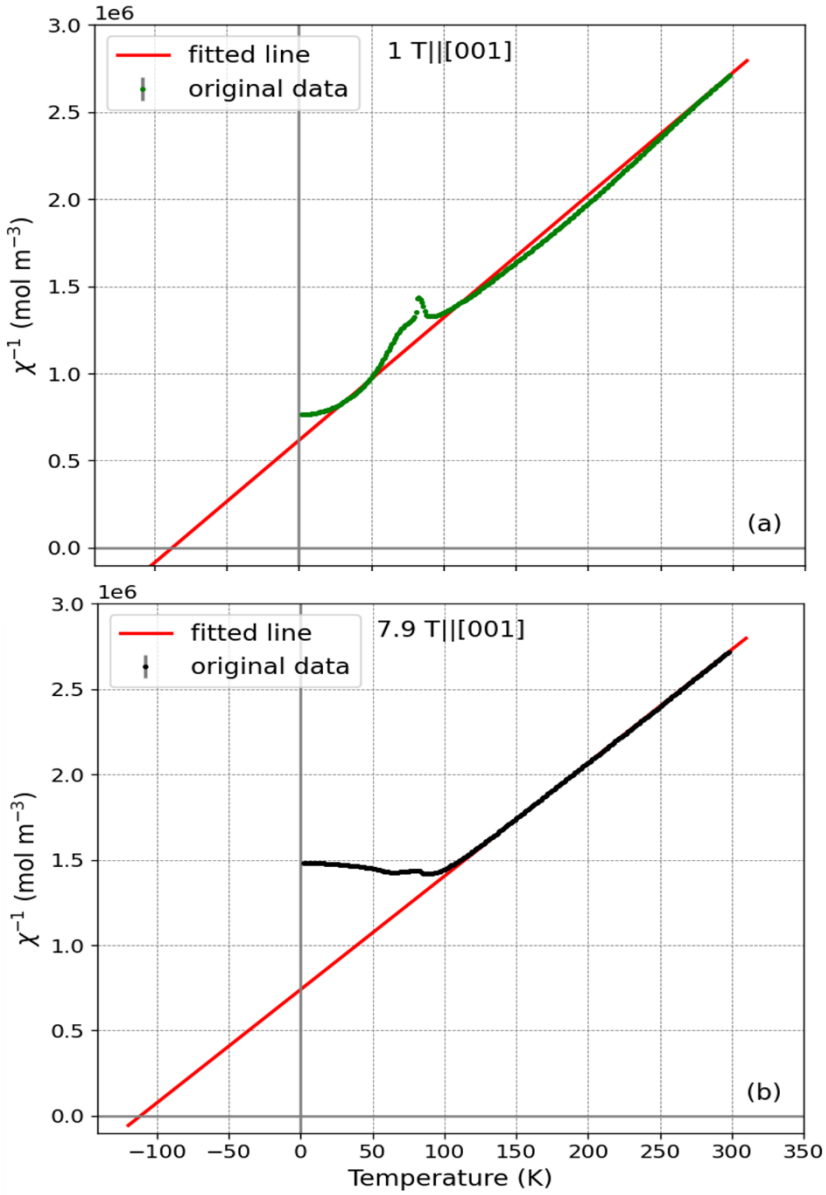

Figure 4.4: Inverse susceptibility of Mn_4FeSi_3 as a function of temperature (green) with a field of 1 T || [001] (black) with a field of 7.9 T|| [001]. The red line is the Curie- Weiss fit to the data in the temperature range (292< T< 300) K and (280 < T< 300) K for the 1 T data and the 7.9 T data, respectively.

To summarize, below 280 K the curves deviate from Curie- Weiss behavior for a field applied along the [100] direction. This deviation is field independent. If the field is applied along the [001] direction, the deviation shifts to much lower temperature with higher fields. The evaluated μ_{eff} ~4.24(4) μ_B and 4.3(1)μ_B with H || [100] and [001], respectively.

$\mu_0 H$ (T)	0.5		1.0		7.9	
Direction	**H || [100]**					
Temperature range (K)	θ_{cw} **(K)**	μ_{eff} **(μB)**	θ_{cw} **(K)**	μ_{eff} **(μB)**	θ_{cw}**(K)**	μ_{eff} **(μB)**
290 – 350	-79	4.27	-77	4.22	-79	4.27
300 – 350	-79	4.28	-77	4.21	-78	4.26
310 – 350	-80	4.30	-77	4.20	-78	4.24
320 - 350	-80	4.30	-76	4.20	-77	4.22
Average value	-79.5	4.29	-76.8	4.21	-78	4.25
Standard deviation	0.6	0.02	0.5	0.01	0.8	0.02
Direction	**H || [001]**					
Temperature range (K)	θ_{cw} **(K)**	μ_{eff} **(μB)**	θ_{cw} **(K)**	μ_{eff} **(μB)**	θ_{cw} **(K)**	μ_{eff} **(μB)**
280 – 300	-99	4.10	-105	4.30	-112	4.38
284– 300	-100	4.10	-106	4.30	-112	4.38
288– 300	-101	4.20	-107	4.30	-112	4.39
292 - 300	-100	4.20	-109	4.32	-113	4.41
Average value	-100	4.15	-106.8	4.31	-112.3	4.39
Standard deviation	0.82	0.06	1.71	0.01	0.5	0.01

Table 4.1: The experimental θ_{cw} and μ_{eff} at different temperature fit ranges and different fields with H || [100] and H || [001].

For both directions, a clear anomaly in $\chi^{-1}$is around 95 K, which corresponds to the transition temperature from PM to an AF ordered phase. A comparison of the obtained Curie Weiss temperatures with T_N, shows comparable values for both.

The theoretical μ_{eff}, determined assuming only localized spins on the transition metal ions using formula **(2.7)**, is 5.7 μ_B. The μ_{eff} obtained from the Curie Weiss fit is significantly lower than the theoretical value and in agreement with earlier studies on this compound (Herlitschke et al., 2016).

4.2.2 Magnetization Measurements with low fields (0- 3) T

Due to the observed field dependent magnetic response, it is convenient to divide the following discussion into two sections. The first one, concentrates on the features obtained by applying low field ≤ 3T, and the second on the features observed under high fields between ≥ 3T. Moreover, the magnetization data is separately analyzed for fields applied parallel to [001] and parallel to [100].

4.2.2.1 Magnetization Measurement with low field along [001]

a) Field-dependence of magnetization based on isothermal measurement with H || [001]

For the isothermal measurements the protocol, described in **chapter (3.3.2.1)**, the field was changed from 8 T to -8 T. The mass magnetization was calculated in units of (Am^2/kg) and is represented as a function of the field flux $\mu_0 H$ in **Figure 4.5**. To better illustrate the observations, the curves are divided into two parts, the first one corresponding to the temperature range between 8 K and 110 K (**Figure 4.5**, **left**) and the second one corresponding to the higher temperatures from 120 K to 350 K (**Figure 4.5**, **right**). Throughout the following discussion, two different color gradient maps are used for the two temperature regions.

At the low fields region (**Figure 4.5, left)**, the curves diverge from a linear response for the low field range from +3 T to -3T for temperatures < 80 K. This reflects a magnetization change in this temperature region and leads to magnetization differences between the isotherms. On the other hand, for the high temperature region above 110 K (**Figure 4.5, right**), the kink in the isotherms, near to zero field, disappears with increasing temperature, and the curves converge till they meet at zero. In other words, for higher temperature the magnetization goes to zero as the field goes to zero.

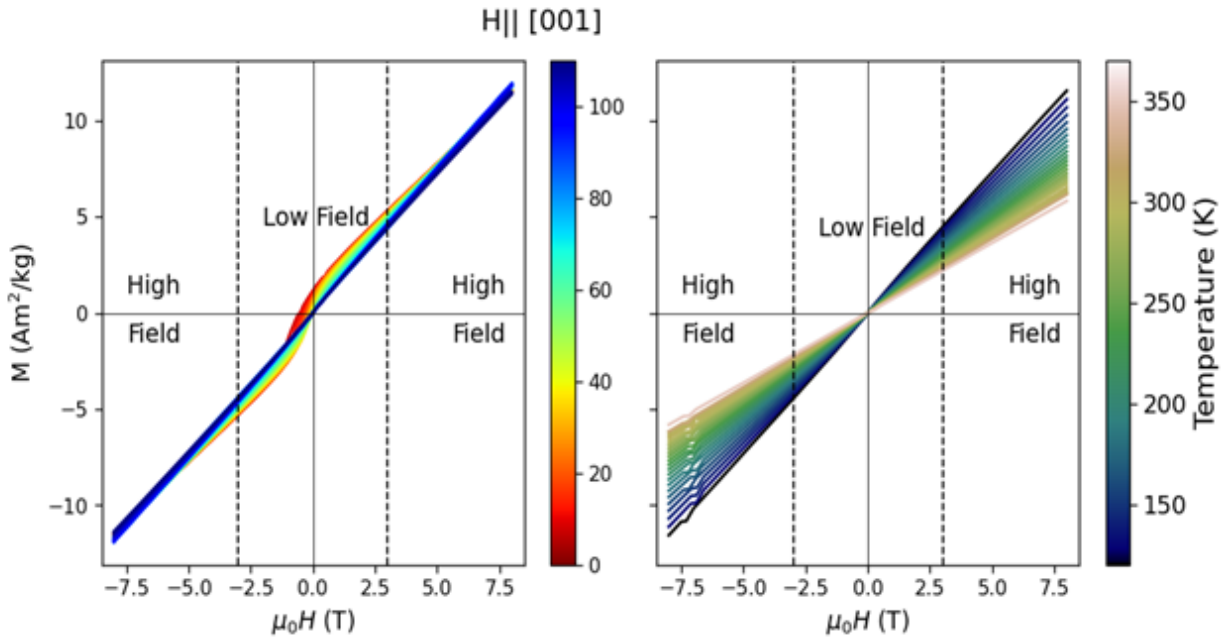

Figure 4.5: Isothermal measurements of Mn_4FeSi_3, with H || [001]. (Left) for the temperature range (8-110) K, and (right) for temperature range (110-350) K. The line colour indicates the temperature of the isothermal measurement. The data has been re-binned with a temperature step of ΔT= 1 K and a field step of $\mu_0\Delta H = 0.1$T.

For a better visualisation of the curves' behaviour, the derivative $\frac{dM}{dB}$ was calculated from the descending field branch and plotted vs $\mu_0 H$ (**Figure 4.6**). This way one clearly observes a strong peak around zero field. It is obvious that the peak is temperature dependent, as the maximum changes its height and moves towards higher fields with decreasing temperature. The highest peaks are observed in the lowest temperature region between < 50 K. (**Figure 4.6, a**). With decreasing temperature, the peak shifts towards the negative fields, while with increasing temperature the peak maxima are decreased.

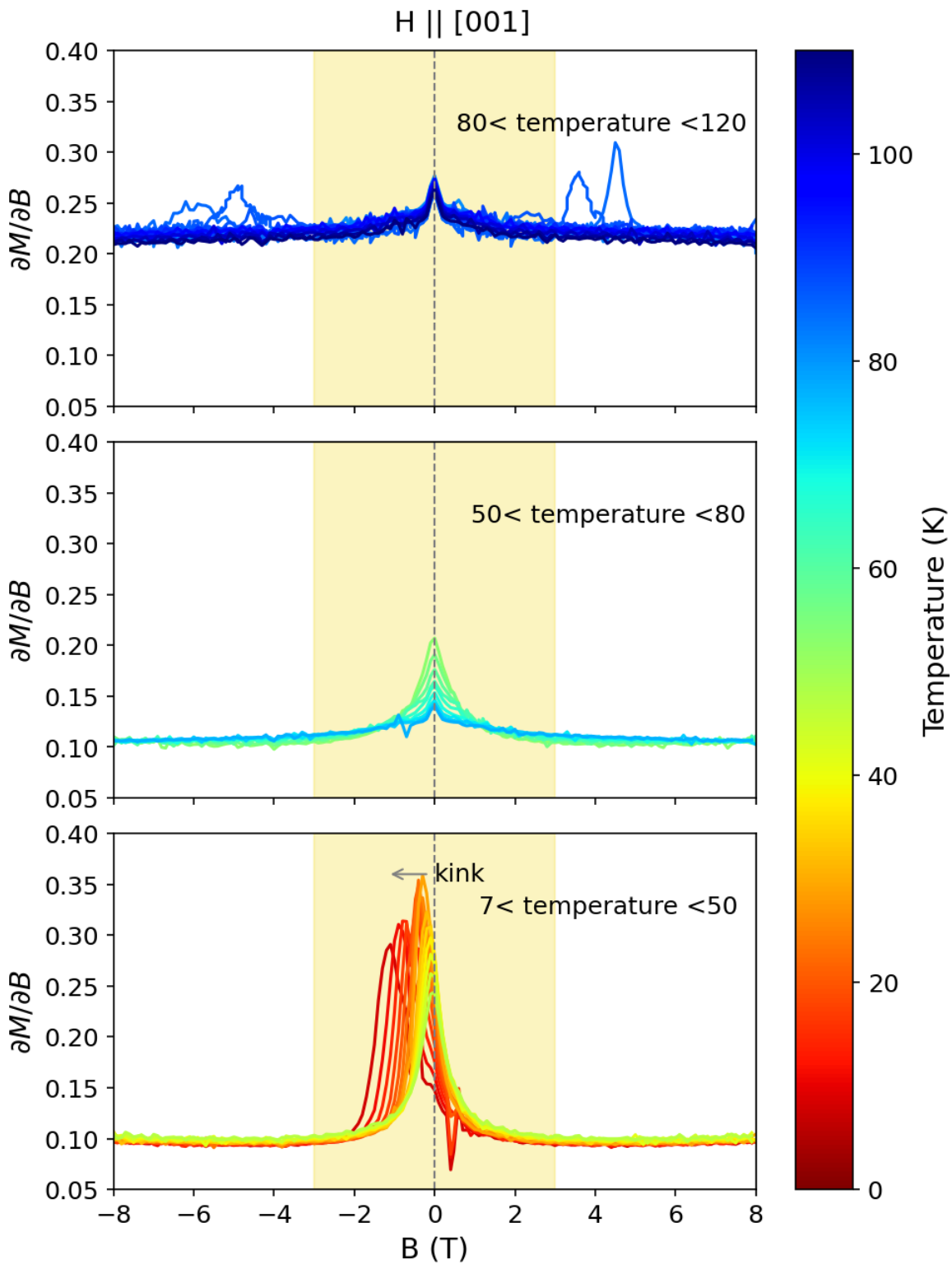

Figure 4.6: $\frac{dM}{dB}$ (×20) as a function of magnetic field || [001] calculated from isothermal measurements of Mn_4FeSi_3 at temperatures (8-110) K. The low field region is highlighted in yellow. The temperature ranges (a) (80< T<120) K (b) (50< T<80) K and (c) (7< T<50) K. The data has been re-binned with ΔT= 1 K and ΔB = 0.1 T.

A close up of the low-field low-temperature region **Figure 4.7**. which shows M(T) curves for selected temperatures below 65 K. Both branches of the hysteresis loop are represented (solid lines: decrease of field from +3 T to -3 T; dashed lines: increase of field from -3 T to +3 T). The opening of a hysteresis loop is clearly visible and increases with decreasing temperature. The two branches of the hysteresis loop are symmetrical around the *y* axis.

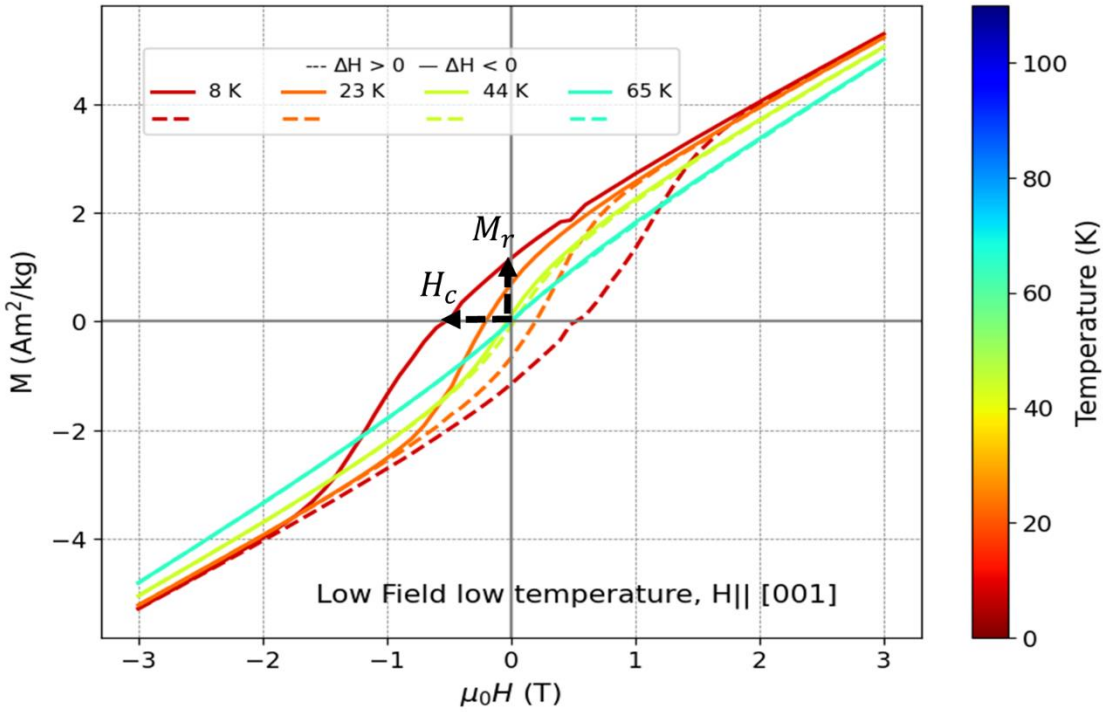

Figure 4.7: M (B) curves corresponding to selected temperatures for the low- field (H || [001]) low-temperature region. Solid lines are extracted from the descending field branch of the hysteresis loop (ΔH < 0); dashed lines correspond to the ascending branch (ΔH > 0). Data has been rebinned with ΔT= 1 K and $\mu_0 \Delta H$ = 0.1 T.

The absolute coercive field and the remnant magnetization are represented as a function of temperature in **(Figure 4.8).** The coercive field $\mu_0 H_c$ **(Figure 4.8, top)** was determined for each temperature as the field value at which the sign of the magnetization changes. The green squares represent $\mu_0 H_c$ from the ascending branch ($\mu_0 \Delta H > 0$), while the red squares are from descending field branch ($\mu_0 \Delta H < 0$). It can be clearly seen, that the coercivity is increasing with decreasing temperature below 60 K. This indicates a ferromagnetic contribution, which becomes stronger at low temperatures and low fields.

The remanence M_r was determined taking the value of the magnetization at almost zero field**.** With the field || [001], the residual strength grows below 60 K and does not saturate at lower temperatures.

Values obtained from the ascending field branch (the green symbols) basically coincide with those from the descending branch (the red symbols).

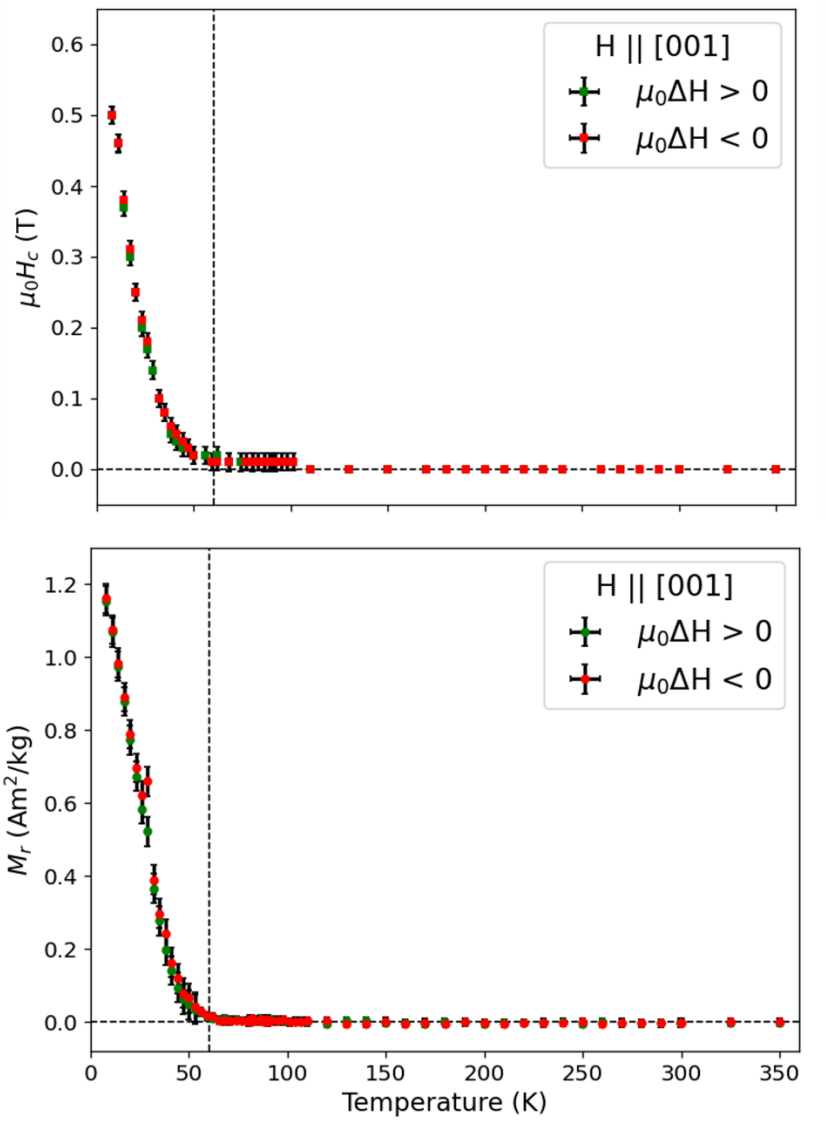

Figure 4.8: Top: The absolute value of the coercive field $\mu_0 H_c$ as a function of temperature with H || [001]. Bottom: The absolute remnant magnetization M_r as a function of temperature. Green and red symbols represent the ascending and descending field branches, respectively. (ΔT= 1 K, μ₀ ΔH= 0. 01 T).

b) Temperature-dependent magnetization with H || [001]

The temperature-dependent magnetization was measured by isofield measurements, while cooling the sample continuously from the room temperature to 2 K at a sweep rate of 1K/min, under a fixed magnetic field || [001]. M/B (T) curves are for selected small fields in **Figure 4.9**. Curves measured under isofield conditions are shown on the left, while curves extracted from the isothermal measurements are shown on the right. The curves for both branches of the hysteresis loop coincide well **(chapter A.2),** then the ascending branch data is shown. Data has been re-binned with a temperature step of 1 K and a field step of 0.01 T for isothermal measurement.

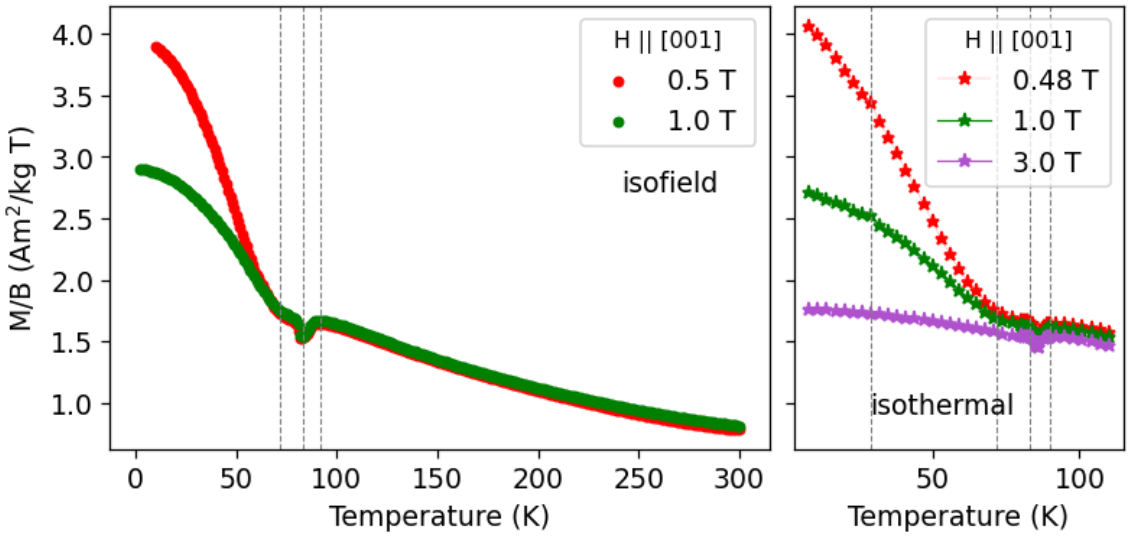

Figure 4.9: The M/B curves as a function of temperature. (Left) Curves from isofield measurements for fields of 0.5 T and 1 T applied along [001] (sample was cooled from 300 - 2) K. (Right) Curves extracted from the descending branch of the hysteresis loop at fields of 0.48[2] and 1 T for temperature range (110 – 8) K. The data has been re-binned with ΔT= 1 K and ΔB = 0.01 T for isothermal measurement, and with ΔT= 1 K for the isofield measurement.

As can be seen, the curves portrayed in **Figure 4.9** show comparable features. However, the isofield measurement covers a broader temperature range reaching down to very low temperatures (< 8 K),

[2] A field of 0.48 T was chosen instead of 0.5 T, due to the noise noticed in the 0.5 T measurement. This is related to the change of the field sweeping mode, from a discontinuous mode of 1000 Oe step size above 0.5 T to a continuous mode between 0.5 T and -0.5 T. The overlap between the recorded data points at the boundary leads to noise in the magnetization curves.

and comparatively high temperatures (> 110 K). On the other hand, the curves extracted from the ascending branch of the hysteresis loop (isothermal measurements) allow a comparison between three selected fields in the low field region.

In the high temperature region **Figure 4.9 (left),** the magnetization increases as the temperature goes down to 92 K then it approximately stays constant till 88 K. This observation is related to the transition from a magnetically disordered PM phase to AF state of the material at a temperature of 92 ± 3 K. A clear dip occurs between 88 K and 80 K. At fields of 0.5 T and 1 T, the curve increases slightly down to the dip < 80 K, followed by a strong increase below 65 K. This increase slows down at higher fields. Below 40 K, the increase rate gets smaller with decreasing temperature at all applied fields and is further reduced by a higher applied field (**Figure 4.9, right**).

4.2.2.2 Magnetization Measurement with low field along [100]

a) Field-dependence of magnetization based on isothermal measurement with H ||[100]

At first sight the magnetization data shows no significant differences between the curves obtained with H || [100] and H || [120] **(chapter A.1).** Thus, the magnetization curves with field || [100] are presented only. The field-dependent magnetization curves with field changes from -8 T to 8 T at different temperatures from 110 K to 8 K, are illustrated in **Figure 4.10**. The M(B) curves correspond to the field descending branch ($\Delta H < 0$) of the hysteresis loop with field applied parallel to [100]. In this section, the low field region, (-3 T to +3 T), features will be presented and discussed.

If one focuses on the low field region, a clear inflection point at zero field is visible for all temperatures (inset in **Figure 4.10**). If one moves from ±3 T to 0 T, the magnetization curves converge and intersect at a very small positive field near to zero.

The hysteresis curves at selected temperatures for the low field region are shown in **Figure 4.11**. The solid curves represent the descending field branch, and the dashed curves show the ascending field branch. One can see a tiny coercive field and a tiny remanent magnetization when the temperature is below 30 K which is well visible. In addition, a small hysteresis is discernible below 30 K.

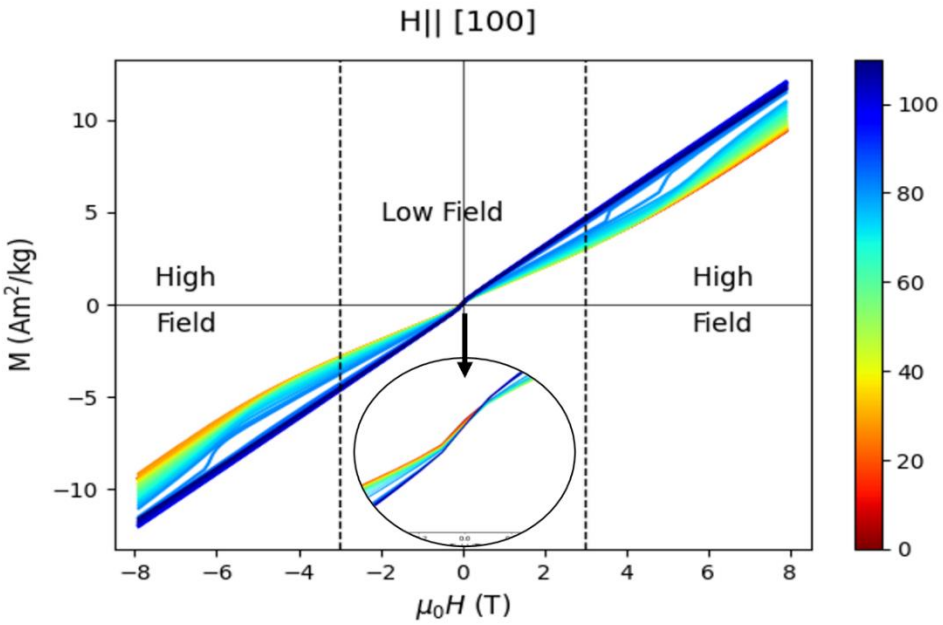

Figure 4.10: Isothermal measurements of Mn_4FeSi_3 in the temperature range of (8-110) K, taken from the descending branch of the hysteresis loop with H || [100]. The data has been re-binned with ΔT= 1 K and μ_0ΔH = 0.1 T.

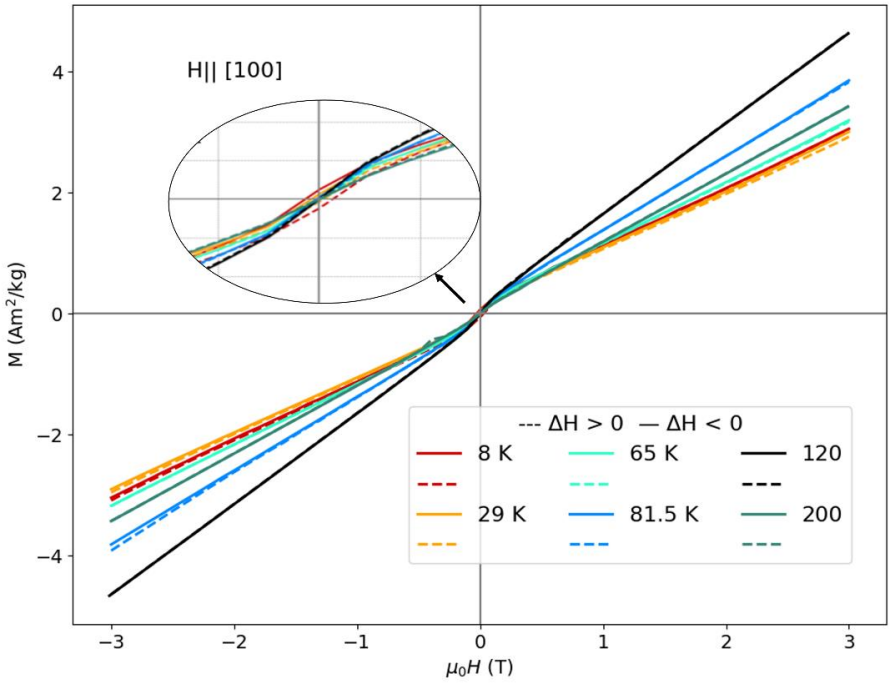

Figure 4.11 : Low field features for selected isotherms obtained by applying the field || [100] (8< T <350) K. The solid curves represent the descending field branch (ΔH < 0) and the dashed ones of the ascending field branch (ΔH > 0). Insert shows zoomed view very close to the origin. Data has been re-binned with ΔT= 1 K and μ_0ΔH = 0.1 T.

Although there is no remanence or coercivity above 30 K, still the slope in the field range (-0.2 < $\mu_0 \Delta H$ < 0.2) T is larger as compared to the slope at larger field values. As the inflection point around zero is still there till 110 K, the higher temperatures above 110 K to 350 K were checked with applied field along the axis parallel to [100]. The inflection point vanishes above 240 K.

For better resolving the anomalies observed below 120 K, the derivative $\frac{dM}{dB}$ was calculated from the ascending branch of the hysteresis loop (**Figure 4.12**). A low intensity peak at zero field occurs for all temperatures. Both the maximum intensity and the position of the peak seem to be temperature independent. Moreover, for temperatures larger than 83 K the slope $\frac{dM}{dB}$ on both sides of the peak is almost constant and does not fall to zero. For lower temperatures (< 80 K), the curvature in the derivative reflects the change of slope in the M (B) curves as a function of temperature. Between the two temperature ranges T < 80 K and T > 80 K, a prominent gap is visible in $\frac{dM}{dB}$ curves, reflecting the large difference between the M(B) slopes of these two temperature ranges.

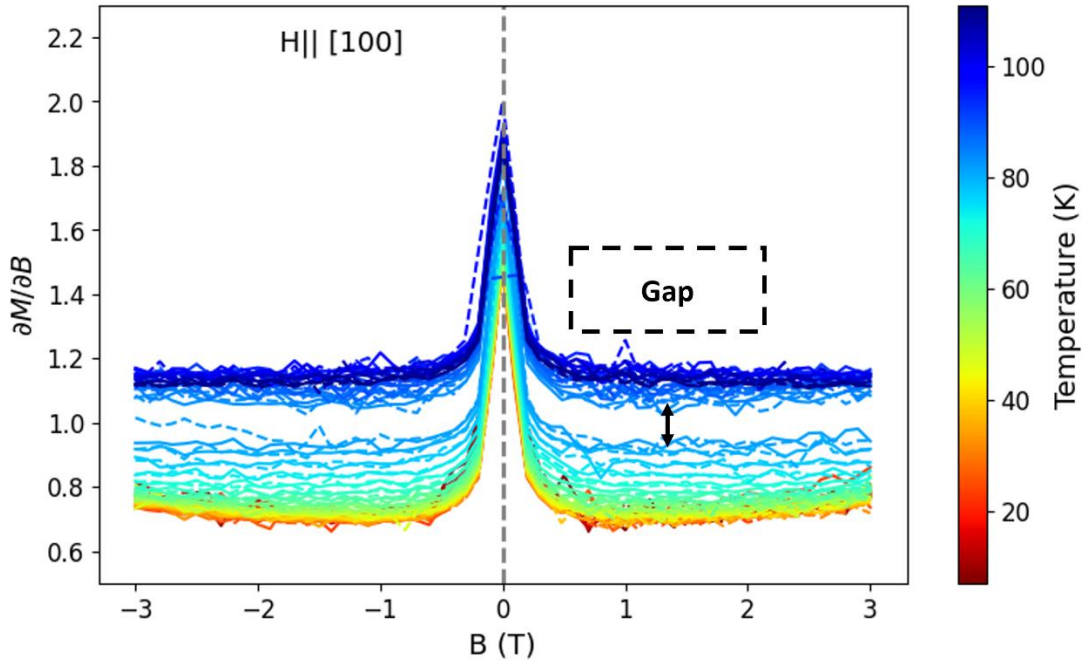

Figure 4.12: $\frac{dM}{dB}$ (×100) calculated from the isothermal measurements of Mn_4FeSi_3 for the temperature range 8-110 K with H || [100]. The data has been re-binned with ΔT= 1 K and ΔB = 0.1 T.

b) Temperature-dependent magnetization with H ||[100]

The temperature-dependent magnetization was obtained by isofield measurements while cooling the sample continuously from 350 K to 2 K at a sweep rate of 1K/min, under a fixed magnetic field || [100]. M/B (T) curves at selected low fields are shown in **Figure 4.13**. The left part shows the curves measured under isofield conditions, while in the right part shows the curves, which were extracted from the isothermal measurements (110-8) K, are shown. Since no significant discrepancies between the ascending and the descending branches, the curves of one of them are presented.

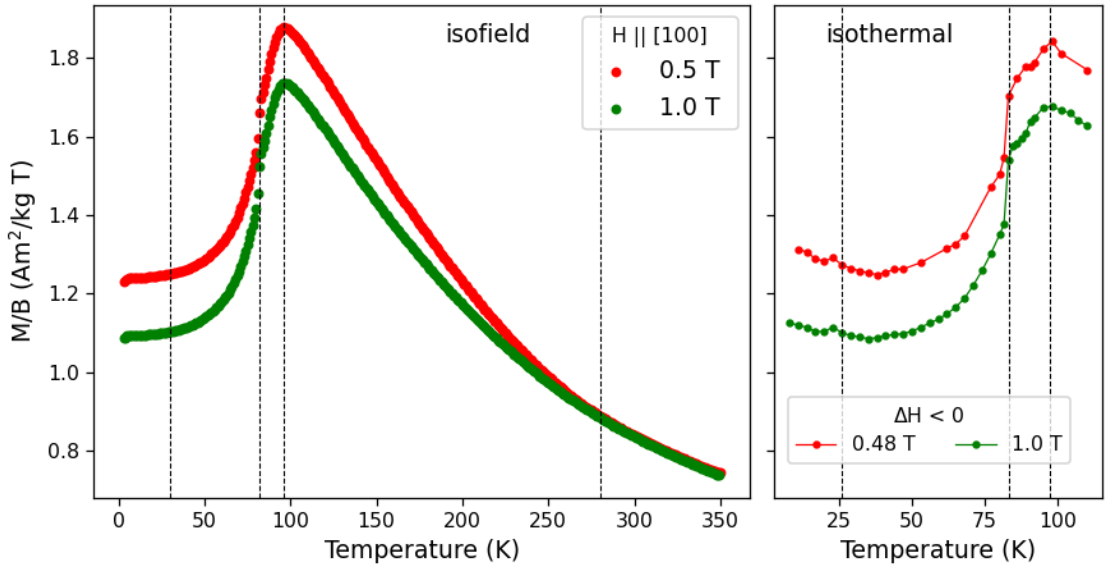

Figure 4.13: The M/B curves as a function of temperature. (Left) Curves from isofield measurements for fields of 0.5 T and 1 T applied along [001] (sample was cooled from 350 - 2) K. (Right) Curves extracted from the descending branch of the hysteresis loop at fields of 0.48[3] and 1 T, temperature range (110 – 8) K. The data has been re-binned with ΔT= 1 K and ΔB = 0.01 T for isothermal measurements and with ΔT= 1 K for the isofield measurement.

In the high temperature Curie-Weiss region (>280 K), the isofield curves for both applied fields are parallel (**Figure 4.13, left**). With further cooling, the magnetization increases and reaches a maximum at 95 ±1 K. Between 95-65 K the magnetization shows a sharp reduction; below this temperature the reduction rate decreases until the curves approximately approach a constant value below 40 K. The extracted curves from the isothermal measurements (**Figure 4.13, right**) show a

[3] A field of 0.48 T was chosen instead of 0.5 T, due to the noise noticed in the 0.5 T measurement. This is related to the change of the field sweeping mode, from a discontinuous mode of 1000 Oe step size above 0.5 T to a continuous mode between 0.5 T and -0.5 T. The overlap between the recorded data points at the boundary leads to noise in the magnetization curves.

similar behaviour. However, in difference to the isofield curves, the magnetization slightly increases below 40 K. A discontinuity in M/B(T) curves occurs around 79 K for the isofield curves, and between (78- 82) K for the isothermal curves.

4.2.2.3 Anisotropic behavior of the magnetization in the low field region

The magnetic properties of Mn_4FeSi_3 exhibit a clear anisotropy with different response depending on whether the field is applied in the *a*, *b*-plane or parallel to the *c-axis*. To show this behavior in the low field region, the isofield M(T) curves at $\mu_0 H = 1T$ with H || [001] and H || [100] are compared and shown in **Figure 4.14**.

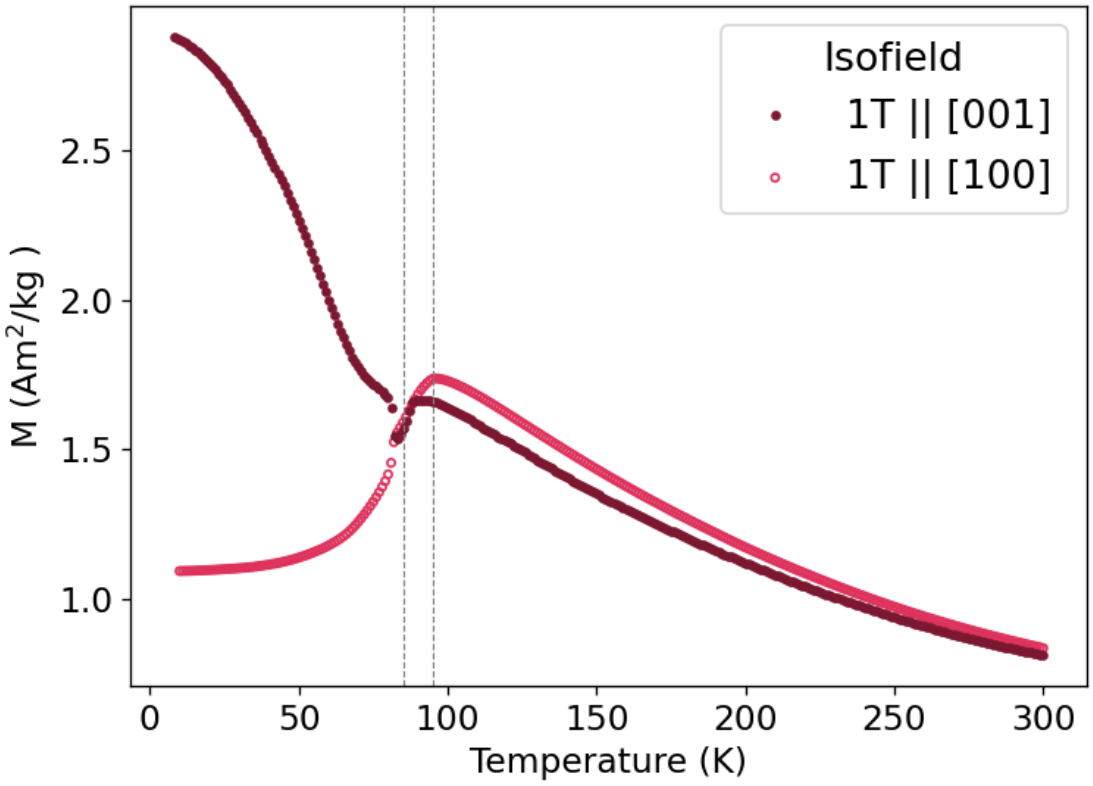

Figure 4.14: M (T) curves for isofield measurement with a field of 1 T. The closed-dark red circles: H || [001], the opened- light red circles: H || [100].

The curves' maxima indicative of the transition from the PM state are slightly different for the two field directions (92 ± 3 K with H || [001]; 95 ± 1 K with H || [100]). For the field || [001] a clear dip

in the magnetization is observed between 88 K and 80 K with a minimum around 82 K. At a similar temperature, a discontinuity sudden decrease in magnetization is observed with the field H ‖ [100]. The curves of the two directions of the field coincide at 82 K. With decreasing the temperature below the drop, the magnetization curve starts increasing again with field H || [001] with an additional change of trend at 65 ±5 K. In contrast to this with H || [100] the magnetization decreases monotonically below the transition temperature. Below 40 K the slope of M (T) curve decreases for both directions. The magnetization with H || [100] is slightly greater than the one with H || [001] in the high temperature range above 87 K. The offset at the PM region could be referred to the different instruments used for these measurements.

4.2.3 Magnetization Measurements with high fields (3-8) T

4.2.3.1 Magnetization Measurement with high field along [001]

a) Field-dependence of magnetization based on isothermal measurement with H || [001]

The magnetization loops for some selected temperatures below 70 K with the external field applied parallel to [001] are shown in **Figure 4.15**. As the field increases above 3 T, the isotherms converge till they intersect at ≈ 5.5 ±0.3 T, at higher fields they diverge again. One can conclude that the divergence of the M(B) curves reflects the variation of the magnetization response in the low temperature region, and the intersect means they have the same magnetization between 5 T and 6 T.

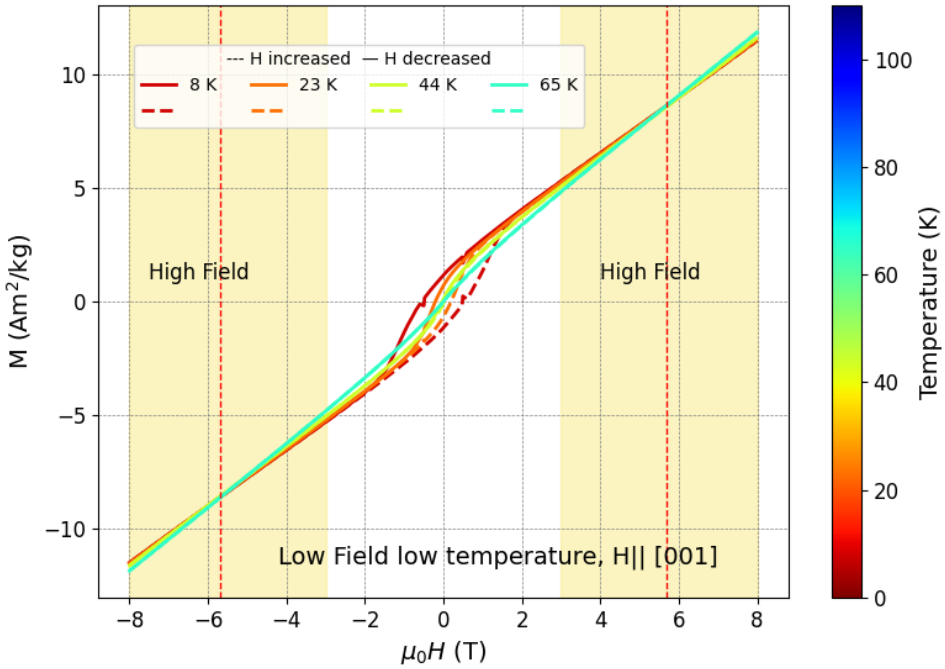

Figure 4.15: Isothermal magnetization data: full hysteresis loops with H || [001] for selected temperatures in the range of 8 K to 110 K. The solid lines are extracted from the descending field branch of the hysteresis loop (ΔH < 0), the dashed- lines are for the ascending field branch (ΔH > 0). The line colour indicates the temperature of the isothermal measurement. Data has been re-binned with ΔT= 1 K and μ_0ΔH = 0.1 T.

The derivative $\frac{dM}{dB}$ is constant for the high fields in the region between 80 K and 120 K (**Figure 4.16, bottom)**. Additional features at different field values and temperatures are observed from the descending branch (solid lines) (enlarged in **Figure 4.16, top**). The first feature corresponds to a temperature of 85 K is located at field values of 4.5 T and -6 T, the second corresponds to 86 K and is located at 3.5 T and -5 T. The third one corresponds to 87 K and is around 2 and -4 T. This means that there is a strong field dependence of these isotherms. Furthermore, the maxima of the differ, with the largest peak at 85 K for the positive fields, while for the negative fields the maximum is at 86 K. This observation is associated with the hysteresis indicated as a dashed line. The greater dashed peak intensity is for 86 K and the smaller one is for 85 K. The 87 K is missing which could be due to instrumental problem. Some other peaks might not occur due to the limitation of the applied field (up to 8 T), the feature might occur at stronger field (> 8T). **Figure 4.17** shows the openining and the closing of the hysteresis loops for these anomalies.

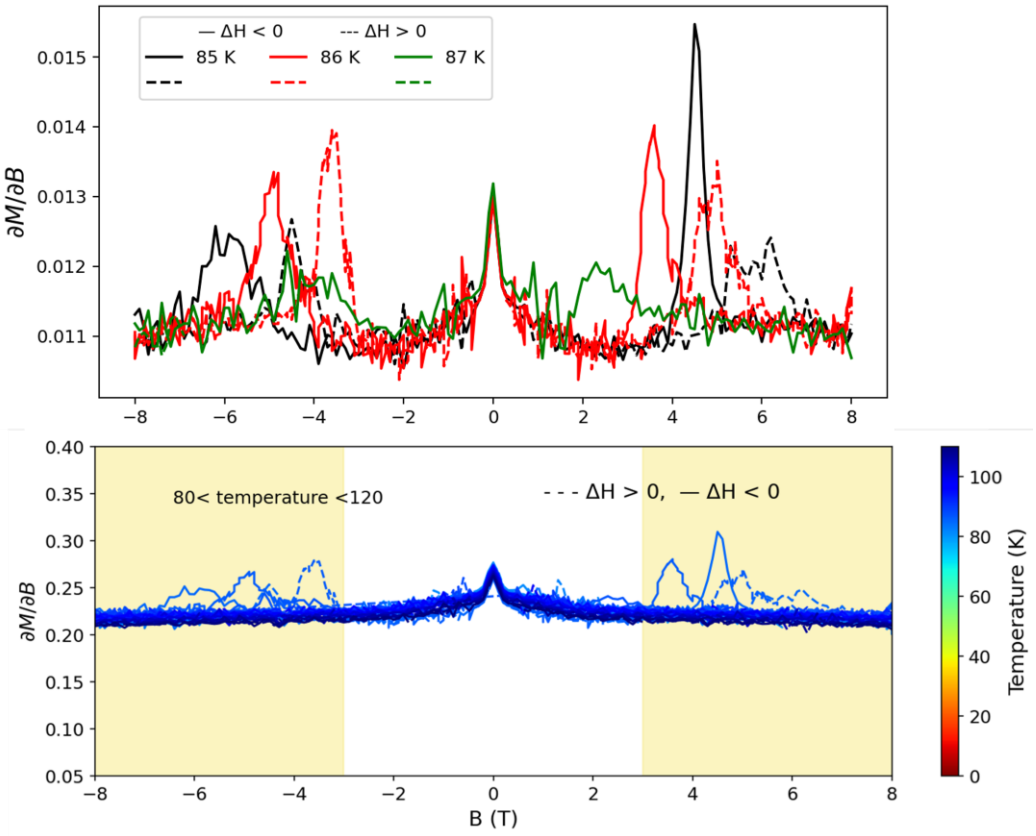

Figure 4.16: $\frac{dM}{dB}$ as a function of magnetic field calculated from the isothermal measurements of Mn_4FeSi_3 with H || [001]. (Bottom) The high field region between (±3 and ±8) T is highlighted in yellow for (80< T < 120) K; ($\frac{dM}{dB}$ × factor 20). (Top) enlarged for temperatures (85-87) K. Solid lines: descending field branch, and dashed lines: ascending field branch. Data has been re-binned with ΔT= 1 K and ΔB = 0.1 T.

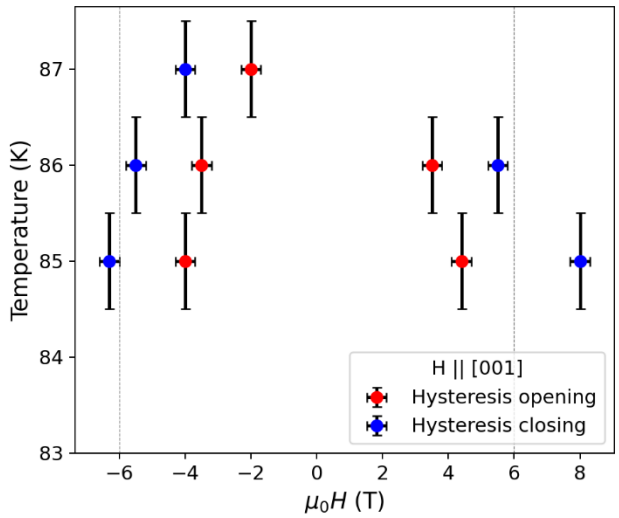

Figure 4.17: The temperature versus the field flux for the anomalies (85, 86, 87) K. Red circles: hysteresis opening and blue circles: hysteresis closing.

b) Temperature-dependent magnetization with H || [001]

The temperature-dependent magnetization for high fields with H parallel to the [001] direction is shown in **Figure 4.18**. On the left, the M(T) curves for the isofield measurement are shown (300 -2 K at 7.9 T). On the right, the curves extracted from the isothermal measurement for selected fields (data has been re-binned with temperature steps of 1 K and field steps of 0.01 T).

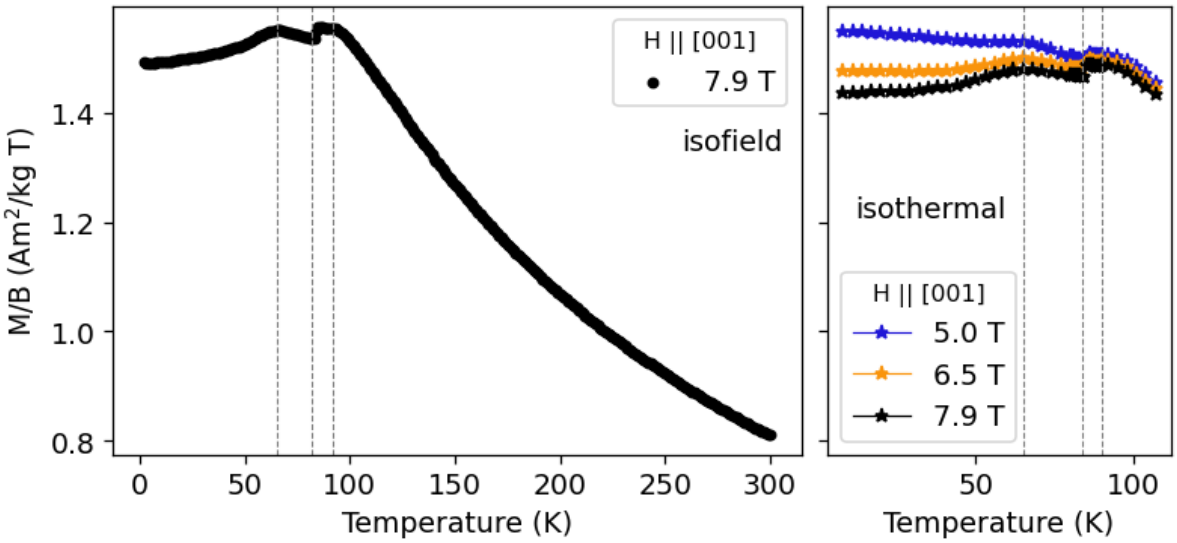

Figure 4.18: The M/B curves as a function of temperature. (Left) curves from isofield measurement at a field of 7.9 T applied || [001], sample was cooled from 300 K to 2 K. (Right) curves extracted from the descending branch of the hysteresis loop at fields of 5, 6, 7.9) T, temperature range (110-8) K. Data has been re-binned with ΔT=1K and ΔB = 0.01 T for isothermal measurement and with ΔT= 1 K for the isofield measurement.

At 7.9 T(**Figure 4.18, left**) the magnetization increases on cooling and reaches a maximum around 94 K and stays approximately constant till ~85 K. A sharp dip appears between 85- 82 K. At lower temperatures the curve increases again till 65±1 K a turning point is reached. Then, the magnetization decreases slowly until the curve approximately becomes constant below 30 K. From the isothermal M(T) curves (**Figure 4.18, right**) it is obvious that the first transition at the same temperature and does not change with field. In addition, the dip observed in the isofield measurements around 84 K is not affected strongly by varying the fields and the protocol. The second transition (~65±1 K) moves in temperature from 62 K at 5 T to 65 K at the higher field of 7.9 T. The peak around 65 K becomes stronger with increasing the applied field.

4.2.3.2 Magnetization Measurement with high field along [100]

a) Field-dependence of magnetization based on isothermal measurement with H || [100]

A comparison of the data with the field applied in the two different directions in a, b- plane [100] and [120] shows that the M(B) curves have in principle the same behavior **(chapter A.1).**

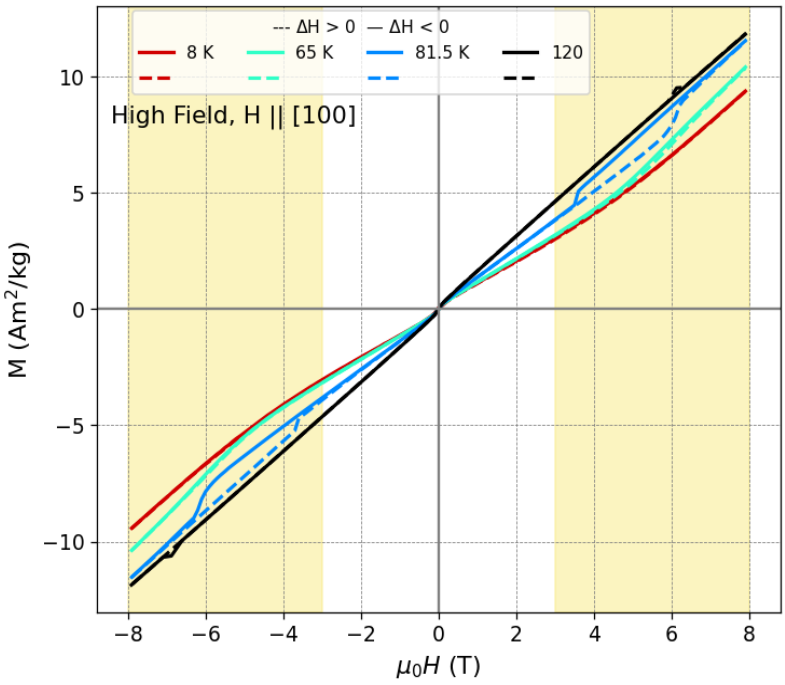

Figure 4.19: Selected isotherms obtained by applying the field || [100]. Solid lines from descending field branch (ΔH < 0), dashed lines from the ascending field branch (ΔH > 0). Data was re-binned with ΔT= 1 K and μ_0ΔH = 0.1 T.

For temperatures above 120 K (in the PM region), magnetization is linear for high fields. With decreasing temperature, the isotherms deviate from the linear behavior and the magnetization decreases. Below < 70 K an increase of the curvature is observed. The ascending and the descending branches of the curves match well except for temperatures between 79 K and 82 K where a small magnetic hysteresis is observed between 3.5 T and 7 T.

The derivative $\frac{dM}{dB}$ was calculated for the temperatures between 8 K and 110 K and is shown versus B with H || [100] in **Figure 4.20.** For the high field /high temperature regions (> 83 K) an almost constant slope is observed, for the lower temperatures (< 80 K), a clear curvature of the derivative is visible at high fields, which decreases with decreasing temperature. The opening of the hysteresis loops above manifests as pronounced anomalies in $\frac{dM}{dB}$ at (80-82) K (**Figure 4.20**). The peaks are

associated with branching of the M(B) curves. The lower peak moves from 4.8(1) T at 80 K to 3.5(1) T at 81.5 K ($\Delta H < 0$) . The peak, indicating the approach of the branches, moves from 8 T at 80 K to 6 T at 81.5 K. The peak positions are slightly different for reversed field direction at 81.5 K and not visible at 80 K. Finally, at 23 K a smaller peak is visible around -7 T, which again is not seen, if the field direction is reversed. **Figure 4.21** shows the openining and the closing of the hysteresis loops for these anomalies.

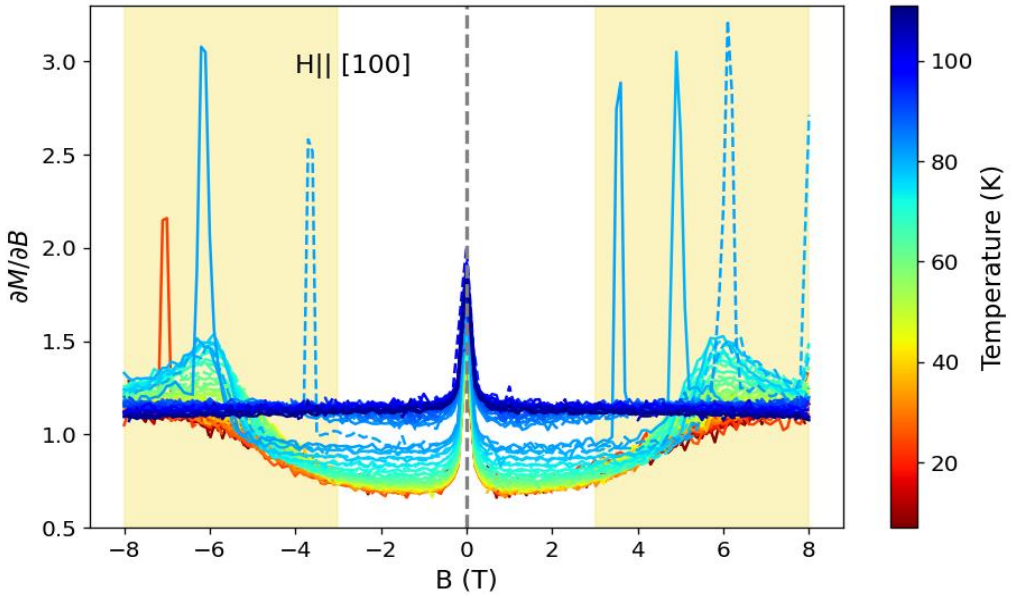

Figure 4.20: $\frac{dM}{dB}$ (×100) calculated from the hysteresis loops of Mn_4FeSi_3 at temperature range of (8-110) K with H || [100] and. The solid lines are for the descending branch and the dashed ones are for the ascending branch. Data has been re-binned with ΔT= 1 K and ΔB = 0.1 T.

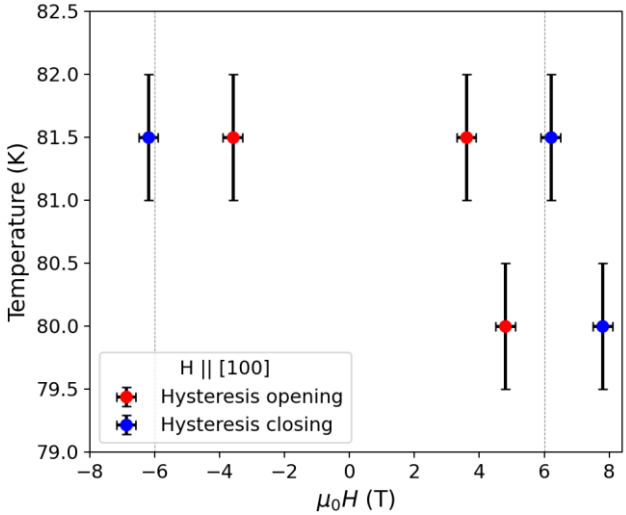

Figure 4.21: The temperature versus the field flux for the anomalies (80, 81.5) K. Red circles: hysteresis opening and blue circles: hysteresis closing.

b) Temperature-dependent magnetization with H || [100]

Temperature-dependent M/B (T) curves measured under isofield conditions in the temperature range of (350–2 K) with H || [100] are shown in **Figure 4.22,** left, on the right curves extracted from the isothermal measurements (ΔB > 0, 8 K< T< 110 K) are shown.

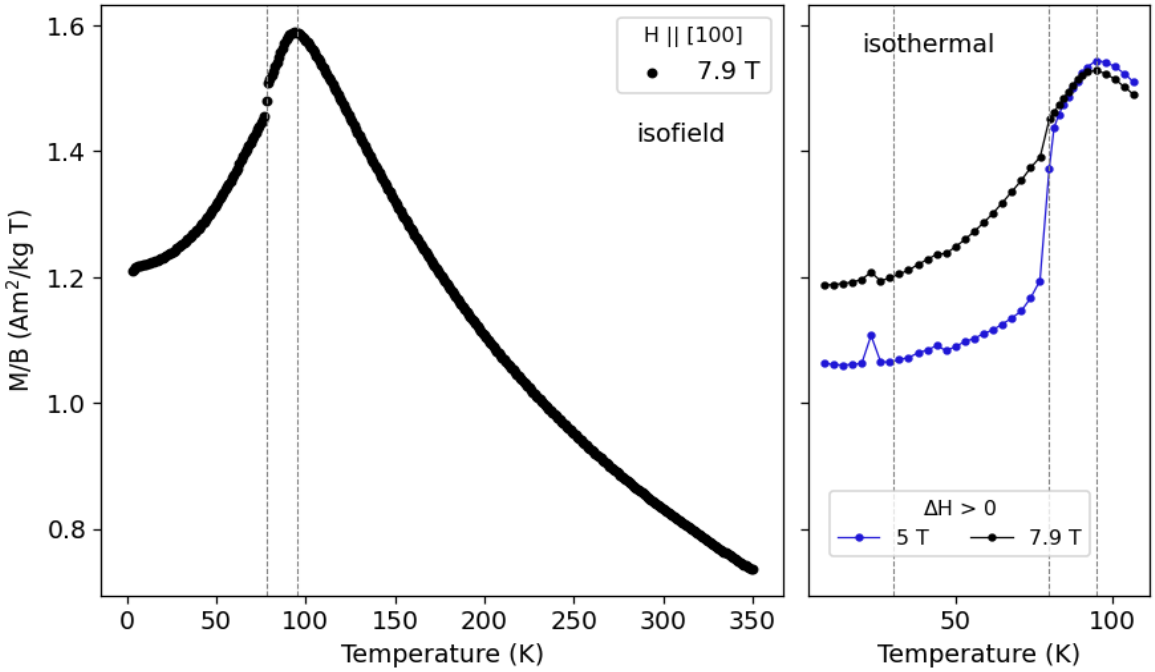

Figure 4.22: M/B curves as a function of temperature with H || [100]. (Left) curves from isofield measurement at 7.9 T (350- 2) K. (Right) curves extracted from the ascending branch of hysteresis loop at fields of 5 T and 7.9 T (110-8 K). Data has been re-binned with ΔT= 1 K and ΔB = 0.01 T for isothermal measurement, and with ΔT= 1 K for the isofield measurement.

With decreasing temperature, the magnetization increases and reaches its maximum at 95 ± 1 K. Below this temperature, it decreases gradually, but remains different from zero at 2 K. The sudden drop of the magnetization in the vicinity of 80 K looks related to the feature which is discussed previously in the isothermal measurements, similar to what was observed with H || [001].

The curves extracted from the isothermal measurements **(Figure 4.22, right**) at 7.9 T are similar. For fields between (5-7.9) the discontinuous change (drop) around (80 -82) K is more pronounced at the lower fields than for the higher fields, as this measurement is close to the peak position identified from the isofield curves. The reduction of the magnetization below 80 K is sharp at 5 T and becomes gradual at the higher field 7.9 T.

4.2.3.3 Anisotropic behavior of the magnetization in the high field region

The anisotropy of the magnetic response of Mn_4FeSi_3 is discussed in this section for relatively high fields of 7.9 T applied || [001] and || [100], and shown in **Figure 4.23**.

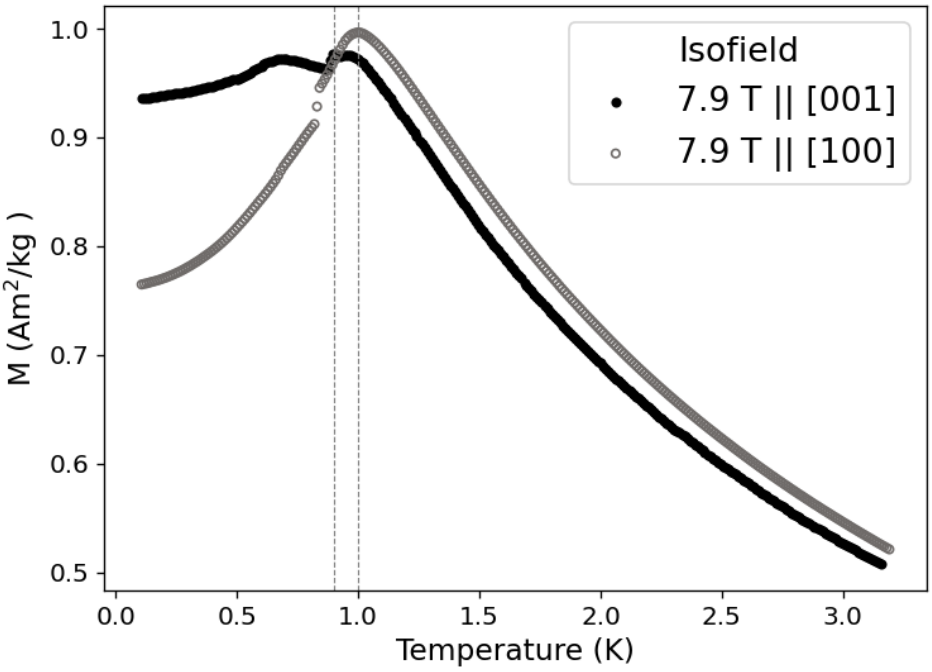

Figure 4.23: M (T) curves of isofield measurement with a field of 7.9 T; black circles (H || [001]) and grey- opened circles (H || [100]).

The transition temperature from the PM to AFM happens around 95 K. It occurs as a broad maximum with H || [001], while it is visible as a global peak with H || [100]. The discontinuous drop in magnetization occurs at slightly different temperatures depending on the field direction: for H || [001] it is located around 84(1) K, while for H || [100] it is around 81(1) K.

There is a small offset of the magnetization in PM region depending on whether the field is || [001] or || [100]. This offset could be due to the different instruments used for these measurements. With H || [001], the magnetization increases again below 80 K, reaches its maximum at (65± 1) K, and then decreases again. This could be interpreted as a transition between two different magnetically ordered phases at 65 K. In contrast to this, when H || [100] the magnetization decreases gradually the whole temperature range from 95 K down to the lowest measured temperature, very similar to the behavior at lower field with a small difference, where a small bump in the vicinity of 65 K appears with the high fields.

Table 4.2 sumarizes and shows the main observations obtained from the isothermal and isofield magnetization measurements for the two different directions. Since the [100] and [120] directions display no significant difference, the [100] is just presented.

No.	Direction / Observation	[001]	[100]	Field dependence	
				Strength	Direction
(1)	**High temperature transition (PM- AF_{HT})**	92 (3) K	95 K	-	-
(2)	**Drop in M**	84 (1) K	81 (1) K	yes	yes
(3)	**Low temperature transition**	65 K	-	yes	yes
(4)	**Low temperature low field phase ($LTLF$)**	T< 65 K B < 5 T	Change in $\partial M/\partial B$ B< 5 T	yes	yes
(5)	**Low temperature high field phase ($LTHF$)**	T < 65 K B > 5.5 T	Change in $\partial M/\partial B$ B> 5.5 T	yes	yes
(6)	**Remanence**	T < 60 K B < 0.6 T	T < 30 K B< 0.2 T	yes	yes
(7)	**Coercivity**	T < 60 K B < 0.6 T	T < 30 K B < 0.2 T	yes	yes
(8)	**Experimental μ_{eff}**	4.3(1) μ_B	4.24(5) μ_B	yes	yes

Table 4.2: Synopsis of the main observations obtained from the magnetization measurements for Mn_4 Fe Si_3 single crystal. The observations are presented with H || [001] and H || [100].

Chapter 5 Discussion and Conclusions

The results of the magnetization data were obtained using two different protocols, under isothermal and isofield conditions. The observations show protocol independent macroscopic features implying that the system is always at thermodynamic equilibrium in contrast to the behavior that our group found in the x =2 member of the $Mn_{5-x}Fe_xSi_3$ family. Taken together, the findings highlight the anisotropic behavior as well as the field-temperature dependent magnetic response of Mn_4FeSi_3.

The paramagnetic susceptibility of the Mn_4FeSi_3 displays isotropic behavior above 280 K, and anisotropic response below 280 K, **Figure 5.1**. If the field is applied || [100] a deviation from Curie-Weiss behaviour is observed below 280 K. This deviation is field strength independent. For H || [001], a field-dependent deviation from *1/T* is observed in a wide temperature region above the ordering temperature. A reasonable adherence to Curie- Weiss behaviour is visible for T > 280 K, when small fields are applied. For large fields, χ^{-1} is linear with T down to the ordering temperature. So we can state, that this field strength is sufficient to suppress the correlations, which lead to the enhanced magnetization in the case of small applied fields.

The paramagnetic moment μ_{eff} determined from the Curie-Weiss analysis is in good agreement with published data (Herlitschke et al., 2016; Johnson et al., 1972). The Curie-Weiss temperatures determined from this analysis differ slightly for the different field directions. We find a lower value if the field is applied || [100].

In contrast to (Candini et al., 2004; Songlin et al., 2002) studies on polycrystalline samples, which show a featureless response of this material, our magnetization measurements on a single crystal produce a variety of features in dependence of field direction. They are summarized in the field-temperature diagram, **Figure 5.2, (a)** with H || [001] and **(b)** with H || [100].

A maximum in the temperature dependence of the magnetization for a field || [100] at 95 K indicates the transition to an ordered state, as shown in **Figure 5.1, bottom**. For the field || [001] (**Figure 5.1, top**) the magnetization flattens at approximately the same temperature upon cooling. This point is close to the high temperature transition (T_{HT}) reported in the literature, which is supposed to be a transition from PM to AF (Songlin et al., 2002). The high temperature antiferromagnetic phase is named in this discussion as (*HTAF*).

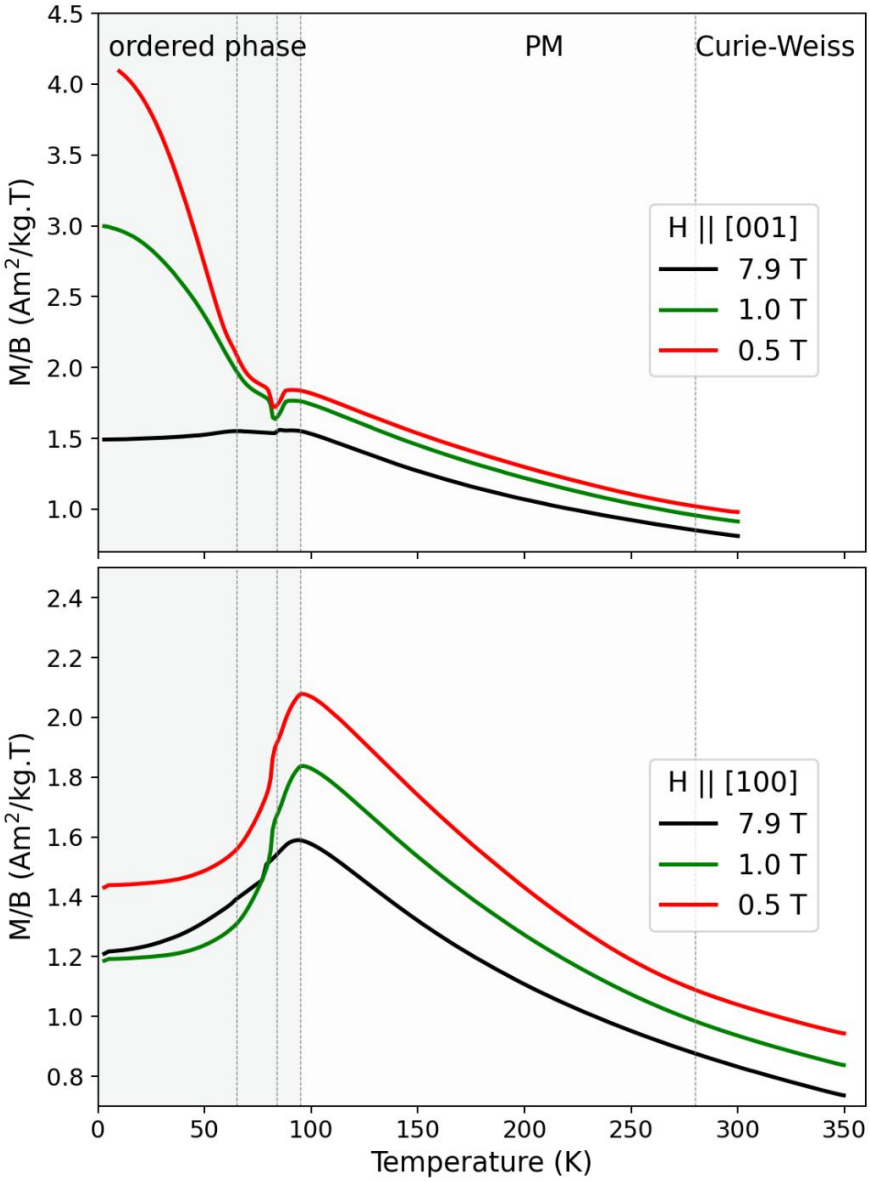

Figure 5.1: M/B (T) obtained from isofield magnetization data set for Mn_4FeSi_3 with fields of (0.5, 1.0, 7.9) T parallel to: (Sürgers et al.) [001] and (bottom) [100]. The curves are shifted up with 0.1 step for clarity.

The sudden drop in the temperature dependence of the magnetization at 84±1 K and 81 ±1 for fields || [001] and || [100], respectively, is manifest as distinct peaks in in the field derivative of the magnetization with hysteretic behavior. With the formation of this peak the slope of the magnetization is reduced in the field range $\mu_0 H < 5$ T. It looks, as if the sharp feature in the field derivative moves out of the observed field window for T < 80 K. This remains to be observed by

higher fields e.g., with pulses fields. It should be noted, that a high field study on powder samples did however show no special features and hence single crystal studies are necessary.

In the low temperature region (< 65 K) and low field region $\mu_0 H < 0.7$ T, the observed coercivity and remanence indicate ferromagnetic correlations of the *c*-component of the magnetic moment.

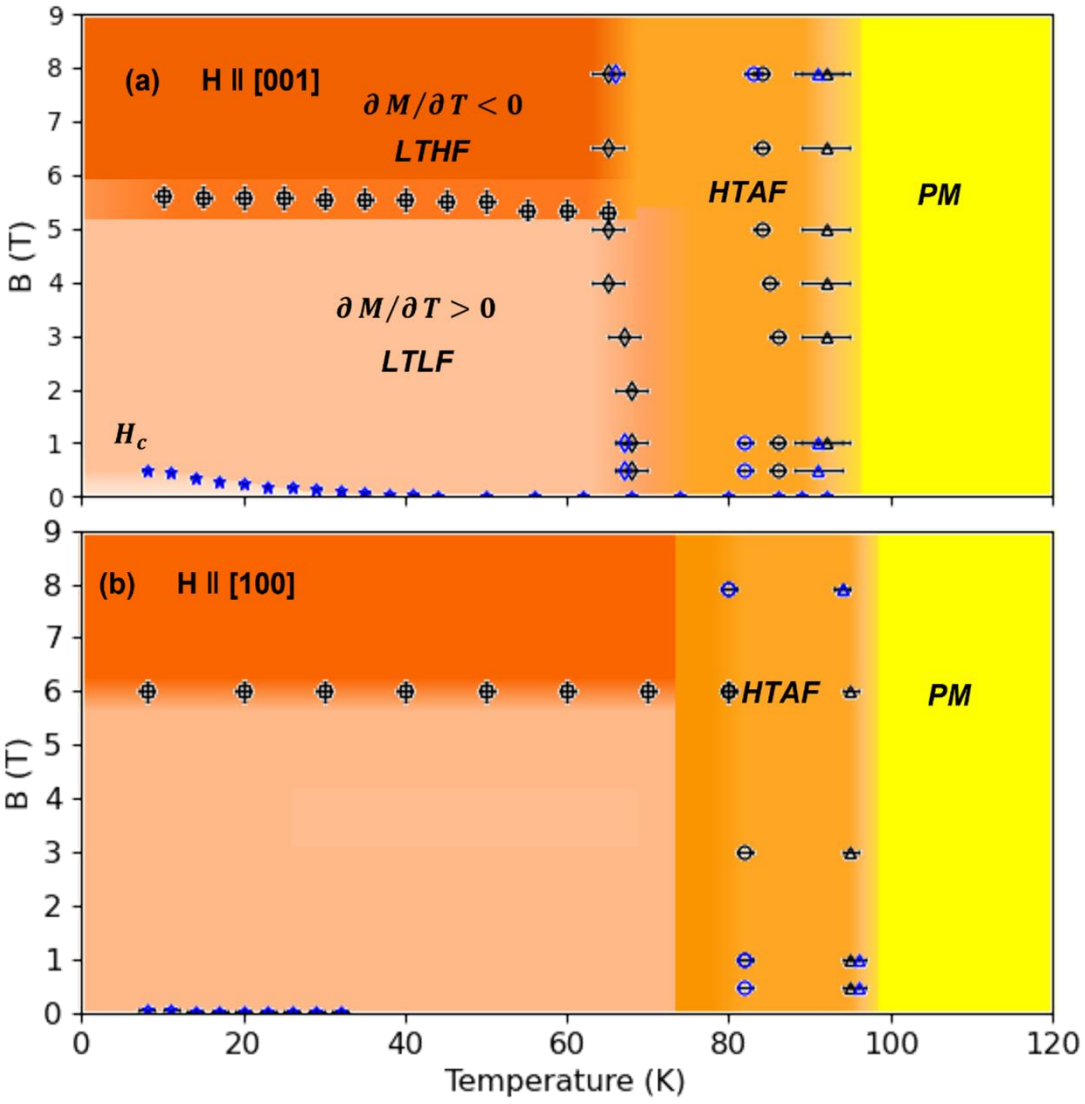

Figure 5.2: Field-temperature diagram of Mn_4FeSi_3. (Black points) obtained from isothermal measurement data set, descending branch and (blue points) obtained from isofield measurement data set. (Δ) T_{HT} (○) the drop in M (◊) T_{LT} (□) field-induced transition (x) coercivity.

Within the temperature dependent measurements of the magnetization this is also seen by the increase of the magnetization upon cooling below 65 K for $\mu_0 H < 5$ T (**Figure 5.2, a)**. The low temperature low field response is named as ($LTLF$). At 5.2(3) T the magnetization response is approximately constant with the temperature change. By increasing the applied field > 5.5 T, a local maximum, enhanced by field, is detected in the vicinity of 65 K, and the curve gradually decreases down to the lowest temperatures. This observation points to the reported transition between two AF phases (T_{LT}) (Candini et al., 2004)**.** The low temperature high field response is named as ($LTHF$). We associate the field induced change of the temperature gradient at 5.2 ±0.3 T to a further magnetic phase of Mn_4FeSi_3.

As the maximum point (T_{HT}) is detected around 95 K along the whole measured field range and directions ([001], [100], and [120]), it seems to be field independent. However, the low temperature transition T_{LT} exclusively occurs around 65 K if the field is applied || [001].

The present magnetization data is compared to the results obtained from different magnetization measurements on single crystals for the neighboring compounds (x = 0 and 2) (Ait Haddouch et al., 2022). The three compositions exhibit anisotropic behavior, as illustrated in **Table 5.1**. In accordance with (Songlin et al., 2002) and (Candini et al., 2004) the PM to AFM transition at T_{HT} for Mn_4FeSi_3 (x =1) is observed roughly at 95 below this for both x = 0, 2. The low Fe concentration in the composition under study is presumably responsible for the slight reduction of the ordering temperature. Based on the increase of T_N found for x=2 this result is surprising. For x =0 and x =2 the spins order first in a collinear way upon cooling. As a consequence, one observes a magnetic response only, when the field is applied in the *a,b*- plane. This is different for the x =1 case, where the susceptibility reacts for all field directions at ~ 95 K. However, it requires a microscopic probe, such as neutron diffraction to decide, whether the magnetic structure is collinear.

From the magnetization data of (Songlin et al., 2002), no field- induced magnetic-phase transitions are observed for x= 1 and 2 up to 38 T in powder samples. In contrast, the present magnetization results from single crystal specimen hint to a temperature independent field-induced transition for $x = 1$ at low temperatures for a field between 5 and 6 T. It manifests differently for the [100] direction and for the [001] direction. In the former case the transition is assigned to the peak in dM/dB in the temperature range 50 K < T < 80 K and to the inflection point for T < 50 K, in the latter case it is related to the field for which the magnetization becomes non-monotonic. Because of the nearly temperature independent susceptibility we speculate, that the AF oriented moments are perpendicular to the [001] direction. This requires a detailed diffraction study to confirm.

A recent study reported a field-induced transition for x= 2, depending on temperature if H ⊥[001], but temperature independent if H || [001]. A temperature dependent field-induced transition is observed at low temperatures only if H || [001] for $x = 0$ (Ait Haddouch et al., 2022). So, the two compounds containing Fe both show transitions for the field applied in [100] (and in [120]) direction as well as for the field applied in [001] direction. In contrast, the parent compound has the field induced transition only for the field || [001], indicating that the transition with field applied along [100] which is observed in x=1,2 is related to the presence of Fe in the system.

x	**Field direction**	**High temperature transition (T_{HT})**	**Low temperature transition (T_{LT})**	**Field induced transition**
0	**|| [001]**	-	66	Temperature dependent < 60 K
	⊥ [001]	99	66	-
1	**|| [001]**	92	65	Temperature independent ~ (5-6) T and < 65 K
	⊥ [001]	95	-	Temperature independent ~ (5- 6) T and < 70 K
2	**|| [001]**	120	69	Temperature independent ~ 4 T and < 70 K
	⊥ [001]	120	69	Temperature dependent < 70 K

Table 5.1: A comparison between the magnetic transitions between $Mn_{5-x}Fe_xSi_3$, x = 0, 1 and 2 from direction dependent magnetization measurements on single crystals. Data for x = 0, 2 is obtained from (Ait Haddouch et al., 2022). Note that the T_{HT} and T_{LT} are named in the literature on the other compositions as T_{N2} and T_{N1}, respectively.

Chapter 6 Outlook

The macroscopic behavior of Mn_4FeSi_3, is clearly more complicated as the published powder data would imply. To resolve the underlying magnetic structure, detailed neutron diffraction investigations are required. Similar to Mn_5Si_3 the field induced phases have not been resolved, because the experiments in strong applied fields can access often only a small number of unique magnetic reflection. It would be interesting to study the different magnetic phases (T > 95 T, 65< T < 95 and T < 65) K with ($\mu_0 H < 5T$) and ($\mu_0 H > 5T$). This could provide more about the magnetic structure of this compound. Moreover, measuring all components of the ordered moments, not only that which align with the applied field provide more insights about the magnetic correlations in this system.

Oriented single crystal samples of $Mn_2Fe_3Si_3$ (x =3) were prepared and synthesis procedure is described with this work. Different studies and measurements can be implemented on this compound as an integrated work of studying the series. This compound is located between two groups within the system (Mn rich AFMs x < 3) with dominant AF interactions and (Fe rich FMs x >3) with stronger FM interactions. A systematic investigation of this compound by field direction dependent magnetization measurement, following the same procedures and protocols, allows the comparison between different compositions throughout $Mn_{5-x}Fe_xSi_3$ system. For this compound it is expected that the FM interactions are enhanced and possibly the AF order is already suppressed as for the x =4 case, which shows the largest MCE across the series. Yet it is unclear, whether the competition between AF and FM interactions plays a role for the different ordering on the *M1* site and on the *M2* site, which is assumed to be relevant for the MCE. So, it looks straight forward to investigate also the single crystal response, for which also new observations are expected as the literature contains only information about powder materials.

References

Ait Haddouch, M., Abboushi, N., Sharma, N., Eich, A., Grzechnik, A., Li, C., . . . Friese, K. (2022). Site dependence of the magnetocaloric effect in Mn5-xFexSi3. *Journal of Applied Crystallography, 55*(5), 1164-1172. doi:doi:10.1107/S1600576722007440

Al-Kanani, H., & Booth, J. J. J. o. a. p. (1997). Magnetic phase transitions in Mn5− x T x Si3 alloys. *81*(8), 4152-4153.

Bilderback, D. (1979). A real-time back-reflection Laue camera. *Journal of Applied Crystallography, 12*(1), 95-98.

Bińczycka, H., Dimitrijević, Ž., Gajić, B., & Szytula, A. (1973). Atomic and magnetic structure of Mn5–xFexSi3. *Physica status solidi (a), 19*(1), K13-K17.

Biniskos, N., Raymond, S., Schmalzl, K., Schneidewind, A., Voigt, J., Georgii, R., . . . Brückel, T. (2017). Spin dynamics of the magnetocaloric compound MnFe 4 Si 3. *Physical Review B, 96*(10), 104407.

Blundell, S. J. C. M. P. (2001). Magnetism in condensed matter: oxford master series. *29*.

Burgei, W., Pechan, M. J., & Jaeger, H. (2003). A simple vibrating sample magnetometer for use in a materials physics course. *American Journal of Physics, 71*(8), 825-828.

Buschow, K. H. J., & Boer, F. R. (2003). *Physics of magnetism and magnetic materials* (Vol. 7): Springer.

Candini, A., Moze, O., Kockelmann, W., Cadogan, J. M., Brück, E., & Tegus, O. (2004). Revised magnetic phase diagram for FexMn5−xSi3 intermetallics. *Journal of Applied Physics, 95*(11), 6819-6821. doi:10.1063/1.1688219

Coey, J. M. (2010). *Magnetism and magnetic materials*: Cambridge university press.

Das, B., Balasubramanian, B., Manchanda, P., Mukherjee, P., Skomski, R., Hadjipanayis, G. C., & Sellmyer, D. J. (2016). Mn5Si3 Nanoparticles: Synthesis and Size-Induced Ferromagnetism. *Nano Letters, 16*(2), 1132-1137. doi:10.1021/acs.nanolett.5b04360

Das, S. C., Mondal, K., Khamaru, N., Pramanick, S., & Chatterjee, S. (2020). Mn-site doping and its effect on inverted hysteresis and thermomagnetic irreversibility behavior of antiferromagnetic Mn5Si3 alloy. *Journal of Physics: Condensed Matter, 32*(48), 485802. doi:10.1088/1361-648X/aba983

Day, A. K. C. P. (1987). *Solid- State Chemistry Techniques*. united states: Clarendon Press Oxford

De Oliveira, N., & von RANKE, P. J. (2010). Theoretical aspects of the magnetocaloric effect. *Physics Reports, 489*(4-5), 89-159.

Derby, J., Atherton, L., & Gresho, P. (1989). An integrated process model for the growth of oxide crystals by the Czochralski method. *Journal of crystal growth, 97*(3-4), 792-826.

Design, Q. (2011). Vibrating Sample Magnetometer (VSM) Option User's Manual. *no, 1096*, 122.

Eich, A., Grzechnik, A., Caron, L., Cheng, Y., Wilden, J., Deng, H., . . . Friese, K. (2019). Magnetocaloric Mn5Si3 and MnFe4Si3 at variable pressure and temperature. *Materials Research Express, 6*(9), 096118. doi:10.1088/2053-1591/ab33b3

Foner, S. (1959). Versatile and sensitive vibrating-sample magnetometer. *Review of Scientific Instruments, 30*(7), 548-557.

Franco, V., Blázquez, J., Ipus, J., Law, J., Moreno-Ramírez, L., & Conde, A. (2018). Magnetocaloric effect: From materials research to refrigeration devices. *Progress in Materials Science, 93*, 112-232.

Galazka, Z. (2020). Czochralski method. In *Gallium Oxide* (pp. 15-36): Springer.

Gencer, H., Kolat, V. S., Izgi, T., Bayri, N., & Atalay, S. (2020). *Magnetocaloric Effect in Perovskite Manganites*.

Gottschilch, M., Gourdon, O., Persson, J., de la Cruz, C., Petricek, V., & Brueckel, T. (2012). Study of the antiferromagnetism of Mn 5 Si 3: an inverse magnetocaloric effect material. *Journal of materials chemistry, 22*(30), 15275-15284.

Gourdon, O., Gottschlich, M., Persson, J., Cruz, C. d. l., Petricek, V., McGuire, M. A., & Brückel, T. (2014). Toward a better understanding of the magnetocaloric effect: An experimental and theoretical study of MnFe4Si3. *Journal of Solid State Chemistry, 216*, 56-64. doi:https://doi.org/10.1016/j.jssc.2014.05.001

Govindhan Dhanaraj, K. B., Vishwanath Prasad, Michael Dudley (Ed.) (2010). *Springer Handbook of Crystal Growth*.

Gschneidner Jr, K., & Pecharsky, V. (1999). Magnetic refrigeration materials. *Journal of applied physics, 85*(8), 5365-5368.

Hahn, T., Shmueli, U., & Arthur, J. W. (1983). *International tables for crystallography* (Vol. 1): Reidel Dordrecht.

Hering, P., Friese, K., Voigt, J., Persson, J., Aliouane, N., Grzechnik, A., . . . Brückel, T. (2015). Structure, Magnetism, and the Magnetocaloric Effect of MnFe4Si3 Single Crystals and Powder Samples. *Chemistry of Materials, 27*(20), 7128-7136. doi:10.1021/acs.chemmater.5b03123

Herlitschke, M., Klobes, B., Sergueev, I., Hering, P., Persson, J., & Hermann, R. P. (2016). Elasticity and magnetocaloric effect in MnFe 4 Si 3. *Physical Review B, 93*(9), 094304.

Hurd, C. J. C. P. (1982). Varieties of magnetic order in solids. *23*(5), 469-493.

JCrystal (Producer). (2018). WinLaue (Laue simulation software). Retrieved from http://jcrystal.com/products/winlaue/index.htm

Johnson, V., Weiher, J., Frederick, C., & Rogers, D. (1972). Magnetic and Mössbauer effect studies of Mn5Si3: Fe5Si3 solid solutions. *Journal of Solid State Chemistry*, *4*(2), 311-323.

Karen Friese, p. c. (2023). [personal communication].

Kittel, C., & McEuen, P. (2018). *Introduction to solid state physics*: John Wiley & Sons.

Lander, G., Brown, P., & Forsyth, J. (1967). The antiferromagnetic structure of Mn5Si3. *Proceedings of the Physical Society, 91*(2), 332.

Luccas, R. F., Sánchez-Santolino, G., Correa-Orellana, A., Mompean, F. J., García-Hernández, M., & Suderow, H. (2019). Magnetic phase diagram, magnetotransport and inverse magnetocaloric effect in the noncollinear antiferromagnet Mn5Si3. *Journal of Magnetism and Magnetic Materials, 489*, 165451.

Lundgren, L., Tarmohamed, G., Beckman, O., Carlsson, B., & Rundqvist, S. (2007). First Order Magnetic Phase Transition in Fe2P. *Physica Scripta, 17*, 39. doi:10.1088/0031-8949/17/1/008

Maraytta, N., Skourski, Y., Voigt, J., Friese, K., Herrmann, M. G., Perßon, J., . . . Brückel, T. (2019). Direct measurements of the magneto-caloric effect of MnFe4Si3 in pulsed magnetic fields. *Journal of Alloys and Compounds*, *805*, 1161-1167. doi:https://doi.org/10.1016/j.jallcom.2019.07.113

Maraytta, N., Voigt, J., Salazar Mejía, C., Friese, K., Skourski, Y., Perßon, J., . . . Brückel, T. (2020). Anisotropy of the magnetocaloric effect: Example of Mn5Ge3. *Journal of Applied Physics, 128*(10), 103903.

Moffat, K. (1997). [22] Laue diffraction. In *Methods in enzymology* (Vol. 277, pp. 433-447): Elsevier.

Mugiraneza, S., & Hallas, A. M. J. C. P. (2022). Tutorial: a beginner's guide to interpreting magnetic susceptibility data with the Curie-Weiss law. *5*(1), 95.

Mühlbauer, A. (2006). *Innovative induction melting technologies: A historical review.* Paper presented at the International Scientific Colloquium, Modelling for Material Processing.

Multiwire Laboratories, L. (2013). MWL120 Real-Time Back-Reflection Laue Camera System. In. USA: Multiwire Laboratories, Ltd. .

Muthuramalingam, T., Mohan, B. J. M., & processes, m. (2013). Influence of tool electrode properties on machinability in spark erosion machining. *28*(8), 939-943.

Narasimhan, K., Reiff, W., Steinfink, H., & Collins, R. (1970). Magnetism and bonding in a D88 structure; Mössbauer and magnetic investigation of the system Mn5Si3-Fe5Si3. *Journal of Physics and Chemistry of Solids, 31*(7), 1511-1524.

Orendáč, M., Gabáni, S., Gažo, E., Pristáš, G., Shitsevalova, N., Siemensmeyer, K., & Flachbart, K. (2018). Rotating magnetocaloric effect and unusual magnetic features in metallic strongly anisotropic geometrically frustrated TmB4. *Scientific Reports, 8*(1), 10933. doi:10.1038/s41598-018-29399-2

Pericleous, K., Bojarevics, V., Djambazov, G., Harding, R., & Wickins, M. J. A. m. m. (2006). Experimental and numerical study of the cold crucible melting process. *30*(11), 1262-1280.

Reif, F. (2009). *Fundamentals of statistical and thermal physics*: Waveland Press.

Schmid, I. (2008). *The role of uncompensated spins in exchange biased systems.* University_of_Basel,

Schwartz, L. H., & Cohen, J. B. (2013). *Diffraction from materials*: Springer Science & Business Media.

Singh, S. J., & Sturza, M. I. J. C. (2022). Bulk and single crystal growth progress of iron-based superconductors (FBS): 1111 and 1144. *12*(1), 20.

Singh, V., Bag, P., Rawat, R., & Nath, R. (2020). Critical behavior and magnetocaloric effect across the magnetic transition in Mn1+xFe4−xSi3. *Scientific Reports, 10*(1), 6981. doi:10.1038/s41598-020-63223-0

Songlin, Dagula, Tegus, O., Brück, E., Klaasse, J. C. P., Boer, F. R., & Buschow, K. H. J. (2002). Magnetic phase transition and magnetocaloric effect in Mn5−xFexSi3. *Journal of Alloys and Compounds, 334*, 249–252. doi:10.1016/S0925-8388(01)01776-5

Sürgers, C., Wolf, T., Adelmann, P., Kittler, W., Fischer, G., & Löhneysen, H. v. (2017). Switching of a large anomalous Hall effect between metamagnetic phases of a non-collinear antiferromagnet. *Scientific Reports, 7*(1), 42982. doi:10.1038/srep42982

Tegus, O., Brück, E., Buschow, K. H. J., & de Boer, F. R. (2002). Transition-metal-based magnetic refrigerants for room-temperature applications. *Nature, 415*(6868), 150-152. doi:10.1038/415150a

Tegus, O., Brück, E., Zhang, L., Buschow, K., & De Boer, F. (2002). Magnetic-phase transitions and magnetocaloric effects. *Physica B: Condensed Matter, 319*(1-4), 174-192.

Vinokurova, L., Ivanov, V., & Kulatov, E. (1995). Magnetic phase transitions in single crystals of Mn5Si3 and (Mn, Fe) 5Si3. *Physica B: Condensed Matter, 211*(1-4), 96-98.

Windsheimer, H., Waitz, R., & Wubben, P. (2015). Inductive melting in cold wall crucible: technology and applications. *Induction technology, Reports*, 1-5.

Windsheimer, H., Waitz, R., & Wubben, P. J. I. t., Reports. (2015). Inductive melting in cold wall crucible: technology and applications. 1-5.

Zarkevich, N. A., & Zverev, V. I. (2020). Viable materials with a giant magnetocaloric effect. *Crystals, 10*(9), 815.

Appendix A

A.1 Comparison between the magnetization measurements with H || [100] and [120]

The data obtained by the isothermal measurements with H || [100] and H|| [120] coincide fairly. Note that the temperature step between (80-90) K is 1.5 K with H || [100] and 1 K with H || [120].

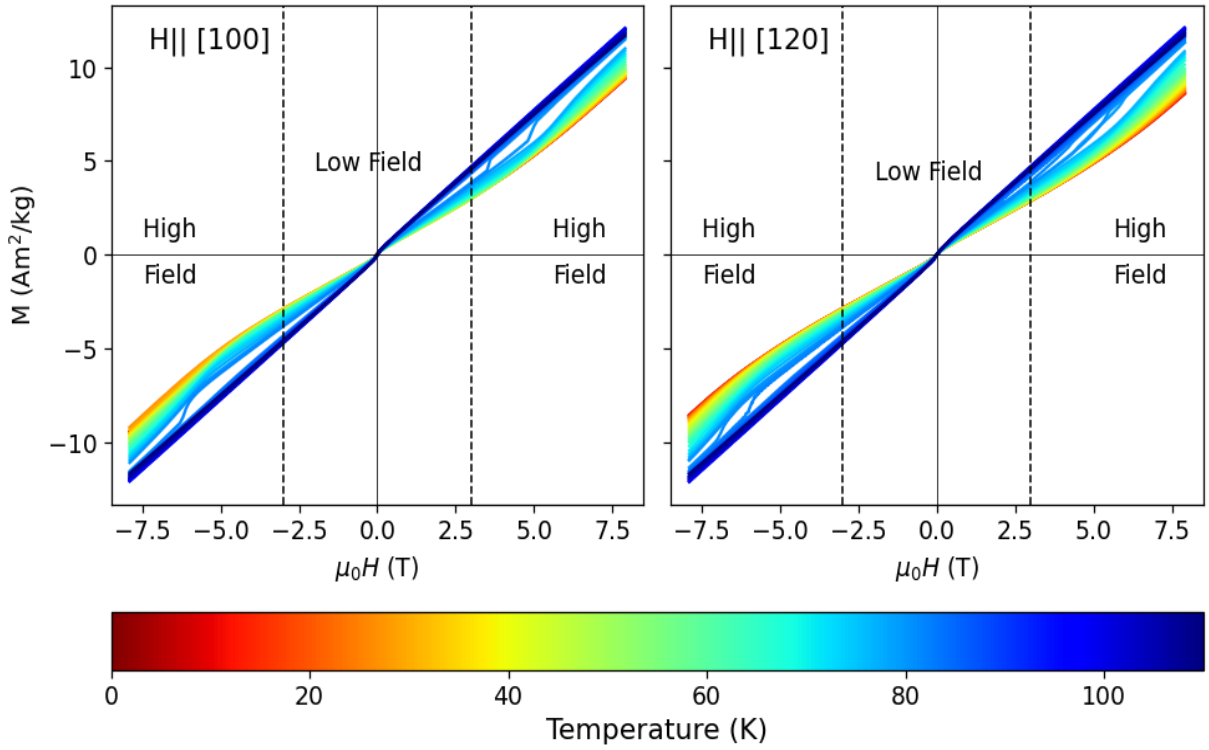

Figure A.1.1: Isothermal measurements of $Mn_4 Fe Si_3$ in the temperature range of (8-110) K, taken from the descending branch of the hysteresis loop, ($\mu_0 \Delta H$= 0. 1 T). (Left) H || [100] and (right) H || [120]. The data has been rebinned with ΔT= 1 K and $\mu_0 \Delta H$ = 0.1 T.

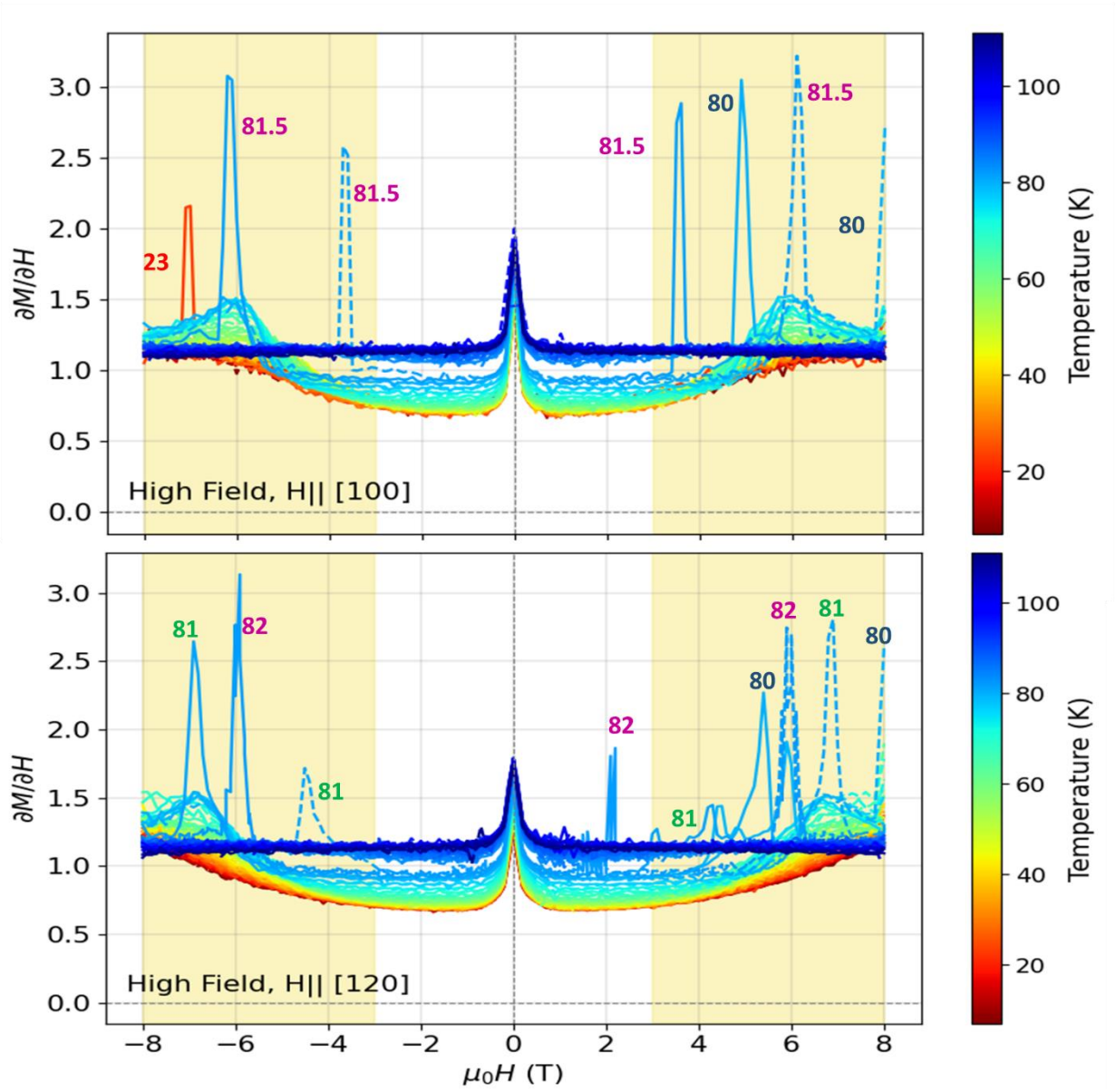

Figure A.1.2: $\frac{dM}{dH}$ **calculated from the hysteresis loops of** $Mn_4 Fe Si_3$ **at temperature range of (8-110) K. (Sürgers et al.) H || [100],** $\frac{dM}{dH} \times 10^2$ **and (bottom) H || [120],** $\frac{dM}{dH} \times 10^5$**. The solid lines are for the descending branch and the dashed ones for the ascending branch. Data was rebinned with ΔT= 1 K and** $\mu_0 \Delta H$ **= 0.1 T.**

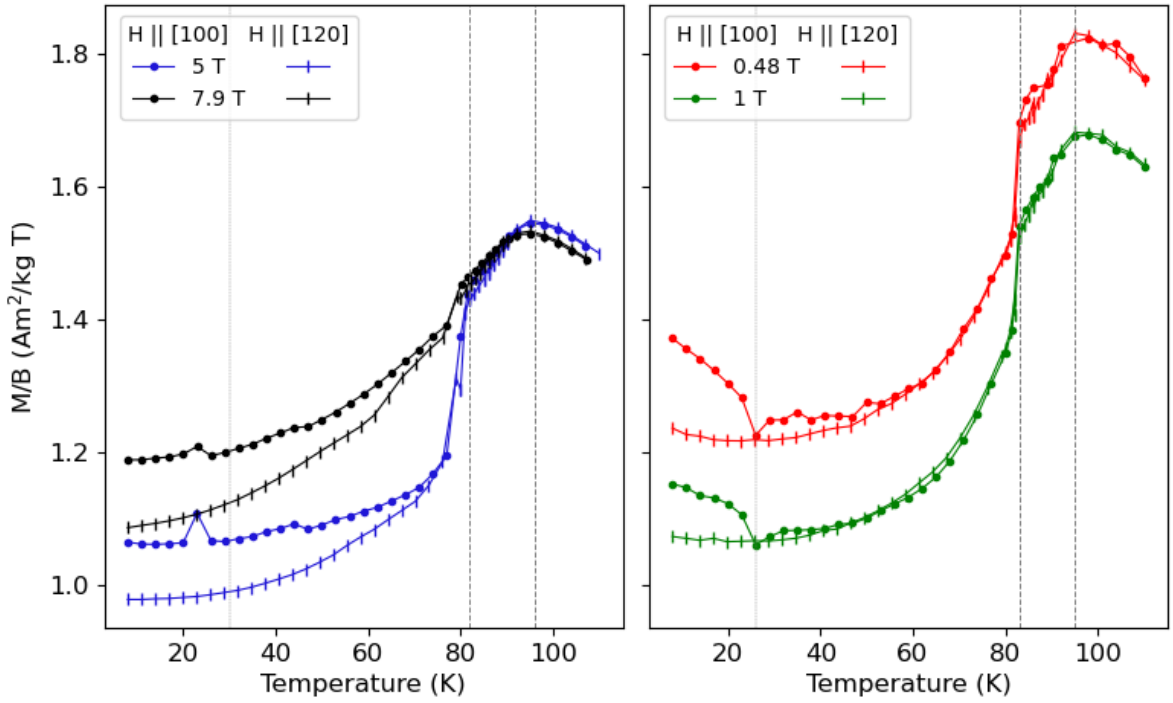

Figure A.1.3*:* M/B curves as a function of temperature, data obtained from the isothermal measurements in temperature range of (8- 110) K. (Left) with high fields (5, 7.9) and (right) with low fields (0.48, 1) T. Closed circles for data with H || [100]; vertical line for data obtained with H || [120]. Data was rebinned with *ΔT= 1 K* and $\mu_0 \Delta H$ = 0.01 *T*.

A.2 Comparison between the data obtained from the hysteresis branches

The data obtained by the isothermal measurements with H || ([001], [100] and [120]). The data pints from both branches of hysteresis loop coincide fairly.

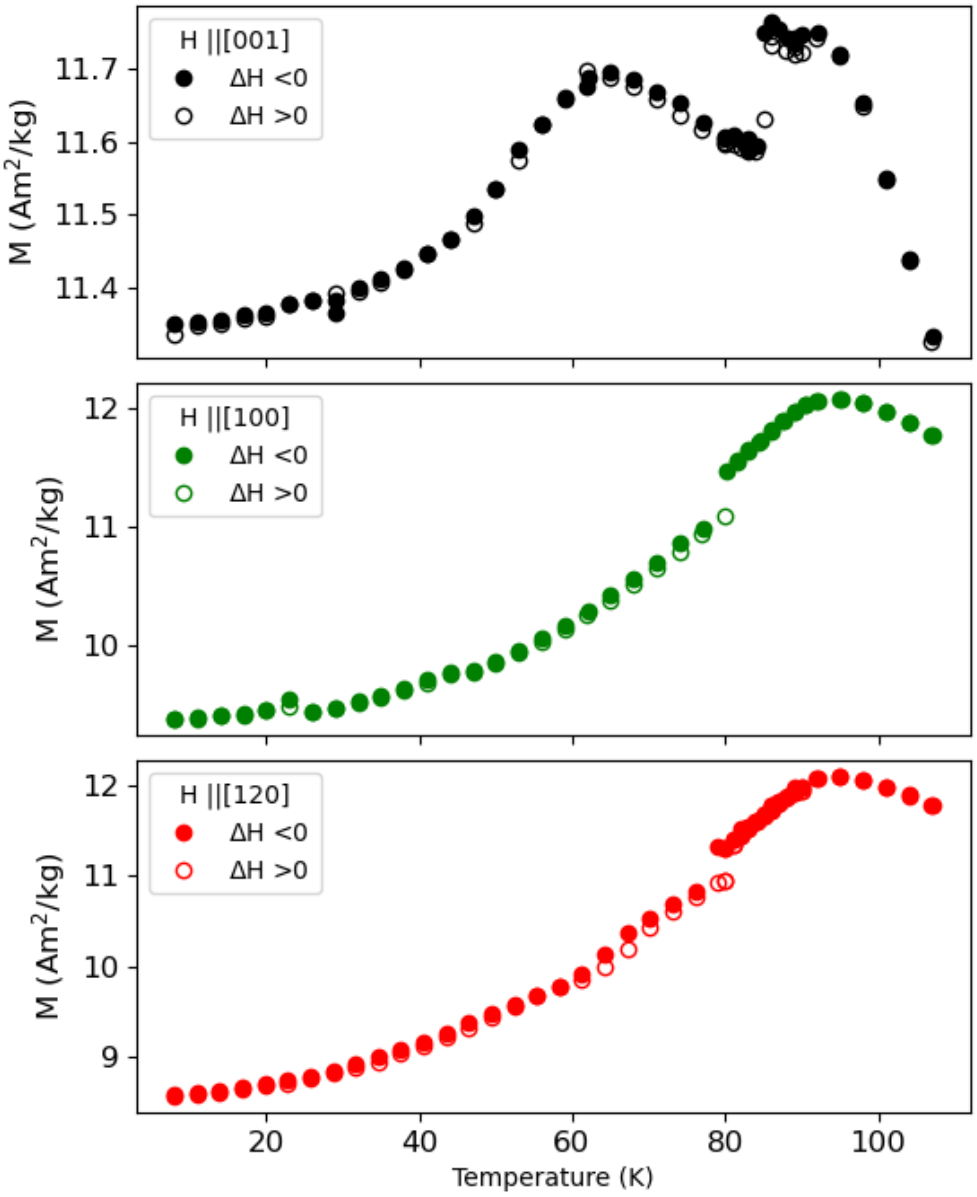

Figure A.2.1: M curves as a function of temperature, data obtained from the isothermal measurements in temperature range of (8- 110) K with field of 7.9 T. (Closed circles) data obtained from descending branch (opened circles) data obtained from ascending branch. (Blach) H || [001], (green) H || [100], and H || [120]. Data was rebinned with $\Delta T = 1\ K$ and $\mu_0 \Delta H = 0.01\ T$.

دراسة الخصائص المغناطيسية على بلورة أحادية من المركب $Mn_4\ FeSi_3$

إعداد:
شذى نزال ناجي نزال

إشراف:
د. حسين سمامرة و بروفيسور د. كارين فريزي و د. يورغ فويت و د. نور مرايطة.

ملخص:

في هذه الدراسة، تم الكشف عن خصائص مغناطيسية عيانية متنوعة للمركب$Mn_4\ FeSi_3$ ، عن طريق القياسات على بلورة أحادية. لقد تمت القياسات على بلورة منفردة محددة الاتجاهات مسبقاً، باستخدام خيار المقياس المغناطيسي لعينة مهتزة. في هذه الدراسة تم اتباع بروتوكولين مختلفين في القياس؛ الأول و هو القياس تحت مجال مغناطيسي ثابت و الثاني و هو القياس تحت درجة حرارة ثابتة. لقد أظهرت القياسات باستخدام العمليتين نتائجاً متقاربة إلى حد كبير، مما يشير إلى أن النظام، تحت الدراسة، هو دائماً في حالة اتزان ديناميكي حراري. تمت القياسات بتطبيق مجال مغناطيسي (حتى 8 تسلا) في ثلاثة اتجاهات مختلفة توازي اتجاهات التماثل للنظام البلوري السداسي ([001] ، [100] ، [120]). لقد تم تحديد العزم البارامغناطيسي تجريبياً بمقدار((4.3(1) μ_B. لقد اظهرت العينة استجابة مغناطيسية مختلفة عند توجيه المجال المغناطيسي باتجاهين مختلفين. بالاتفاق مع الدراسات السابقة فإن المركب يظهر تحولين. الأول من الحالة البارامغناطيسية إلى المغناطيسية المضادة (الانتيفرومغناطيسية) عند درجة حرارة 95 كلفن عند تطبيق المجال في الاتجاهات الثلاثة التي تمت دراستها. و الانتقال الثاني من حالة انتيفرومغناطيسية إلى أخرى قرب درجة حرارة 65 كلفن فقط عند تطبيق المجال في اتجاه [001]. تشير الدراسة الحالية إلى انتقال النظام من حالة استجابة مغناطيسية إلى أخرى بتأثير المجال المغناطيسية الخارجي في مدى درجات حرارة منخفضة تقل عن 80 كلفن و عند مجال مغناطيس بين 5 و 6 تسلا. تم معاينة هذا الانتقال بين طورين مغناطيسيين مع ملاحظة اختلاف الاستجابة عند تطبيق المجال باتجاهين مختلفين. ترجح النتائج سيادة التفاعلات الانتيفرومغناطيسية في المركب و تشير النتائج الى تفضيل العزوم المغناطيسية إلى الترتب بشكل متضاد في اتجاه عمودي على [001] ، مع وجود بعض التفاعلات الفرومغناطيسية لمركبات العزم المغناطيسية باتجاه[001] ، و التي يمكن التغلب عليها بزيادة شدة المجال المغناطيسي المطبّق. إلا أن هذه الملاحظات و النتائج تحتاج إلى مزيد من التحقق باستخدام وسائل قياس اكثر دقة مثل تشتت النيوترنات.